Molecular Dynamics Study of Liquid Crystals by ^{2}H and ^{14}N NMR Spectroscopy

BY

YANBIN CHEN

A Thesis submitted to

The Faculty of Graduate Studies

In Partial Fulfillment of the Requirements for the Degree of

MASTER OF SCIENCE

Department of Physics and Astronomy

University of Manitoba

Winnipeg, Manitoba

© Yanbin Chen, September 2005

To My Parents

Abstract

Deuterium (^{2}H) and Nitrogen 14 (^{14}N) NMR spectroscopy were used to investigate the molecular dynamics in one thermotropic and one lyotropic liquid crystal. Quantitative analyses of deuterium spectral densities of motion for three deuteron sites (ring and C_α) at two different Larmor frequencies (46 and 61.4MHz) are reported in the smectic A and C* phases of (*S*)-[4-(2-methylbutyl)phenyl]-4'-octylbiphenyl carboxylate (8BEF5-d_{15}), a partially deuterated smectogen. ^{2}H spectral densities for two deuteron sites on the chain (C_1 and C_2/C_3) at Larmor frequency 61.4MHz and ^{14}N spectral densities for the head group (NH_4^+) of the molecule decylammonium chloride (DACl) at 28.9MHz are reported in the lamellar phase of a partially deuterated sample, DACl-d_{11}/H_2O binary system.

The motional model is the small step rotational diffusion for reorientations plus internal rotations in the strong collision limit. In the chiral C* phase of the first molecule, 8BEF5-d_{15}, the helical axes are aligned along the external magnetic field and the deuteron spins appear to relax in a macroscopically uniaxial environment. After including the molecular tilt, the reorientation processes in the SmC* phase are found to have higher activation energies than those in the smectic A phase.

Applying the same motional models to the lyotropic molecule DACl-d_{11}, the tumbling motion of the long axis of the molecule in the aggregates is more rigorous in comparison to the molecular spinning motion. The similarity of deuterium spectral densities from the C_1 and C_2/C_3 sites may indicate a relatively rigid unit of C_1-C_2-C_3-C_4 in the backbone.

Acknowledgements

I would like to thank my supervisor, Dr. Ronald Y. Dong, for all his instruction, guidance and assistance throughout the entirety of this project. I also want to emphasize that his great patience, perseverance and countless hours spent for me and my project, especially during the difficult time in my experiments. The training opportunity with Dr. Dong benefits me in understanding what a research worker should be and how a research project should evolve. I am fortunate to study in the NMR lab of Dr. Dong.

Special thanks go to my committee members, Dr. Ronald Dong, Dr. David Hoult and Dr. Torsten Hegmann, for their guidance to literatures reading and intensive help to the revision of my master thesis.

My gratitude also goes to Mr. Jiadi Xu, who shares his knowledge with me in learning a variety of things ranging from NMR basic theory, spectrometer to graphic software. Jiadi is always there when I have some questions in mind. In addition, I really appreciate Jiadi and his wife, Cuimei Xu, for their care of me in life, like big brother and sister.

I would also like to thank Mr. Norm Finlay, Ms. Jing Zhang and all my other fellow students and friends in Winnipeg and Brandon, who have helped and entertained me throughout my master program in Canada.

At last, I am very grateful to my parents, Qixian Miao and Zhenji Chen, my brother, Yanjun Chen, and Uncle Zihao Song, for their endless support over the years.

Contents

List of Tables

List of Figures

1 Introduction

Nuclear Magnetic Resonance (NMR) was discovered by the groups of Purcell [1] and Bloch [2] in the 1940s. NMR is a phenomenon found in nuclear spin systems that involve magnetic moments and angular momenta [3]. The broad areas under study by NMR include solid-state physics, chemistry, chemical physics, biophysics and biochemistry, in which information on an atomic or molecular level can be obtained. Recently, Magnetic Resonance Imaging (MRI) has found exciting applications in medicine, e.g. in high quality but safe diagnosis by scanning the appropriate parts of the human body.

One of the most important fields of study in material sciences today is the study of liquid crystalline materials, which typically involve organic compounds and show a state of order intermediate between the crystalline solid and the isotropic liquid state. In 1888 Reinitzer [4] found, by using a polarizing microscope, a cloudy but completely fluid state in a substance (molten cholesteryl benzoate) which appeared between the solid phase at 145.5 ºC and a completely clear liquid phase at 178.5 ºC. This peculiar state was later called *"liquid crystal"* by Lehmann [5]. Today, *"mesophase"* is a more commonly used term than liquid crystals among scientists.

NMR has proven to be a powerful tool for studying mesophases [6]. In some cases, NMR is the only technique available to obtain information on the order of microscopic (atomic) scale in mesogenic materials. ^{2}H and ^{13}C NMR studies are conducted extensively in

dynamics and static structural research of liquid crystals. Other nuclei, such as ^{14}N and ^{1}H, have also been used.

1.1 Thesis Outline

Chapter 1 provides some fundamental NMR concepts both in a classical and a quantum mechanical picture. The structure of mesophases of liquid crystals and experimental methods closely related to the present research on a thermotropic and a lyotropic liquid crystal are outlined in Chapter 2. Chapter 3 outlines some particular motional models that are popular in the ^{2}H and ^{14}N NMR relaxation study of liquid crystals. The study based on a new approach in treating chiral smectogen in a biaxial phase as a uniaxial case is summarized in Chapter 4. The last chapter addresses another category of liquid crystals, lyotropics, and a dynamics study combining both ^{2}H and ^{14}N relaxation information is described.

1.2 Basic NMR in a Classical Picture

Nuclear Magnetic Resonance (NMR) is a phenomenon associated with the interactions between the magnetic moments of the spinning nuclei of matter and applied static and rotating magnetic fields. These nuclear magnetic moments, created by the electric charge and intrinsic angular momentum (or *spin*) of the nuclei, can precess about the direction of the static field at a well-defined *Larmor frequency* because of the torque resulting from the interaction with the static field. Another torque due to interaction with a second field,

which rotates about the static field at approximately the Larmor frequency, allows a change of declination of the bulk magnetic moment relative to the direction of the static field–the moment *nutates*. Thus, as the bulk magnetic moment precesses, having been nutated (or *flipped*) away from its equilibrium alignment with the static field, the NMR phenomenon is observed by detecting the e.m.f. (electromotive force) induced in a receiving coil placed perpendicular to the static field.

Not all nuclei possess spin, but plenty do, for example: ^{1}H, ^{2}H, ^{17}O, ^{13}C, ^{14}N, ^{31}P, etc. The availability of these nuclei in materials makes NMR a powerful and versatile tool in learning about the physical, chemical, and/or biological properties of matter [7].

Spin is a basic quantity like mass and electrical charge. While the rotation of the mass produces an angular momentum L, the rotation of the charge gives the nucleus a magnetic moment m [8], which experiences a magnetic torque in a static field. The Irish physicist Larmor showed in 1897 that the application of any aligning force (torque) to a spinning object causes a circular motion known as precession [9]. An everyday example is the slow wobble of a child's top (or a gyroscope) as it slows down. Here gravity produces a torque that causes the spinning object to rotate about a vertical axis. Similarly, a spinning magnet subjected to an external applied magnetic field can precess. The number of times per second that the axis of the magnet revolves about the static field direction is termed the resonant frequency, or the Larmor frequency. The linking of the Larmor frequency and the magnetic field strength is the most important relationship in magnetic resonance. The proportionality between the two is called the nuclear *gyromagnetic ratio* γ.

When a sample is placed in a strong static magnetic field, its magnetic moment grows parallel to the applied $\vec{B}_0$ field (the direction of the laboratory z axis) over the order, typically, of a fraction of a second, giving an *equilibrium* magnetisation M_o. (Magnetisation is magnetic moment per unit volume, and having direction and amplitude can be represented by a vector $\vec{M}$ [7].) This process of growth is termed *longitudinal relaxation*. Now instead of the laboratory frame (x, y, z) used above, it is often convenient to describe the precession in a *rotating frame* (x', y', z'), which rotates about the z axis at approximately the Larmor frequency of the spinning nucleus. When viewed from the frame rotating *exactly* at the Larmor frequency, the magnetisation does not precess, viz. it is stationary. The situation of no precession leads to the conclusion that in the rotating frame, there is *no* static $\vec{B}_0$ field! If now, in our rotating frame, an additional magnetic field $\vec{B}_1$ is applied perpendicular to the static field, the magnetic moment must precess about the direction of this new field due to the absence of the $\vec{B}_0$ field. The declination of the magnetic moment therefore progressively increases. By only keeping the $\vec{B}_1$ field on for the appropriate time (a *pulse*), the magnetisation can be "flipped" through any desired declinational angle, and in particular, flip angles of 90° (or $\pi/2$), 180° (or π) of $\vec{M}$ can be obtained. The jargon for such flips is "a 90 (180) degree pulse". Note that by applying successive pulses of $\vec{B}_1$ field at various orientations in the rotating $x'y'$ plane, not only the declination but also the azimuth of the magnetisation can be altered, for it always precesses about the $\vec{B}_1$ field.

In general, the reference frame does not have to rotate at the Larmor frequency – the

former's frequency may be larger or smaller than the latter's. Here any magnetisation that is not along the *z* axis appears to be slowly precessing about the *z* axis. This implies the existence of a small residual $\vec{B}_0$ field, $\Delta\vec{B}_0$, either in the +*z* direction, corresponding to when the frame rotates more slowly than the Larmor frequency, or in the –*z* direction, relating to when the frame rotates more quickly than the Larmor frequency. Then, when the $\vec{B}_1$ field, which is rotating with the rotating frame and is stationary therein, is applied, the magnetisation will precess about the vector sum $\vec{B}_{eff}$ of the fields $\Delta\vec{B}_0$ and $\vec{B}_1$, as shown in Fig. 1.1.

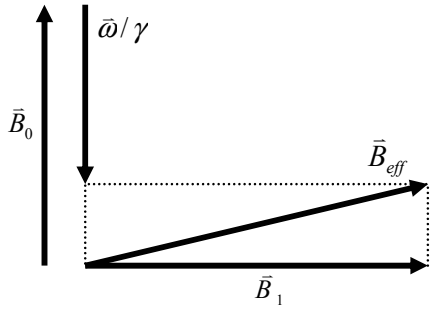

Fig. 1.1 The effective magnetic field $\vec{B}_{eff}$ in the rotating frame, is the vector sum of the external field $\vec{B}_0$, the fictitious field $\vec{\omega}/\gamma$ and *r.f.* field $\vec{B}_1$.

Note that if the applied $\vec{B}_1$ field rotates at a frequency far off the Larmor frequency, namely, $\Delta\vec{B}_0 >> \vec{B}_1$, there will be negligible flipping of magnetisation and therefore negligible transverse magnetisation. Proper signal detection requires a big transverse magnetisation so that a large voltage is induced in a receiving coil, and this only is possible when the rotational frequency of the $\vec{B}_1$ field is close to the Larmor frequency. Clearly, the phenomenon satisfies a definition of "resonance" [10]: *When an abnormally large vibration of an object is produced in response to an external stimulus at a frequency which is the same, or nearly the same, as the natural vibration frequency of the object.*

To further this discussion, we now turn to a more formal mathematical description of the subject. Mathematically, the relation of the fixed lab frame and the rotating frame could be derived by considering time derivatives of $\vec{M}$ [11],

$$\left(\frac{d\vec{M}}{dt}\right)_{fixed} = \left(\frac{d\vec{M}}{dt}\right)_{rot} + \vec{\omega}\times\vec{M}\,, \tag{1.1}$$

where the magnitude of $\vec{\omega}$ gives the angular frequency of rotation of the unit frame $(\hat{i},\hat{j},\hat{k})$, while the direction of $\vec{\omega}$ is the axis about which the rotation occurs. In such a rotating coordinate system all three unit vectors rotate with a velocity and direction defined by the same $\vec{\omega}$. Since in the laboratory frame,

$$\left(d\vec{M}/dt\right)_{fixed} = \gamma\vec{M}\times\vec{B}, \tag{1.2}$$

where $\vec{B}$ is a general magnetic field, one finds in the rotating frame,

$$\left(d\vec{M}/dt\right)_{rot} = \gamma\vec{M}\times\vec{B} - \vec{\omega}\times\vec{M} = \gamma\vec{M}\times(\vec{B}+\vec{\omega}/\gamma). \tag{1.3}$$

The fictitious term $\vec{\omega}/\gamma$ is introduced by the rotation. If $\vec{B}$ is a constant field $\vec{B}_0$ in the *z* direction, then when $\vec{\omega} = -\gamma\vec{B}_0$ the magnetisation is a fixed vector and precesses with an angular velocity $\omega_0 = -\gamma B_0$, the Larmor frequency. However, if the total field $\vec{B}$ is the sum of the constant field $\vec{B}_0$ and another field $\vec{B}_1$, perpendicular to $\vec{B}_0$ and rotating it around it with an angular velocity $\vec{\omega}$, then there is an effective field

$$\vec{B}_{eff} = \left(B_0 + \omega/\gamma\right)\hat{k} + B_1\hat{i}\,, \tag{1.4}$$

where the $\vec{B}_1$ field has been placed along the *x* axis of the rotating frame. One then finds from Eq. (1.3) that

$$\left(d\vec{M}/dt\right)_{rot} = \gamma\vec{M}\times\vec{B}_{eff}\,. \tag{1.5}$$

and $\vec{M}$ precesses about the $\vec{B}_{eff}$ field in the rotating frame, Upon resonance, the fictitious term $\vec{\omega}/\gamma$ in Eq. (1.4) is in the opposite direction to $\vec{B}_0$ and cancels $\vec{B}_0$, leaving, in the rotating frame, only $\vec{B}_1$ interacting with $\vec{M}$. However, in an off-resonance situation, the $\vec{B}_1$ field and the rotating frame are not at the resonant Larmor frequency ω_0, and the term $\vec{\omega}/\gamma$ cannot cancel $\vec{B}_0$ completely, leaving a component of the effective field in the *z* direction. Then,

$$\begin{aligned} \left|\vec{B}_{eff}\right| &= \left[\left(B_0 - \omega/\gamma\right)^2 + B_1^2\right]^{1/2} \\ &= (1/\gamma)\left[\left(\omega_0 - \omega\right)^2 + \omega_1^2\right]^{1/2} \equiv \Omega/\gamma, \end{aligned} \tag{1.6}$$

where $\omega_1 = \gamma B_1$ is the on-resonance nutational frequency and Ω is the off-resonance nutational frequency.

Apart from a deliberate choice, this off-resonance condition ($\omega \neq \omega_0$) could be due to a) field inhomogeneity, i.e., nuclei at different positions experience different magnetic fields resulting in different Larmor frequencies, or b) *chemical shifts* that are caused by the small magnetic field of surrounding electron clouds, or c) additional local magnetic fields introduced by neighbouring nuclei. The magnetic field at the nucleus is *not* equal to the applied magnetic field, since electrons around the nucleus shield it from the applied field. The difference between the applied magnetic field and the field at the nucleus is termed the *nuclear shielding* or chemical shift. Chemical shift anisotropy is described by the chemical shift tensor $\hat{\sigma}$, and is particularly important in obtaining molecular structure information [12].

So far, we have considered ways of understanding excitation and mentioned the factors

that determine the Larmor frequency. However, after excitation, the nuclear system returns to equilibrium and we now briefly examine how. In a microscopic picture, the molecules, which bear nuclear spins, are randomly moving and tumbling in a manner that is traditionally described as "Brownian motion". This is due to the kinetic energy of the molecules along with constant collisions between them. The accompanying random motions of the nuclear magnetic moments in space, as the nuclei "tag along for the ride", generate fluctuating magnetic fields which provide an interaction mechanism between nuclei. The magnetisation $\vec{M}$ then relaxes due to these interactions. Transverse components of the fluctuating fields rotating at the Larmor frequency change the declinations of the magnetic moments, providing a mechanism, *on average*, for release of magnetic energy $-\vec{M}\cdot\vec{B}_0$ and eventual partial alignment with $\vec{B}_0$. Attainment of alignment and therefore release of energy, which minutely heats the sample and increases the molecular translational and rotational energy, is typically an exponential process, with a characteristic time constant T_1 determined by the molecular dynamics. This dynamic mechanism (sometimes called a *spin-lattice relaxation* mechanism, a term borrowed rather loosely from sold-state physics) effectively determines the recovery behaviour of the longitudinal magnetisation M_z, the z-component of the magnetisation vector, to its equilibrium value M_o. If the equilibrium magnetisation is flipped by a 90º pulse into the xy plane, M_z can be plotted as a recovery function as follows,

$$M_z = M_0\left(1-e^{-t/T_1}\right). \tag{1.7}$$

This experimentally-observed exponential relaxation can be incorporated into the

equation of precessional motion given above (Eq. 1.2) as the following phenomenological equation formulated by Bloch [2],

$$\frac{dM_z}{dt} = \gamma\left(\vec{M} \times \vec{B}\right)_z - \frac{M_z - M_0}{T_1}. \tag{1.8}$$

There is a second relaxation process in NMR, associated with low-frequency, axial (parallel to $\vec{B}_0$) components of the fluctuating magnetic fields, that occurs simultaneously with longitudinal relaxation. Fluctuating differences in $\vec{B}_0$ from place to place in the sample give rise to a range of Larmor frequencies, constantly fluctuating, and hence a progressive random and *irreversible* dephasing of the sum transverse magnetisation. As energy is exchanged only between nuclei in this process, it is sometimes termed *spin-spin* relaxation, or more commonly *transverse relaxation* for it causes the *xy* component of $\vec{M}$, M_{xy} , to decrease to zero. T_2 is the time constant describing the decay of the transverse magnetisation to zero according to

$$\frac{dM_{xy}}{dt} = \gamma\left(\vec{M} \times \vec{B}\right)_{xy} - \frac{M_{xy}}{T_2} \tag{1.9}$$

$$\Rightarrow M_{xy} = M_{xy0} e^{-t/T_2}. \tag{1.10}$$

Eqs. (1.8) and (1.9) are the *Bloch equations*. T_1 relaxation processes arise only from fluctuating magnetic field with components in the *x*' and *y*' directions, while T_2 processes arise from components in all three directions [11]. Although the T_1 and T_2 processes happen simultaneously, in the solid state the T_2 process is usually much faster than the T_1 process. However, T_1 is equal to T_2 in isotropic liquids, due to the rapidity of the motional processes which causes the effects of the transverse fluctuating fields to be dominant. In

general, any mechanism which gives rise to fluctuating magnetic fields at a nucleus is a possible relaxation mechanism. Various physical interactions have been found to be important in spin-lattice relaxation and these interactions are discussed in Section 1.5.

In practice, inhomogeneity in the main magnetic field $\vec{B}_0$ significantly affects the T_2 process. It causes the Larmor frequency to differ from place to place in the sample adding a term T_2^{inho} into the actual time constant that we measure, called T_2^*, represented by

$$1/T_2^* = 1/T_2^{real} + 1/T_2^{inho}. \qquad (1.11)$$

Note that the dephasing caused by static field inhomogeneity is macroscopic and in principle *reversible*, while the spin-spin relaxation, characterized by T_2^{real}, is microscopic and irreversible. To illustrate how macroscopic dephasing can be reversed, we consider a simple pulse sequence, the Hahn echo experiment [13], a practical way of measuring T_2 (Fig. 1.2). Due to the field inhomogeneity, transverse magnetisations $\vec{m}_i$ arising from nuclei in different parts of the sample experience slightly different values of applied field, and thus, following a 90º pulse (Fig 1.2.i and following), they precess with a range of frequencies about the Larmor frequency. The $\vec{m}_i$ thus start to "fan out" in the $x'y'$ plane (ii). However, a subsequent 180º pulse (iii) at time τ inverts the y' components of magnetisation, and an element that had precessed an angle ϕ from the x axis now is at angle $-\phi$. The field inhomogeneity affecting the nuclei prior to the 180º pulse will continue to influence the same nuclei in precession in the same manner after the inversion pulse (iv), and so the spins refocus along the $-y$ axis at time 2τ with an amplitude diminished only by true transverse relaxation (T_2).

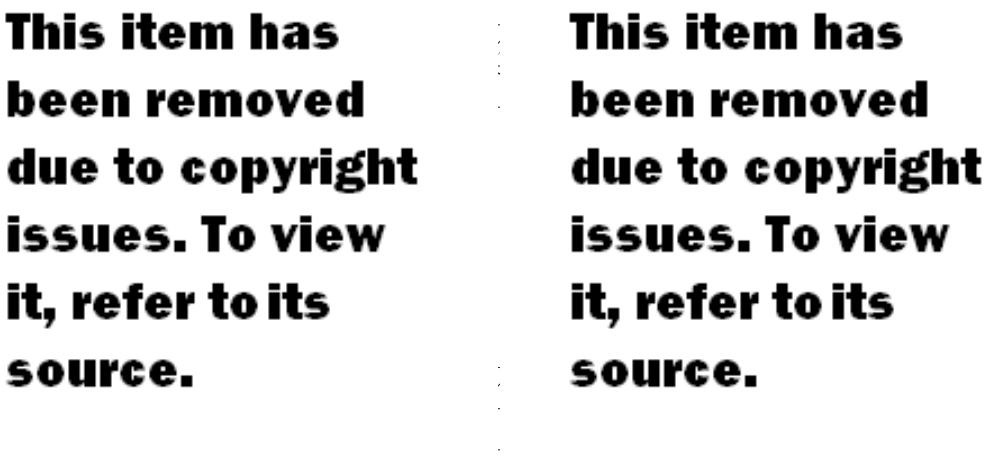

Fig. 1.2 Illustration of spin dynamics of Hahn echo experiment [14].

Turning very briefly now to experimental details, in performing an NMR experiment, an *alternating* RF magnetic field [15] is created when an alternating RF current at the Larmor frequency is passed through a transmitter coil surrounding the sample. In the laboratory frame, this magnetic field can be considered to be an oscillating vector along the *x* axis having amplitude $2B_1$. However an oscillating vector can be decomposed into two components, each of amplitude B_1, one rotating clockwise at a frequency of $+\omega_0$, and the other rotating counterclockwise at $-\omega_0$. In a frame rotating clockwise about the *z* axis at frequency $+\omega_0$, the $\vec{B}_1$ vector component that rotates clockwise in the laboratory frame will be stationary, while the $\vec{B}_1$ counterclockwise rotating component will be at frequency $-2\omega_0$ in the positively rotating frame. A field that rotates about the *z* axis at $-2\omega_0$ is so far from the resonance frequency of the spins that it can be ignored [7]. To transmit then, a *high power RF amplifier* [10] is used to put RF current into the coil for the length of time needed to create the desired pulse.

Besides the coils of wire in a persistent superconducting magnet which generate the strong external $\vec{B}_0$ field along the *z* direction, a *receiving coil* must be present to perform signal detection. The signal is received by the precessing transverse magnetisation's inducing a voltage in the receiving coil — the FID. That coil must therefore be designed so that, if current *were* passed through it, *would* produce a $\vec{B}_1$ field in the *xy* plane. The maximum signal to noise ratio can be obtained by an appropriate coil design. The underlying assumption here is that the noise originates solely from the Brownian motion of the electrons in the receiving coil and is a manifestation of coil resistance and temperature [10]. The FID signal is now passed to a low-noise pre-amplifier and thence to the spectrometer receiver for analysis. In practice, a *quadrature detector* [16] is used to subtract the transmitter frequency from that of the FID while retaining the value(s) and the sign(s) of the difference frequency(ies). This makes analogue-to-digital conversion easier while preserving chemical shift information.

Plotting received voltage as a function of time gives a sine wave, which will decay with a time constant T_2^*. To get frequency information, a frequency domain spectrum is then obtained by *Fourier Transformation* (FT) [7] of the FID. In the early days of NMR, a simple method called a *continuous wave* (CW) experiment was performed at constant radio frequency by sweeping the B_0 field strength to observe a signal when resonance was attained. Nowadays, pulsed methods and fast FT by means of a computer make NMR versatile for various complicated experiments. In FT-NMR, *all* frequencies in an NMR spectrum are stimulated simultaneously with a short radio-frequency pulse. Compared to

a CW experiment, FT-NMR has the advantage of saving a great amount of time [17].

1.3 Quantum Mechanical Aspects of NMR

Since spin is described with a quantum number, it can only be multiples of ±1/2. Unpaired protons, electrons, neutrons are spin 1/2. Two or more particles with opposite signs can eliminate their spins. For a deuterium atom ^{2}H, a neutron and a proton have a total nuclear spin $I = 1$.

Let us consider a simple case: a proton with spin 1/2 is put in an external magnetic field. The energy of magnetic interaction $\vec{m} \cdot \vec{B}_0$ is *quantized* and there are thus two energy states — 'spin up' and 'spin down'. The spin could transit to a high energy state 'spin down' only if it absorbs an exact amount of energy that is equal to the energy difference between spin up level and spin down level. After absorption, the spin cannot stay at that excited energy state for long, but drops back to the low energy level and in the meanwhile, releases that amount of energy to the surroundings — the 'lattice'. The lifetime of this energy emission process is the spin-lattice relaxation time T_1, during which the excited spin-down spins fully release all the excess energies, and the spin exchange between both energy levels reaches a dynamic equilibrium. In general, for a nucleus of spin I, its energy can be represented by

$$E = -m\gamma\hbar B_0, m = I, I-1....-I, \tag{1.12}$$

where $\hbar$ is the Planck's constant over 2π, m the quantum number, I the spin ($I = 1$ for deuteron), and γ the gyromagnetic constant, which is specific to each kind of nuclei. Both

the γ and the external magnetic field B_o determine the exact amount of energy gap for a resonance. However, only certain transitions are allowed, governed by the *selection rule* $\Delta m = \pm 1$. Thus the allowable change in energy is

$$\Delta E = \gamma \hbar B_0 \tag{1.13}$$

or

$$\Delta E = \hbar \omega_0 \tag{1.14}$$

Thus, if an applied B_1 field has a frequency ω_0, a quantum of energy may be absorbed from the field or released to the field. In particular, such fields provide a relaxation mechanism for extracted energy from an excited system. Relaxation phenomena are of paramount importance in NMR. It is because of the existence of relaxation mechanisms that the nuclear spin can 'feel' the temperature of the lattice, and that differences of populations can appear between the various energy levels of the nuclear spin system, leading to a net absorption by the spin system of *r.f.* power supplied by an external generator. As a consequence of these differences, a net nuclear magnetisation [15]

$$\vec{M} = \frac{N\gamma^2\hbar^2 I(I+1)\vec{B}_0}{3kT} \tag{1.15}$$

appears in an applied field $\vec{B}_0$. Here N expresses the number of nuclear spins per unit volume, k denotes Boltzmann's constant and T is absolute temperature. At equilibrium and room temperature, the number of spin in the lower energy state is slightly greater than the number in the upper energy level. This spin distribution obeys Boltzmann statistics. For a coupled spin 1/2 pair, each spin can be in the α (spin up) or β (spin

down) state, and so there are four possibilities: $\alpha_1\alpha_2$, $\alpha_1\beta_2$ or $\beta_1\alpha_2$ and $\beta_1\beta_2$. These four possibilities correspond to four energy levels. Note that subscript 1 or 2 is added to differentiate the two nuclei. The close correspondence of the classical and quantum mechanical treatments is made particularly clear by examining a differential equation relating the time variations of the expectation values $\langle \mu_x \rangle, \langle \mu_y \rangle$, and $\langle \mu_z \rangle$. It is found that the equation of the expectation value of magnetisation [3]

$$\frac{d\langle \vec{\mu} \rangle}{dt} = \langle \vec{\mu} \rangle \times \gamma \vec{B} \tag{1.16}$$

is just the classical equation and the expectation value of the magnetic moment obeys the classical equation of motion. Eq. (1.16) was derived for a single spin. If the spins are assumed not to interact with one another in a system, Eq. (1.16) can be easily proved to be true for the expectation of the total magnetisation. In practice, this is true because we measure the results of a number of spins simultaneously; the observed bulk magnetisation is simply the expectation value of the total magnetic moment [3].

Although radiative transitions between energy levels are commonly used as a simple picture in the literature to explain the NMR signal, this is not actually the case: if a significant number of radiative transitions were to occur during signal reception, these would dissipate the stored energy as emitted radio waves; however, the energy associated with signal reception is mostly lost in the form of heat in the resistance of the receiving coil and pre-amplifier through which the induced current passes. This near-field loss mechanism can be so large as to change the effective longitudinal relaxation time T_1.

Thus, NMR is actually *not* about absorption and emission of radio waves [18], as almost universally portrayed in the scientific literature and community. For more details, please refer to the explanation of an exchange of *virtual phonons* [18] in the theory of quantum electrodynamics by Hoult and Ginsberg.

1.4 Density Matrix

In a complex multi-spin system, the *density matrix*, σ , is a good tool in treating a huge number of atoms with certain interactions given by a spin Hamiltonian via statistical means. This is because no solution of the probability amplitudes, or a complete set of wave functions is necessary. The spin system is in a state of wave function or ket $|\varphi_k\rangle$, which is in general time-dependent and may be expanded using a complete orthonormal basis set of *m* stationary kets $|\phi_i\rangle \equiv |i\rangle$. So,

$$|\varphi_k\rangle = \sum_{i=1}^{m} C_i^k(t)\,|i\rangle, \tag{1.17}$$

where C_i is the amplitude. The density matrix element, σ_{ji}, is defined as the ensemble average of product of amplitudes from two orthonormal basis sets

$$\sigma_{ji} = \sum_k C_j^k C_i^{k*} / N = \overline{C_j C_i^*}, \tag{1.18}$$

where *i* and *j* represent the index of the orthonormal basis.

The evolution of density matrix is given by the following equation,

$$\frac{d\sigma}{dt} = -i[(H_0 + H'(t)), \sigma], \tag{1.19}$$

where H_0 is the static Hamiltonian and H' represents the time-dependent spin-lattice

coupling. One can show that the irreducible spectral densities $J_m(\omega_{m,q})$ are the Fourier transforms of the correlation functions $G_m(\tau)$,

$$J_m(\omega_{m,q}) = (C_\lambda \rho_{2,0})^2 \int_0^\infty G_m(\tau) e^{-i\omega_{m,q}\tau} d\tau , \tag{1.20}$$

where $\omega_{m,q}$ are the characteristic frequencies arising through transforming to the interaction picture and can be expressed in terms of a linear combination of the resonant frequencies of the relaxing spin(s) [6]. The relaxation rates ($1/T_1$ and $1/T_2$) can be written as a linear combination of irreducible spectral densities and the coefficients of expansion are obtained by evaluating the double commutators of spin operators for a specific spin-lattice interaction λ. In working out $G_m(\tau)$, one can use successive transformations from the *principal axis system* (PAS) to the laboratory frame and the closure property of the rotation group to rewrite $D^2_{m0}(\Omega_{PL})$ so as to include the effects of local segmental, molecular, and/or collective motions for molecules in liquid crystals.

1.5 Spin Interaction

A NMR spectrum of a liquid crystal contains, in principle, both static and dynamic information. The position and the relative intensity of the peaks can give the partially averaged spin interactions [19], while the linewidths of these peaks may provide dynamic information. The Hamiltonian [6] of the spin system is used to describe the quantum interaction in NMR. Here five kinds of interactions are of interest: Zeeman interaction, nuclear dipole-dipole interaction, J-coupling, quadrupolar interaction and chemical shift, which are indexed as Z, D, J, Q, CS, respectively for future notation.

Spin Hamiltonian

The Zeeman Hamiltonian H_z between the magnetic moment of a nucleus and external magnetic field is written as

$$H_Z = -\gamma\hbar\vec{I}\cdot\vec{B}_0 . \tag{1.21}$$

If including the chemical shift anisotropy, also called diamagnetic shielding, which describes the weakening effect of the external field due to neighbouring electron clouds, the Zeeman interaction should be rewritten as

$$H_Z = -\gamma\hbar\vec{I}\cdot(\hat{1}-\hat{\sigma})\cdot\vec{B}_0 , \tag{1.22}$$

where $\hat{\sigma}$ is a 2nd rank tensor that describes the chemical shift anisotropy.

The dipole-dipole (dipolar) Hamiltonian H_D shows the magnetic interaction between two magnetic moments,

$$H_D = \frac{\gamma_i\gamma_j\hbar^2}{r_{ij}^3}\vec{I}_i\cdot\hat{D}_{ij}\cdot\vec{I}_j , \tag{1.23}$$

where r_{ij} is the internuclear distance between the two nuclei, and $\hat{D}_{ij}$ is a dipolar coupling tensor of 2nd rank, which is similar to a chemical shift tensor. Its main difference from the chemical shift interaction, however, is that the dipolar tensor is traceless; that is, the sum of its diagonal elements is zero. Therefore, unlike the chemical shift, dipolar interactions are averaged to zero in solution due to the isotropic tumbling of molecules.

In addition, the indirect, electron-mediated interaction called J-coupling is different from dipolar interaction because J-coupling works through the electrons in bonds while the dipolar interaction works directly between nuclei. Now

$$H_J = \hbar \vec{I}_i \cdot \hat{J}_{ij} \cdot \vec{I}_j , \tag{1.24}$$

where the J-coupling tensor $\hat{J}_{ij}$ is not traceless. In liquid crystal, H_J is usually small compared to H_D and will be ignored. The quadrupolar Hamiltonian is the main interaction in our ^{2}H and ^{14}N NMR study, its presentation is deferred to section 1.6.

Motionally Averaged Hamiltonian

Although having similarities to both solid and liquid phases, the molecules in liquid crystals are rotating and diffusing at rates similar to those in isotropic liquids, but are not random. The fast motion in the mesophase of a liquid crystal is such that usually the nuclear spin interactions are averaged, but the non-randomness means that the averages are different from those in its isotropic phase. In liquid crystals, three main types of interactions of interest are time-averaged dipolar, quadrupolar and chemical shift Hamiltonians. The time averaging nuclear spin Hamiltonians may be easily studied in the form of irreducible spherical tensor operators of rank l, $T_{l,m}$ and $R_{l,m}$.

$$H_\lambda = C_\lambda \sum_l \sum_{m=-l}^{l} (-1)^m T_{l,m}^\lambda R_{l,-m}^\lambda , \tag{1.25}$$

where l = 0,1,2 and scalar factor C_λ is the appropriate interaction constant with a label λ for the type of interaction. Thus,

$$C_D = -\mu_0 \gamma_I \gamma_S \hbar^2 / 2\pi , \;\; C_Q = eQ / 2I(2I-1) , C_{CS} = \gamma_I \hbar . \tag{1.26}$$

For λ=*D or Q,* the spin operators $T_{l,m}$ in the laboratory frame are

$$T_{0,0} = -\sqrt{\frac{1}{3}} \vec{I} \cdot \vec{S} , \;\; T_{2,0} = \sqrt{\frac{1}{6}} \left(3 I_Z S_Z - \vec{I} \cdot \vec{S} \right),$$

$$T_{2,\pm1} = \mp\frac{1}{2}\left(I_Z S_\pm + I_\pm S_Z\right),\ \ T_{2,\pm2} = \frac{1}{2} I_\pm S_\pm . \tag{1.27}$$

Here, the two spins $\vec{I}$, $\vec{S}$ can be either the same for homonuclear dipolar coupling or quadrupole coupling, or unequal for heteronuclear dipolar interaction.

The coupling tensor $R_{l,m}$ in the laboratory frame is time-dependent due to motions of spin-bearing molecules. It is more convenient to transform $R_{l,m}$ to the principal axis system (PAS), in which the irreducible components are $\rho_{l,n}$, and

$$R_{l,m} = \sum D^{l*}_{mn}(\Omega_{PL})\rho_{l,n}, \tag{1.28}$$

where $D^{l}_{m,n}(\Omega_{PL})$ denotes the Wigner rotation matrices and Ω_{PL} are the Euler angles by which the laboratory frame is brought into coincidence with the PAS. Meanwhile,

$$\rho_{2,0} = \sqrt{\frac{3}{2}}\Delta_\lambda,\ \ \rho_{2,\pm1} = 0,\ \ \rho_{2,\pm2} = \frac{1}{2}\Delta_\lambda\eta_\lambda, \tag{1.29}$$

where in the dipolar case λ=D, $\eta_D = 0$ and $\Delta_D = \left\langle 1/r^3_{IS} \right\rangle$ and r_{IS} is the internuclear distance. In the quadrupolar case (see below), λ=Q, Δ_Q and η_Q can be obtained from V_{ii}, the principal values of the electric field gradient tensor $\hat{V}$, which is diagonalized in the PAS. The electric field gradient, abbreviated as *efg*, $\Delta_Q = V_{zz} = eq$, and the *asymmetry parameter* [6] of the *efg* tensor is defined as

$$\eta_Q = \frac{V_{xx} - V_{yy}}{V_{zz}}. \tag{1.30}$$

1.6 Nuclear Electric Quadrupolar Interaction

The quadrupolar interaction arises from the interaction, at the site of the nucleus, between the nuclear electric quadrupole moment eQ and the non-spherically symmetric electric

field gradient, *efg*, caused by the electric charge distribution of the atom or molecule. The quadrupolar Hamiltonian only occurs when $I > 1/2$, and is expressed as,

$$H_Q = \hbar \vec{I} \cdot \hat{Q} \cdot \vec{I} = \frac{eQ}{2I(2I-1)} \vec{I} \cdot \hat{V} \cdot \vec{I} \,, \tag{1.31}$$

where the quadrupolar coupling tensor $\hat{Q}$ has been written in terms of *efg* tensor $\hat{V}$. Now, in the general irreducible tensor representation, $R^Q_{l,m}$, are nonzero only when $m = 0, \pm 2$, and the components $m = \pm 1$ vanish. Since $\hat{V}$ is symmetric and traceless in PAS, the quadrupolar Hamiltonian can be written in PAS as:

$$H_Q = \hbar \omega_Q \left\{ \left[I_z^2 - \frac{1}{3} I(I+1) \right] + \frac{\eta}{3} \left(I_x^2 - I_y^2 \right) \right\}, \tag{1.32}$$

where the quadrupolar frequency ω_Q is defined as

$$\omega_Q = \frac{3e^2 qQ}{4I(2I-1)\hbar} \,, eq = V_{zz} \,. \tag{1.33}$$

In the deuteron case, the asymmetry parameter η can usually be approximated as $\eta = 0$ (η~0.04 for aromatic deuterons) due to "axial" symmetry of the electric field gradient along the C-^{2}H bond. Thus, $V_{xx} = V_{yy}$, and the principal *z* axis is along the C-^{2}H bond.

The time-averaged quadrupolar Hamiltonian, for a deuteron spin with axially symmetric *efg* ($\eta = 0$), becomes

$$\overline{H_Q} = \overline{\omega_Q} [I_z^2 - I(I+1)/3] \,, \tag{1.34}$$

where

$$\overline{\omega_Q} = \frac{3}{4} \frac{e^2 qQ}{\hbar} \sum_m \overline{D^2_{0,m}(\theta, \varphi)} D^2_{m,0}(\beta, \alpha) \,, \tag{1.35}$$

with (β, α) being the polar angles of the C-^{2}H vector in the molecular frame, and the

time-averaged Wigner rotation matrices $\overline{D^2_{0,m}(\theta,\varphi)}$ being the order parameters in a uniaxial phase. These order parameters can be written in terms of a Cartesian order tensor $\hat{S}$ [20,21] which is symmetric and traceless 3×3 matrix. The $\hat{S}$ has a maximum of five independent, nonzero elements, and their relations with the time-averaged Wigner rotation matrices are

$$S_{zz} = \overline{D^2_{0,0}}\,,\quad S_{xx} - S_{yy} = \sqrt{\frac{3}{2}}\left(\overline{D^2_{0,2}} + \overline{D^2_{0,-2}}\right),\quad S_{xy} = i\sqrt{\frac{3}{8}}\left(\overline{D^2_{0,-2}} - \overline{D^2_{0,2}}\right)$$

$$S_{xz} = \sqrt{\frac{3}{8}}\left(\overline{D^2_{0,-1}} - \overline{D^2_{0,1}}\right),\quad S_{yz} = i\sqrt{\frac{3}{8}}\left(\overline{D^2_{0,-1}} - \overline{D^2_{0,1}}\right) \tag{1.36}$$

Hence, the quadrupolar splitting (Fig. 1.3) of a Zeeman line is

$$\Delta\nu_Q = \frac{3}{2}\frac{e^2qQ}{h}\left[S_{zz}\left(\frac{3}{2}\cos^2\beta - \frac{1}{2}\right) + \frac{1}{2}\left(S_{xx} - S_{yy}\right)\sin^2\beta\cos 2\alpha\right] \tag{1.37}$$

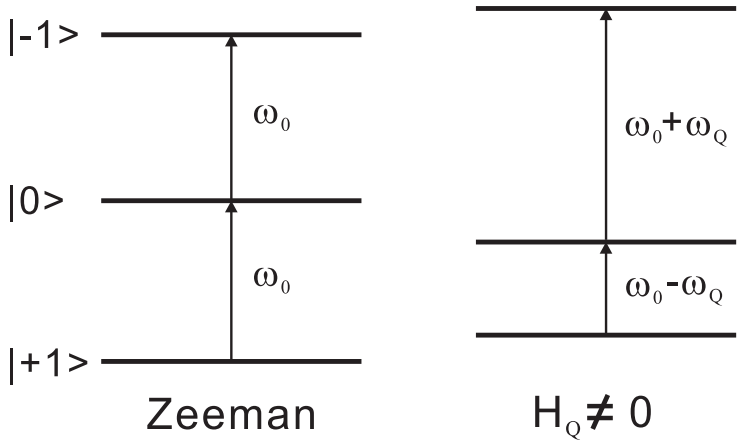

Fig. 1.3 Energy level diagram for a deuteron spin in a magnetic field. $\omega_0/2\pi$ is the Larmor frequency.

If η is nonzero as in the aromatic deuteron site, Eq. (1.37) must be modified to give [19,22]

$$\Delta\nu_q^i[T] = \frac{3}{2}\left(\frac{e^2qQ}{h}\right)\times\left\{S_{zz}[T]\cdot\left(\frac{3}{2}\cos^2\beta_{R,Q}^i - \frac{1}{2} + \frac{\eta}{2}\sin^2\beta_{R,Q}^i\right)\right.$$

$$\left. + \Delta_{biaxial}\left[\sin^2\beta_{R,Q}^i + \frac{\eta}{3}\left(\cos^2\beta_{R,Q}^i + 1\right)\right]\right\}, \tag{1.38}$$

where $\Delta_{biaxial}$ is a molecular biaxial parameter and is $(S_{xx} - S_{yy})$, $\beta^i_{R,Q}$ is the angle between the C-D bond and the *para* axis of the phenyl ring of the molecule 8BEF5 to be discussed in Chapter 4. When the quadrupolar interaction is cylindrically symmetric (η = 0), and the Euler angle α = 0º [in Eq. (1.37)], Eq. (1.38) goes back to Eq. (1.37).

In lyotropics, the doublet spacing $\Delta\nu$ depends on a) the orientation of the average surface normal at a particular site w.r.t. the symmetry axis of the aggregate (angle "Φ"), b) the orientation of symmetry axis of the aggregate w.r.t. the magnetic field (angle "Θ"). Fig. 1.4 shows the lamellar phase structure and these angles. Thus, the quadrupolar splitting of the nitrogen in the head group of the molecule can be expressed as [23,24]

$$\Delta\nu_N = \frac{3}{2}\left(\frac{e^2qQ}{h}\right)S_{CN}\left(\frac{3\cos^2\Phi - 1}{2}\right)\left(\frac{3\cos^2\Theta - 1}{2}\right) \tag{1.39}$$

where S_{CN} is the segmental order parameter of the nitrogen.

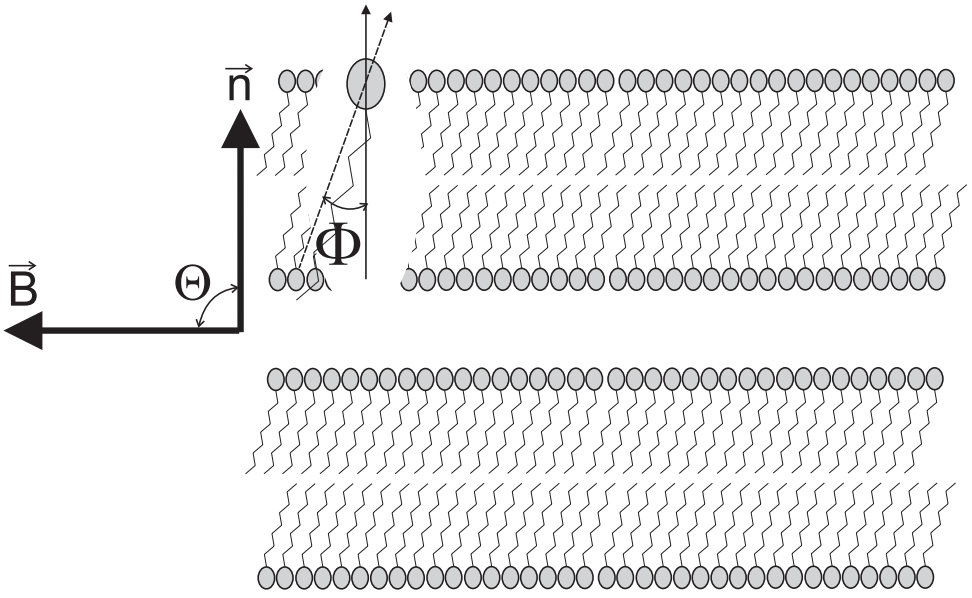

Fig. 1.4 Schematic diagram of the lamellar phase and the orientation of the molecules. $\vec{B}$ is the external field and $\vec{n}$ is the average surface normal. The tilted axis on the enlarged molecule is the symmetry axis of the aggregates. Water flows within the layers

Mathematics of Solid Echo Sequence

To investigate how the radiofrequency pulses affect a spin system, it is helpful to examine the evolution of the density matrix in a quantum picture [6]. The so-called "solid echo" pulse sequence [25] $90°_{+x} - \tau - 90°_{+y} - \tau - echo$, where $\tau < T_2$, serves as a good example to illustrate the advantage of quantum mechanics. By ignoring the chemical shift and at exact resonance, the Hamiltonian in the rotating frame is

$$H = \omega_Q Q_z + \omega_1 I_x \tag{1.40}$$

The spins, initially in I_z state, flip to $-I_y$ state after a $90°_x$ pulse. Then under the quadrupolar interaction $\omega_Q Q_Z$, the spins precess at different rates causing them to fan out in the $I_y - J_y$ plane. So at the instant before the second pulse, the density matrix for each spin packet is

$$\sigma(\tau) = -I_y \cos\omega_Q\tau + J_y \sin\omega_Q\tau \tag{1.41}$$

A y direction pulse does not affect I_y but causes J_y to precess in the "$J_y - K_y$ plane" at $-2\omega_1$. The density matrix just after the second pulse is

$$\sigma(\tau^+) = -I_y \cos\omega_Q\tau + (J_y \cos 2\phi - K_y \sin 2\phi)\sin\omega_Q\tau \tag{1.42}$$

and when $\phi = 90°$,

$$\sigma(\tau^+) = -I_y \cos\omega_Q\tau - J_y \sin\omega_Q\tau \tag{1.43}$$

This corresponds to a quadrupolar echo experiment. Further evolution under the quadrupolar interaction makes the dephased spin packets to refocus on the $I_y - J_y$ plane:

$$\sigma(\tau + t) = (-I_y \cos\omega_Q t + J_y \sin\omega_Q t)\cos\omega_Q\tau - (J_y \cos\omega_Q t + I_y \sin\omega_Q t)\sin\omega_Q\tau$$

$$= -I_y \cos\omega_Q(t-\tau) + J_y \sin\omega_Q(t-\tau) \tag{1.44}$$

and at time $t = \tau$,

$$\sigma(2\tau) = -I_y \tag{1.45}$$

So the spins refocus after time 2τ.

Frame Transformation

The description of the orientation of a molecule in liquid crystals, where the molecule is rotating and diffusing, is more complex. It is necessary to define the director reference frame (D), x^{Dir}, y^{Dir}, z^{Dir}. Euler angles (α,β,γ) between *x*, *y* and *z* axes of two frames are employed to describe the rotational transformation. In detailed study of the motion of the nuclei at a particular site inside a molecule, the segmental frame (S) and the Principal Axis System (PAS) where the interactions take place should be included in addition to molecule-fixed frame (M) and laboratory frame (L). A particular link among these frames by successive transformations is

The Laboratory frame (L) $\xleftrightarrow{(\alpha_{LD},\beta_{LD},\gamma_{LD})}$ The Director reference frame (D)

$\xleftrightarrow{(\alpha_{DM},\beta_{DM},\gamma_{DM})}$ The Molecule-fixed frame (M) $\xleftrightarrow{(\alpha_{MS},\beta_{MS},\gamma_{MS})}$

The Segmental frame (S) $\xleftrightarrow{(\alpha_{SP},\beta_{SP},\gamma_{SP})}$ The Principal Axis System (PAS)

Actually, the orientation for the director frame fluctuates continuously and is spatially random. The time-dependent director orientation can make an appreciable or even a dominant contribution to the spin relaxation. Thus it is necessary to differentiate between an instantaneous director, for which $\mathbf{n_x}$, $\mathbf{n_y}$, and $\mathbf{n_z}$ will be time-dependent, and the time-averaged director. This is needed to describe order director fluctuations [6].

References

[1] E.M.Purcell, H.C.Torrey, and R.V.Pound, Phys. Rev. **69**, 37 (1946).

[2] F.Bloch, W.W.Hansen, and M.Packard, Phys. Rev. **69**, 127 (1946).

[3] C.P.Slichter, *Principles of Magnetic Resonance*. (Springer-Verlag, Berlin, Heidelberg, New York, London, Paris, Tokyo, Hong Kong, 1989).

[4] F.Reinitzer, Monatsh Chem. **9**, 421 (1888).

[5] O.Lehmann, Z. Phys. Chem. **4**, 462 (1889).

[6] R.Y.Dong, *Nuclear Magnetic Resonance of Liquid Crystals*, 2nd ed. (Springer, New York, 1997).

[7] Author (2002).The Basics of NMR. Retrieved Mar 15, 2005, Magnetic Resonance Laboratory, Rochester Institute of Technology. Web Site: http://www.cis.rit.edu/htbooks/nmr/inside.htm

[8] C.N.Chen and D.I.Hoult, *Biomedical Magnetic Resonance Technology*. (Adam Hilger, Bristol, 1989).

[9] R.P.Feynman, R.B.Leighton, and M.Sands, *The Feynman Lectures on Physics*. (Addison-Wesley, Reading, 1964).

[10] C-N.Chen and D.I.Hoult, *Biomedical Magnetic Resonance Technology*. (Adam Hilger, Bristol, 1989).

[11] T.C.Farrar and E.D.Becker, *Pulse and Fourier Transform NMR*. (Academic Press, New York, 1971).

[12] R.J.Abraham, J.Fisher, and P.Loftus, *Introduction to NMR Spectroscopy*. (John Wiley & Sons, Chichester, 1992).

[13] E.L.Hahn, Phys. Rev. **80**, 580 (1950).

[14] Author (1999).NMR Advanced Course. Retrieved Apr 15, 2005, Department of Chemistry, Queens University. Web Site: http://web.chem.queensu.ca/FACILITIES/NMR/nmr/webcourse/

[15] A.Abragam, *The Principles of Nuclear Magnetism*. (Clarendon, Oxford, 1961).

[16] T.C.Farrar, *Introduction to Pulse NMR Spectroscopy*. (Farragut, Wisconsin, 1989).

[17] E.Fukushima and S.B.W.Roeder, *Experimental Pulse NMR-A Nuts and Bolts Approach*. (Addison-Welsey, Reading, Massachusetts, 1981).

[18] D.I.Hoult and N.S.Ginsberg, J. Magn. Reson. **148**, 182 (2001).

[19] C.A.Veracini, in *Nuclear Magnetic Resonance of Liquid Crystals*, edited by J.W.Emsley (Reidel, Dordrecht, 1985), Vol. 141, pp. 99.

[20] W.Maier and A.Saupe, Nature **14a**, 882 (1959).

[21] W.Maier and A.Saupe, Nature **15a**, 287 (1960).

[22] R.Y.Dong, J.W.Emsley, and K.Hamilton, Liq. Cryst. **5**, 1019 (1989).

[23] J. Charvolin and Y.Hendrikx, *NMR of Liquid Crystals*. (Reidel, Dordrecht, 1985).

[24] M.Wachowicz, S.Jurga, and M.Vilfan, Phys. Rev. E **70**, 031701 (2004).

[25] J.G.Powles and P.Mansfield, Phys. Lett. **2**, 58 (1962).

2 Liquid Crystals and Experimental Methods

2.1 Mesophases in Thermotropic Liquid Crystals

Liquid crystals have traditionally been divided into two broad classes: *thermotropic* and *lyotropic* liquid crystals. Thermotropic liquid crystals are generally formed by organic molecules, whose mesomorphic behaviours arise from changing the *temperature*. Lyotropic liquid crystals gain anisotropic properties from mixing two or more components. Here, both the *concentration* of mesogenic materials and/or the temperature can induce various mesophases. Due to the existence of long range orientational order in liquid crystals, molecules are preferably aligned along a particular direction in space, labeled by the local director $\hat{n}$. The *diamagnetic susceptibility* of a liquid crystal is anisotropic, due to the shape anisotropy of the molecules. The diamagnetic susceptibility χ has two principal components in an uniaxial phase, where $\chi_{//}$ is the component along the director, while $\chi_{\perp}$ is that perpendicular to the director. If the diamagnetic susceptibility anisotropy $\Delta\chi\ (=\chi_{//}-\chi_{\perp})$ is positive, the director will align along the magnetic field. This is favoured by most rod-like molecules, while a negative $\Delta\chi$ is common for disc-like molecules. A typical rod-like liquid crystal molecule has 20~30Å in length and ~5Å in width.

Before discussing the mesophases of a liquid crystal, it is beneficial to take a look at the isotropic phase, as shown in Fig. 2.1a, which is a completely disordered liquid. In the isotropic phase, molecules possess no long range *positional* or *orientational* order. The

isotropic liquid has a low viscosity and is clear. Actually, some short-range order may exist in the isotropic phase of liquid crystals, i.e. over a short length scale of a few molecular distances. The short-range orientational order parameter is non-zero but small.

The Nematic Phase

The nematic phase (see Fig. 2.1b) has a long-range orientational order [1] because the molecules tend to align along $\hat{n}$. However, positional order of molecular centres is still absent. The reason is, at a certain temperature the thermal energy may be sufficient to destroy the positional order of a solid but not enough to destroy its orientational order. Macroscopically, these materials show anisotropic properties, such as refractive index, dielectric constant and light scattering. Nematic phase is apolar, since $+\hat{n}$ and $-\hat{n}$ are equivalent. In addition, most thermotropic nematics known so far are uniaxial, due to the rotational symmetry around the director $\hat{n}$. The orientational order of molecules can be described by a second-rank tensor in the first approximation. In the case of rod-like molecules, this order is specified by an order parameter $S=\langle P_2(\cos\theta)\rangle$, where θ is the angle between the rod axis and the director.

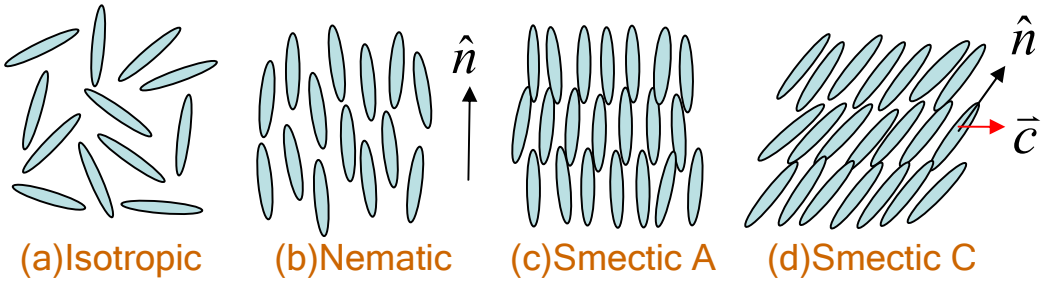

Fig. 2.1 Being cooled down, (a) an isotropic phase could form (b) a nematic phase with the director, (c) a smectic A phase with the director or (d) a smectic C phase with two vectors for ordering.

Let us now consider the nematic-isotropic phase transition, where the long-range

orientational order is suddenly destroyed upon heating, and the order parameter S drops discontinuously from a nonzero value to zero. This first order transition temperature T_c is also known as the *clearing point*. This behaviour was successfully interpreted by Maier and Saupe [2,3]. Assuming that anisotropic dispersion forces are responsible for the nematic order among the molecules, they have proposed an orientational pseudo-potential

$$V(\theta) = -\varepsilon \langle P_2(\cos\theta) \rangle P_2(\cos\theta), \tag{2.1}$$

where the parameter ε scales the intermolecular interaction. The orientation of molecules in a mesophase can be specified by a singlet distribution function $f(\Omega)$, where Ω denotes the Euler angles (ϕ, θ, φ) involved in transforming between the molecular frame and the director frame. $f(\Omega)$ originates from this orientational pseudo-potential $V(\Omega)$ according to,

$$f(\Omega) = \exp\{-\beta V(\Omega)\} / Z, \tag{2.2}$$

where $\beta = 1/k_B T$ and Z is the single-molecule partition function

$$Z = \int d\Omega \exp\{-\beta V(\Omega)\}. \tag{2.3}$$

The average of any single molecule property $X(\Omega)$ over the orientations of all molecules is defined by

$$\langle X \rangle = \int_0^{2\pi} d\phi \int_0^{\pi} d\theta \sin\theta \int_0^{2\pi} d\varphi X(\Omega) f(\Omega). \tag{2.4}$$

If $X = P_L(\cos\theta)$, then the generalized order parameter $\langle P_L \rangle$ is given by

$$\langle P_L \rangle = \int_0^1 P_L(\cos\theta) f(\cos\theta) d(\cos\theta). \tag{2.5}$$

Among all the orientation order parameters of different ranks, only $\langle P_2 \rangle$ can be determined from the dipolar or quadrupolar splittings in NMR spectra [4]. Due to the fourth-rank

tensor nature of the scattering interaction, $\langle P_2 \rangle$ and $\langle P_4 \rangle$ are accessible by the Raman scattering technique. Although it is usually not straightforward, $\langle P_4 \rangle$ can also in principle be obtained from nuclear spin relaxation [5].

The Smectic A Phase

The word smectic has a Greek origin, i.e. 'smectos', which means 'soap-like'. Besides the orientational order, molecules arrange themselves into layers and show some degree of positional order, as the molecular centres of mass are arranged on the average in equidistant planes (see Fig. 2.1c). Additional phase symmetry properties are used to distinguish different smectic phases, with a label from A to I.

In the smectic A phase, the director $\hat{n}$ is parallel to the normal of the smectic layers. The layers form a one-dimension density wave. Due to the freedom of motion of molecules within the layers, SmA phase could be considered a two dimensional liquid.

The Smectic C Phase

Molecules in the SmC phase (see Fig. 2.1d) differ from those in the SmA phase by tilting themselves at an angle θ with respect to the layer normal. This tilt angle θ depends on the compound, and for a given compound, it can vary over a range of temperature or stay relatively constant. This phase is biaxial. Besides the director $\hat{n}$, its projection onto the layer defines another ordering direction $\vec{c}$.

The Chiral Nematic (Cholesteric) Phase

'*Chiral*' means handedness, or means molecules arrange themselves such that they share the same local director in each of the nematic layers. These local directors form a screw

framework, either right-handed, or left-handed. The molecules contain a chiral centre and have intermolecular forces that favour the alignment of molecules at a slightly different angle to one another. This leads to the formation of a helical structure which can be visualized as a stack of very thin 2-D nematic-like layers with the director in each layer twisted with respect to those above and below [6]. Indeed the local directors of different layers vary continuously from 0º to 360º. This 360º rotation of $\hat{n}$ is completed over a distance of *p*, called the *pitch*, and the direction of *p* is called the pitch axis, which is perpendicular to all $\hat{n}$. The pitch length is usually of the order of the wavelength of visible light. Light of particular wavelength can be selectively reflected from a sample of chiral nematics. Since a decrease in temperature will increase the degree of twist, thereby shortening the pitch, the colour of the reflected visible light will change accordingly [7]. Twisted nematic liquid crystals have broad applications in the LCD industry [8].

The Chiral Smectic C (Ferroelectric) Phase

Chirality [9] in self-organizing systems can lead to a reduced phase symmetry and can yield a huge variety of novel mesophases with unique structures and properties [10]. Strong chirality, has lead to a series of fascinating frustrated phases, such as Blue Phases (BP) [11] and the Chiral Smectic C phase (SmC* [12]). Similar to the chiral nematic phase, molecular chirality in the SmC* phase leads to a helicodial structure, in which molecules with a tilt angle θ position in each layer but with various azimuthal angle ϕ, from 0º to 360º, at different layers. The tilt θ is dependent on temperature. This phase is also biaxial, but the $\vec{c}$ axis rotates according to the ϕ angle.

Special molecules (e.g. bent shaped dimesogens [10]) can lead to an anticlinic molecular organization (SmC_A), in which the tilt direction alternates between ϕ=0º and 180º from one layer to the next, giving rise to antiferroelectric properties of the corresponding chiral mesophases (SmC^*_A) [13]. Further, at least two subphases occur between the SmC* and the SmC^*_A phases. One of them is the ferri-smectic (SmC^*_γ) phase [13], which has superlattice periodicities consisting of three layers. Fig. 2.2 illustrates these three chrial phases from above and side views.

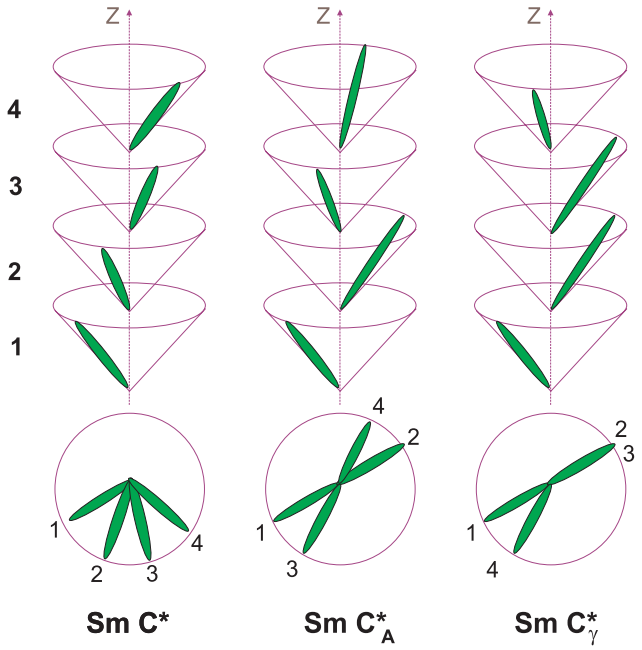

Fig. 2.2 Chiral smectic C (SmC*) phase, antiferroelectric smectic C (SmC^*_A) phase and ferri-smectic C (SmC^*_γ) phase.

For achiral molecules of rigid bent (banana shaped) molecular structure [14], Niori [15] *et al.* observed chirality and polar order of electric dipoles in smectic phases. Here, a polar order within the layer arises from the directed stacking of bent core units to minimize the excluded volume [10]. This leads to several possible smectic phases [16,17], known as B (banana) phases.

The Columnar Phase

The columnar phase is formed by stacking discotic (disc-like) molecules [18]. These molecules tend to stack themselves into columns, and their directors are along the column axis (i.e. perpendicular to the molecular planes). Also, the arrangement of the columns can show different patterns, including hexagonal, rectangular or oblique symmetry.

2.2 Classification of Lyotropic Liquid Crystals

To form a lyotropic liquid crystal, at least two components are needed. One component contains *amphiphilic* molecules, which are composed of a polar head group (which is *hydrophilic*) and a hydrocarbon tail (*hydrophobic*). The other component is the solvent in which amphiphilic molecules reside. Lyotropic liquid crystal exists everywhere in our daily life. Soap in water forms a variety of lyotropic phases. A common soap is sodium dodecylsulphate where an ionic group (sulphate) is attached to a hydrocarbon chain [6]. The sulphate head group is soluble in water while the chain part is quite insoluble. Thus, in a dilute solution, the soap molecules form a spherical structure, called a *micelle*, leaving the soluble head group outside in the water, while keeping the hydrophobic chain inside away from water molecules (see Fig. 2.3). Micelles come in various sizes, but the diameter of the smallest sphere could be of only two molecules' length.

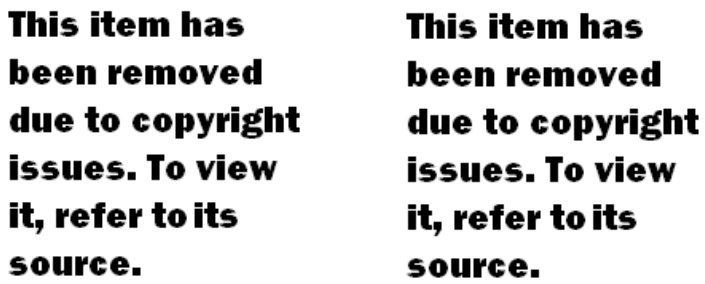

Fig. 2.3 Structure of spherical micelles [6].

The term "critical micelle concentration" (CMC) [19] describes the minimum concentration of the surfactant molecules in the solvent. Above the CMC, micelles are formed. At the CMC the hydrocarbon chains undergo a substantial change in their environment since below this concentration they are interacting mainly with the solvent and above it primarily with each other. This difference may be revealed in nuclear magnetic shielding as changes in the chemical shift of the nucleus of interest. A break in the curve of the chemical shift against concentration usually appears at the CMC [19].

As the concentration increases, the micelles begin to arrange themselves into a *cubic* pattern and then a *hexagonal* pattern. The cubic phase has a structure similar to that of a face-centred or body-centred cubic crystal lattice, though micelles take the place of atoms or ions (note that cubic phases also exist in thermotropic liquid crystals [20]). The hexagonal phase is formed by rod-shaped molecule aggregates, whose surface is composed of hydrophilic heads while the hydrophobic tails are kept inside. Six rods group around a seventh rod, showing a compact and stable structure (see Fig. 2.4).

The *lamellar* phase forms at an even higher concentration. This bilayer structure has molecules arranging their hydrophilic polar heads facing into in the solvent, while

hydrophobic nonpolar tails fill the inside, as also shown in Fig. 2.4.

The viscosities of the three phases, cubic, hexagonal and lamellar, are inversely related to their concentrations, because of their specific structures. The cubic phase is the most viscous among the three, because it lacks a sheer plane that allows sliding of molecules. In contrary, the sheet-like parallel layers that allow sliding on each other help the lamellar phase to gain higher fluidity with less water content. The hexagonal phase is more compact but has somewhat a sliding plane, showing medium viscosity. A typical phase diagram of lyotropic liquid crystals is shown in Fig. 2.4.

This item has been removed due to copyright issues. To view it, refer to its source.

This item has been removed due to copyright issues. To view it, refer to its source.

Fig. 2.4 Phase diagram of a lyotropic crystal as a function of both concentration and temperature [6].The dotted line is the critical micelle concentration. The cubic phase is one of the intermediate phases between the hexagonal and the lamellar phase. The dark boundary line refers to the Kraff temperature, below which few liquid crystalline state form.

The phase transitions in Fig. 2.4 can be determined by a number of strategies [19], e.g. polarizing microscopy, differential scanning calorimetry, X-ray diffraction and proton NMR linewidth study, where an abrupt discontinuity in linewidth occurs at the phase transition.

In lyotropic systems, intermediate phases between the lamellar and the columnar (here hexagonal in Fig. 2.4) organization can provide a wide variety of complex meso-morphologies [9]. The bicontinuous cubic phases and non-cubic intermediate phases (rhombohedral phases, tetragonal phases and different mesh phases) represent possible phases between the lamellar and the columnar organization. They are summarized in Fig. 2.5 [10].

Fig. 2.5 Intermediate phases occurring at the transition between the lamellar smectic and the columnar organization of amphiphilic molecules [21-25]. Though the shown phases have mostly been found in lyotropic systems [26], related structures should also be possible for thermotropic intermediate phases.

If the concentration of micelles is such that their weight of amphiphilic molecules is

greater than that of the water, the molecules can form a spherical structure trapping water droplets inside, with the amphiphilic polar head in contact with the water, and the nonpolar tails isolated on the outside. This is shown in Fig. 2.6a. Another scenario occurs when the micelles are dissolved in a nonpolar solvent. Provided the concentration of micelles is low, the molecules can form the same structure, called an 'inverse micelle'.

Fig. 2.6 (a) Cross section of an inverse micelle and (b) Cross section of a vesicle [6].

Surfactants dissolved in water can also form lyotropic phases. Thus, phospholipids can form another phase, *vesicles* (Fig. 2.6b), other than micelle in dilute solution. Vesicles are bilayers that have folded into a three-dimensional spherical structure, similar to a micelle but with two layers of molecules. Vesicles form because they eliminate the edges of bilayers, protecting the hydrophobic chains from the water at the centre. For a flat bilayer to be without edges, it would have to be infinite. Molecules that form vesicles usually have a fluid double chain and a large optimal area per head group [27]. Lipids found in biological membranes spontaneously form vesicles. Lyotropic liquid crystals are also extremely important because of their role in biological membranes. Membranes are composed of amphiphilic lipids - mostly phospholipids and cholesterol.

Recently, intensive study of novel non-conventional materials has led to novel

mesophases and deeper understanding of the driving force for their self-organization [10]. It is found that besides the molecular shape and space filling effects, nanoscale segregation of incompatible molecular parts (micro segregation), and the minimization of resulting interfaces between these nanoparticles [28] play an important role in mesogenic self assembly, leading to new mesophase morphologies [9,29-31].

2.3 Pulse Sequences

Solid Echo Sequence

The solid echo pulse sequence [32] is a routine way to acquire quadrupolar splittings in a liquid crystal sample. In contrast to liquid state, where the relaxation time is on the order of 1 s, the relaxation time scale in solid is so short such that T_2 is on the order of 100 μs. Since the instrument (e.g. deadtime in NMR probe) cannot response fast enough to capture the full FID over this short time scale, acquiring a true FID signal by a simple 90º pulse is impossible. For τ larger than the deadtime, the trailing half of the solid echo is equal to the true FID [33]. Therefore, the solid echo is a good technique for overcoming the effects of the deadtime in determining the FID shape [34]. By adjusting the echo delay τ, left shifting proper amount of FID data points, the true FID can be obtained.

Various versions of Jeener-Broekaert Sequence

The Jeener-Broekaert (JB) sequence is used in this thesis to measure spin-lattice relaxation times by first maximizing the quadrupolar order, or "spin alignment" according to Spiess [35]. An additional 45º pulse added to the JB sequence can produce the net effect

of subtracting the equilibrium M_∞ signal (the equilibrium magnetization at infinite time) from the JB signal. This would minimize any long-term instability in the NMR signal immediately after the second 45º pulse. Besides, if a deadtime problem occurs, where it is difficult for the spectrometer to observe signal soon after the second 45°_y pulse, a refocusing 90°_y pulse may be added as in the solid echo sequence. When there are several doublets of interest to be measured in the same spectrum, a separate experiment with a specific τ is required to maximize the quadrupolar order of each doublet. Alternatively, broadband excitation may be used to irradiate several doublets identically using a Broadband JB (BBJB) sequence, or called Wimperis sequence [36,37]. This is particularly useful if the NMR spectrum represents a powder sample. Also, the BBJB has the advantage of saving time on a relaxation experiment. The BBJB sequence with M_∞ subtraction and proper phase cycling is routinely used to measure spin-lattice relaxation times (Fig. 2.7) in the present work.

To calculate both T_{1Z} and T_{1Q} from the decay curve composed by the 15 measurements, the sum $S(t)$ and difference $D(t)$ of the spectrum and its reverse w.r.t. Larmor resonance frequency, are given by

$$S(t) \propto \exp(-t/T_{1Z}) \tag{2.6}$$

$$D(t) \propto \exp(-t/T_{1Q}) \tag{2.7}$$

The BBJB sequence – M_∞ sequence works successfully with the ^{2}H study. However, when it came to ^{14}N T_1 measurements, spectra in a relaxation measurement require proper phase correction [34]. The way of phase correction in our ^{14}N NMR was verified by

employing different versions of JB sequences.

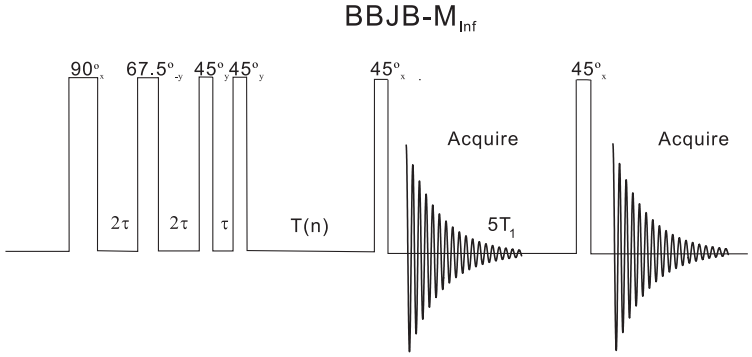

Fig. 2.7 Pulse diagram of BBJB-M_∞ sequence. Recycle delay after the 5th pulse is to $5T_1$ when the magnetization fully recovers. In the pulse sequence, T(n) is a list of times within the relaxation time scale. In practice, 15 points of different T(n), are used to obtain partially relaxed spectra.

2.4 Apparatus

We used a Bruker Avance 400 spectrometer with 9.1 tesla superconducting magnet. ^{2}H is measured at 61.4 MHz and ^{14}N at 28.9 MHz. The sample temperature was regulated by an air flow to better than 0.1ºC. A pulse width about 3 μs was employed in the two-channel probe to obtain an optimized 90º pulse for ^{2}H. ^{2}H relaxation data of 8BEF5 were collected for aromatic deuteron sites 'a' and 'b', and the deuterons at the methylene C_α, by measuring their Zeeman (T_{1Z}) and quadrupolar (T_{1Q}) spin-lattice relaxation times. Relaxation delay of 200 ms was used and the number of scans for signal averaging was 128. The uncertainty of T_{1Z} and T_{1Q} measurements was estimated to be less than 5%. In the BBJB sequence, the delay time τ between the first and the second pulse (see Fig. 2.7) was set accordingly [38] to make the efficient irradiation on the splitting peaks of interest. In other words, to produce a more pronounced difference between right peak and left peak. The best scenario of the quadrupolar order was when the left component of the

doublet totally disappeared in the BBJB-M_∞ sequence. In the lyotropic measurements, the samples were in 4 mm NMR tubes to save the amount of deuterated materials. The relaxation times of five deuterium doublets vary significantly, ranging from 50 ms for ^2H at carbon site 1 (near the head group) to over 1 s for ^2H at carbon 10 (at the end of chain). For ^{14}N lyotropic study, the lyotropic samples were sealed in 7.5 mm NMR tubes. A pulse width of 3.7-3.9 μs was used for ^{14}N in a single-channel ^{14}N probe. The dwell time was 2 μs and the corresponding spectral width was ±250 kHz. A signal averaging of 16k scans was routine in the literature [39,40], while here the number of scans was up to 8k. An excitation delay τ of 5 μs to 20 μs was used at different temperatures according to the splitting of ^{14}N doublet. At lower temperature, a τ of less than 4 μs between the first and the second pulse was found to give a better broadband irradiation.

2.5 Liquid Crystal Samples

Chiral Smectic Sample 8BEF5

The smectogen (S)-[4-(2-methyl-butyl) phenyl]-4'-n-octybiphenyl carboxylate (8BEF5) exhibits a variety of mesophases, and was investigated in a previous study [4]. Our 8BEF5-d_{15} sample (in 5 mm NMR tube) was kindly provided by Dr. C.A.Veracini, University of Pisa. It was specifically deuteriated at the aromatic and alpha carbon sites, and is shown in Fig. 4.1, while the other methylenic sites were accidentally deuteriated during the synthesis, resulting in much lower intensities for these sites.

The smectic-isotropic transition temperature is 408 K. The sample shows powder pattern

before its alignment at high temperature (>380 K) by the external field. By melting it completely in isotropic phase, the sample gains a well defined monodomain in both SmA and SmC* phases after cooling down slowly.

Lyotropic Sample DACl/H_2O Binary System at Lamellar Phase

The decylammonium chloride (DACl)/H_2O binary system is popular as a model system in the study of lyotropic liquid crystals [41,42] and biological membrane system. It belongs to a family of long-chain cationic surfactants, whose family members are different by the number of carbons and the type of the halides [43,44]. At higher DACl concentrations, a variety of mesophases are formed, including hexagonal phase, lamellar phase, nematic and micellar isotropic phase. The DACl was synthesized by C. Morcombe, Brandon University. Two non-deuterated DACl/H_2O (54 wt.%) and DACl/H_2O (56 wt.%) samples were packed into 7.5 mm NMR tubes. The two selectively deuterated 1,9,10-DACl-d_7 and 2,3-DACl-d_4 were provided by Dr. A. S. Tracey, Simon Fraser University. These two kinds of deuterated DACl crystal powders were mixed to a weight ratio of 2 to 1, then were used as the solute 1,2,3,9,10-DACl-d_{11} and mixed with doubly-distilled water to prepare samples in different concentrations for ^2H study. The experimental ^2H NMR investigation was focused on a series of samples with concentrations chosen to cover interesting regions of the DACl/H_2O phase diagram (Fig. 2.8) [45]. They contained 54, 56, 59 wt.% of 1,2,3,9,10-DACl-d_{11} in H_2O to study the lamellar phase behavior. 1,9,10-DACl-d_7 and 2,3-DACl-d_4 were also mixed respectively with water, and both were at the 54 wt.%, for reference. The uncertainties in sample concentrations were estimated

to be less than 2%. By measurements of sample containing only one kind of selectively deuterated material [46], it is found that the C_2, C_3 doublets appear indistinguishable and thereby only one quadrupolar splitting and relaxation can be recorded. On the other hand, in the lamellar phase of 1,9,10-DACl-d_7/H_2O, besides the $\Delta\nu_1$, $\Delta\nu_9$ and $\Delta\nu_{10}$, an additional weak splitting appeared, which is probably deuterated accidentally at the carbon site between C_4 and C_8. We named this C_X. Thus, in total, there are five doublets in the combined deuterated lyotropic samples.

Fig. 2.8 Phase diagram of DACl/H_2O binary system is reproduced [45].

To align these lyotropic samples in the lamellar phase quickly, heating outside the magnet into fluid state is necessary before putting the samples into the superconducting magnet bore. However, the samples were usually not well aligned when first cooled down into the lamellar phase. The signal to noise was poor especially for doing relaxation

experiments. Then the sample must be heated up again and be kept at some high temperature for a few hours then cooled down slowly. This kind of process was repeated several times until a well aligned sample was achieved. A deuterated 54 wt.% sample was heated to 345 K into the micellar isotropic phase, the deuterated 56 wt.% one to 360 K and the deuterated 59 wt.% one was 410 K. Before completely becoming isotropic, a lamellar-isotropic biphasic region extending 10-20 degree appears, whose span corresponds the phase diagram reported earlier [45] by polarizing microscopy. The boundary of the biphasic regions was actually determined by the onset of relatively temperature-insensitive splittings and the existence of an isotropic peak between the doublets in the spectrum. In fact, this isotropic peak exists for quite a large temperature range in the lamellar phase. The phases and transitions temperatures are summarized in Table 2.1.

Table 2.1 Transition temperatures determined for the samples used in both ^{2}H and ^{14}N studies.

Sample wt.%	Phases and transition temperatures
54	$\text{lamellar} \xrightarrow{334K} \text{lamellar+isotropic} \xrightarrow{345K} \text{isotropic}$
56	$\text{lamellar} \xrightarrow{342K} \text{lamellar+isotropic} \xrightarrow{357K} \text{isotropic}$
59	$\text{lamellar} \xrightarrow{380K} \text{lamellar+isotropic} \xrightarrow{410K} \text{isotropic}$

2.6 Sample Preparation of Lyotropic Samples

The decylammonium chloride (DACl)-D_2O binary system was prepared at a serial of concentrations (38 wt.%.~59 wt.%) in NMR tubes for mapping the phase diagram and ^{14}N study, while the deuterated DACl-H_2O (doubly distilled) binary system of

corresponding concentrations for ^2H relaxation study. The preparation methods were surveyed [39,41,45,47,48], and detailed procedures and precautions in preparing a particular DACl/D_2O (43.0 %w.t.) sample carried out are given here.

A. Solute Weighing and Solvent Injection

DACl was weighed to an accuracy of 1 mg and then put into a small clean bottle with a microbar in it. 15 spoons of DACl weigh around 120mg of DACl. A 180-250 mg well-mixed mixture could be good for one transfer into a 4 mm NMR tube, while 350-400 mg for a 5 mm tube and 650-750 mg for a 7.5 mm tube. These vary somewhat depending on the concentration and viscosity of the mixture.

A 50 μL syringe was used to inject D_2O (H_2O) to the bottom of bottle at the first shot to let them mix easily; DACl on the wall inside was flushed down at later shots. Some drops left at the opening of the bottle were used for later concentration correction if required. For D_2O, 100 μL equals around 110 mg.

B. Mixing

Before the bottle was capped, teflon tape was used around the opening of the glass bottle for a few turns to make a thin film before capping the bottle to prevent water loss. Then the gap between the cap and the bottle was glued by putting pre-mixed epoxy (30 min before) and then drying the glue for a day. The sample was then stirred on a magnetic Stirrer/Hot plate by the microbar for over 1 hr at room temperature. For higher DACl concentration (>48% wt), the bubbles introduced by fast stirring made the mixture looked like white soap, indicating a well mixed sample. After centrifuging the bottle for over 30

min, a layer of condensed bubble remains on the top of the clear mixture, these bubbles were reduced by centrifuged up and down for 2 times, each for 5 min. To mix the sample in isotropic phase, the bottle was stirred while immersing into high temperature oil which was heated above the predicted phase transition temperature (usually >70 ºC). In high concentration case, mixture might need to go as high as 110 ºC to reach isotropic phase, then the mixture was cooled down out of the oil bath. Finally, the mixture would become clear liquid without bubble. The water vapor left on the inner wall was removed by rolling mixture over the bottle to cover all the area of the inner wall and then centrifuging up and down 3 times, each for 10 min. The whole process was cycled for a second time until transparent homogenized mixture was obtained. Typically, the sample was equilibrated at room temperature for a least 1 hr before transferring.

C. Transferring and Sealing

Since DACl/ D_2O lyotropic mixtures remained in micellar phase at room temperature, we could transfer it into a NMR glass tube at room temperature at ease. If necessary, everything was pre-cooled below room temperature (at 5~15 ºC) before transferring. High temperature (in isotropic phase above the hexagonal or lameller region) transferring would not work because the sample cooled down quickly and became too viscous to flow and sticked on the pipette in a few seconds.

Before transferring, the cap was sawed out halfway carefully. To avoid dust dropping into the mixture, the saw dust was cleaned with wet napkin constantly. A constriction on the sample tube was made by a propane flame. Longer tube would make sealing easier. The

mixture was sucked gently and transferred to the bottom of the NMR tube. Great care was needed to prevent leaving mixture on the upper part of the NMR tube. If a big amount mixture stayed at the wide junction of pipette and it could not be blown out, then waited for a while till it flowed into the fine tip region. The opening of the sample tube was capped by a parafilm tape to prevent water loss and was frozen a bit and then centrifuged to get rid of the bubbles.

To seal the NMR tubes, the chemicals on its inner wall must be cleaned with ethanol after freezing the sample by liquid nitrogen in advance. Otherwise, the chemicals will be burnt during sealing and cause the sample not to seal at all. The sample must be constantly and completely frozen for degassing and sealing. Then the sample tube was plugged into a vacuum system to gain a reduced pressure for easy sealing. A propane gun was used to seal at the constriction. Finally, the sample was equilibrated in room temperature for a week before experiment.

References

[1] R.Y.Dong, *Nuclear Magnetic Resonance of Liquid Crystals*, 2nd ed. (Springer, New York, 1997).

[2] W.Maier and A.Saupe, Nature **14a**, 882 (1959).

[3] W.Maier and A.Saupe, Nature **15a**, 287 (1960).

[4] D.Catalano, L.Chiezzi, V.Domenici, M.Geppi, C.A.Veracini, R.Y.Dong, and K.Fodor-Csorba, Macromol. Chem. Phys. **203**, 1594 (2002).

[5] P.L.Nordio and U.Segre, *The Molecular Physics of Liquid Crystals*. (Academic Press, New York, 1979).

[6] W.L.Gordon, J.L.Koenig, P.G.Cramer, J.Graff, and R.Lazebnik (2004). Liquid Crystals. Retrieved Feb 3, 2005, from Polymers & Liquid Crystals, Case Western Reserve University. Web Site:http://plc.cwru.edu/tutorial/enhanced/files/textbook.htm

[7] T.J.Sluckin, Contemp. Phys. **41**, 37 (2000).

[8] B.Bahadur, *Liquid Crystal: Applications and Uses*. (World Scientific, Singapore, 1992).

[9] C.Tschierske, Ann. Rep. Progr. Chem. C **97**, 191 (2001).

[10] C.Tschierske, Curr. Opin. Colloid Interf. Sci. **7**, 69 (2002).

[11] B.Pansu, Mod. Phys. Lett. B **13**, 769 (1999).

[12] R.B.Meyer, L.Liebert, L.Strzelecki, and P.Keller, J. Phys. Lett. **36** (L69) (1975).

[13] A.Fukuda, Y.Takanishi, T.Isozaki, K.Ishikawa, and H.Takezoe, J. Mater. Chem. **4**, 997 (1994).

[14] G.Pelzl, S.Diele, and W.Weissflog, Adv. Mater. **11**, 707 (1999).

[15] T.Niori, F.Sekine, J.Watanabe, T.Furukawa, and H.Takezoe, J. Mater. Chem. **6**, 1231 (1996).

[16] A.Eremin, S.Diele, and G.Pelzl, Phys. Rev. E **64**, 051707 (2001).

[17] A.Jakli, D.Kruerke, H.Sawade, and G.Heppke, Phys. Lett. **86**, 5715 (2001).

[18] S.Chandrasekhar, B.K.Sadashiva, and K.A.Suresh, Pramana **9**, 471 (1977).

[19] C.L.Khetrapal, A.C.Kunwar, A.S.Tracey, and P.Diehl, *Lyotropic Liquid Crystals: Nuclear Magnetic Resonance Studies in Lytropic Liquid Crystals.* (Springer-Verlag, New York, Heidelber, Berlin, 1975).

[20] S.Diele and P.Goring,"Thermotropic cubic mesophases" in *Handbook of liquid crystals*, edited by D.Demus, J.Goodby, G.W.Gray, H.W.Spiess, and V.Vill (Wiley-VCH, Weinheim, 1998), Vol. 2B, pp. 887.

[21] MC.Holmes, Curr. Opin Colloid Interf. Sc. **3**, 485 (1998).

[22] M.Antonietti and C.Goltner, Angew. Chem. Int. Ed. Engl. **36**, 910 (1997).

[23] M.Leaver, A.Fodgen, M.Holmes, and C.Fairhurst, Langmuir **17**, 35 (2001).

[24] M.Imai, A.Saeki, and T.Teramoto, J. Chem. Phys. **115**, 10525 (2001).

[25] H.Hasglatt, O.Soderman, and B.Jonnsson, Liq. Cryst. **17**, 157 (1994).

[26] JM.Seddon and RH.Templer,"Polymorphism of lipid-water systems" in *Handbook of biological physic*, edited by R.Lipowsky and E.Sackmann (Elsevier, Amsterdam, 1995), Vol. 1, pp. 97.

[27] D.R.Fattal, D.Andelman, and A.Ben-Shaul, Langmuir **11**, 1154 (1995).

[28] W.Chen and B.Wunderlich, Macromol. Chem. Phys. **200**, 283 (1999).

[29] G.Stebani, G.Lattermann, M.Wittenberg, and JH.Wendorff, J. Mater. Chem. **7**, 607 (1997).

[30] C.Tschierske, J. Mater. Chem. **8**, 1485 (1998).

[31] C.Tschierske, J. Mater. Chem. **11**, 2647 (2001).

[32] J.G.Powles and P.Mansfield, Phys. Lett. **2**, 58 (1962).

[33] J.G.Powles and J.H.Strange, Proc. Phys. Soc. **82**, 6 (1963).

[34] E.Fukushima and S.B.W.Roeder, *Experimental Pulse NMR-A Nuts and Bolts Approach*. (Addison-Welsey, Reading, Massachusetts, 1981).

[35] H.W.Spiess, J. Chem. Phys. **72**, 6755 (1980).

[36] S.Wimperis, J. Magn. Reson. **86**, 46 (1990).

[37] J. Jeener and P.Broekaert, Phys. Rev. **157**, 232 (1967).

[38] G.L.Hoatson, J. Magn. Reson. **94**, 152 (1991).

[39] R.Y.Dong, Mol. Phys. **99**, 637 (2001).

[40] R.Y.Dong, E.Tomchuk, J.J.Visintainer, and E.Bock, Mol. Cryst. Liq. Cryst. **33**, 101 (1976).

[41] M.Wachowicz, S.Jurga, and M.Vilfan, Phys. Rev. E **70**, 031701 (2004).

[42] M.Tornblom, R.Sitnikov, and U.Henriksson, J. Phys. Chem. B **104**, 1529 (2000).

[43] G.J.Kruger, M.Rademeyer, and D.G.Billing, Acta Cryst. E **59**, o480 (2003).

[44] M.Gorden, Acta Cryst. **6**, 739 (1953).

[45] M.R.Rizzatti and J.D.Gault, J. Colloid and Interface Sci. **110**, 258 (1986).

[46] R.Y.Dong, Chem. Phys. Lett. **375**, 517 (2003).

[47] Stefan Jurga Marcin Wachowicz, Marija Vilfan, Phys. Rev. E. **70**, 031701 (2004).

[48] J.D.Gault, M.A.Leite, M.R.Rizzatt, and H.Gallardo, J. Colloid and Interface Sci. **122**, 587 (1988).

3 Relaxation Models of Liquid Crystals

3.1 Correlation Function and Spectral Density

In NMR spectroscopy, correlation functions of the orientation of atom-atom vectors are of prime importance. Correlation times that describe the rate of molecular reorientation are derived from these. The time correlation function [1] is of great value for the analysis of dynamical processes in condensed phases. When a time-dependent quantity $A(t)$ is multiplied by itself at a different time, it is called an auto-correlation function. But if $A(t)$ is multiplied by another time-dependent quantity $B(t')$ evaluated at time t', it is called a cross-correlation function. Both products are averaged over some equilibrium ensemble. For example, an autocorrelation function for a property, A, measures the correlation between the value of $A(0)$ at an arbitrary initial time and its value at a later time t, $A(t)$. The normalized autocorrelation function for A is defined as:

$$G^{Auto}(t) = \frac{\langle A(t)A(0)\rangle}{\langle A(0)A(0)\rangle}, \tag{3.1}$$

where the brackets imply an ensemble average. In molecular systems undergoing stochastic fluctuations, this function varies from a maximum of 1 at $t = 0$, to a value of zero at long times, where all correlation between the initial and current A values has been lost.

In Eq. (1.20), under the assumption that the PAS frame is rigid in the molecular frame, i.e. the Euler angles between the two frames are time independent, $G_{m_L}(t)$ may be

evaluated in terms of the Wigner rotation matrix $D^2_{m_L m_M}(\Omega_{LM})$ in the fluctuating Hamiltonian

$$G_{m_L}(t) = \sum_{m_M} [d^2_{m_M 0}(\theta)]^2 \left\langle \left\{ D^2_{m_L m_M}[\Omega_{LM}(0)] - \overline{D^2_{m_L m_M}} \right\} \times \left\{ D^{2*}_{m_L m_M}[\Omega_{LM}(t)] - \overline{D^{2*}_{m_L m_M}} \right\} \right\rangle . \quad (3.2)$$

Now $\Omega_{LM}(\equiv \alpha, \beta, \gamma)$ denotes the Euler angles that transform from a molecular frame fixed on the molecular core to the laboratory frame, θ is the angle between the z_{PAS} axis of the PAS frame (in ^{2}H study, this would refer to the C-D bond) and the z_M axis of the molecular frame, and m_L and m_M are the projection indices for a tensor of rank two in the laboratory and molecular z axes, respectively.

Recall from the chapter 1, the spectral density comes from the Fourier transformation of the autocorrelation function $G_{m_L}(t)$, but now it is a real quantity. For a quadrupole interaction, Eq. (1.20) becomes

$$J_{m_L}(m_L \omega) = \frac{3\pi^2}{2} (q_{CD})^2 \int_0^\infty G_{m_L}(t) \cos(m_L \omega t) dt , \quad (3.3)$$

where the nuclear quadrupolar coupling constant $q_{CD} = e^2 qQ / h$ ($\eta = 0$ is assumed).

On the other hand, spectral densities can be simply related to the measured relaxation rates (T_1^{-1} or T_2^{-1}). In quadrupolar interaction, by using Jeener-Broekaert sequence, Zeeman spin-lattice relaxation time T_{1Z} and quadrupolar spin-lattice relaxation time T_{1Q} are measured simultaneously. ^{2}H T_{1Z} and T_{1Q} relate to the spectral densities $J_m(m\omega_0, \Theta)$ for the director oriented at an angle Θ with respect to the external magnetic field as follows [2] :

$$\frac{1}{T_{1Q}} = 3J_1(\omega_0, \Theta) \tag{3.4}$$

$$\frac{1}{T_{1Z}} = J_1(\omega_0, \Theta) + 4J_2(2\omega_0, \Theta), \tag{3.5}$$

where ω_0 is the Larmor frequency. For the director aligned along the external magnetic field, Eqs. (3.4) and (3.5) enable the determination of spectral densities $J_1(\omega_0, 0°)$ and $J_2(2\omega_0, 0°)$.

3.2 Rotational Diffusion Model

In a stochastic Markovian process, the orientational correlation function for a uniaxial molecule can be written as

$$G_{mm'n}^{LL'}(t) = \int\int d\Omega_0 d\Omega P(\Omega_0) D_{mn}^{L*}(\Omega_0)\ P(\Omega_0 \mid \Omega t) D_{m'n}^{L'}(\Omega), \tag{3.6}$$

where for simplicity, *m* and *n* are used to represent the m_L, the projection index in the laboratory frame and m_M, the projection index in the molecular frame, respectively. $P(\Omega_0 \mid \Omega t)$ is the conditional probability of finding a molecule at orientation Ω at a time *t* if the orientation of molecule was Ω_0 at *t*=0.

Nordio *et. al* [3-5] proposed the small step rotational diffusion (SRD) model to describe the evolution of the conditional probability $P(\Omega_0 \mid \Omega t)$ where the molecular reorientation in a potential of mean torque takes place through a sequence of small angular steps. The rotational diffusion tensor is diagonalized in a molecular frame.

Uniaxial Molecule in Uniaxial Phases

Taking the simplest situation where an uniaxial molecule reorients in a unixial phase, the

solution to the rotational diffusion equation is discussed in Appendix A.

For $L = 2$ the reduced correlation function [Eq. (A.24)] in the notation of Tarroni and Zannoni is

$$g^2_{m,n}(t) = \sum_k \left(\beta^2_{m,n}\right)_k \exp\left[\left(\alpha^2_{m,n}\right)_k t\right], \tag{3.7}$$

where the decay constants, $(\alpha^2_{mn})_k / D_\perp$, are the eigenvalues of the rotational diffusion matrix, and $(\beta^2_{mn})_k$, the corresponding eigenvectors, govern the relative weights of the exponentials. The diffusional coefficient $D_\perp$ represents tumbling rotation of the molecule about one of its short molecular axes, while $D_\parallel$ the spinning motion about the long molecular axis. Both $D_\perp$ and $D_\parallel$ appear in $(\alpha^2_{mn})_k$.

As an approximation, the correlation functions [Eq. (3.7)] can be written using a single exponential by restricting the sum over K to the leading term,

$$g^2_{m_L m_M}(t) = \left[\left\langle (D^2_{m_L,m_M})^2 \right\rangle - \left(\overline{D^2_{m_L,m_M}}\right)^2 \delta_{m_L,0}\delta_{m_M,0}\right] \times \exp[(\alpha^2_{m_L,m_M})_1 t]$$

$$= \kappa(m_L, m_M)\exp[-t/\tau^2_{m_L,m_M}]. \tag{3.8}$$

Vold and Vold [6] have solved for a cylindrical molecule reorienting in uniaxial mesophases numerically, and using the notation of Vold and Vold, Eq. (3.7) becomes

$$g^{MR}_{m,n}(t) = c_{m,n}\sum_{j=1}^{3} a^{(j)}_{m,n}\exp\left[-t/\tau^{(j)}_{m,n}\right], \tag{3.9}$$

where $c_{m,n}$ represents the mean square of the Wigner rotation matrices,

$$c_{m,n} = \left\langle \left| D^2_{m,n}(\Omega)\right|^2 \right\rangle - \left(\overline{D^2_{00}}\right)^2. \tag{3.10}$$

The correlation times $\tau^{(j)}_{m,n}$ at each temperature depend on the order parameter $\langle P_2 \rangle$ and

on the rotational diffusion tensor components. The $a_{m,n}^{(j)}$ expresses normalized weights of the exponentials whose time constant

$$\left[\tau_{m,n}^{(j)}\right]^{-1} = \frac{6D_{\perp}}{b_{m,n}^{(j)}} + n^2(D_{\parallel} - D_{\perp}) . \tag{3.11}$$

The $a_{m,n}^{(j)}$, $b_{m,n}^{(j)}$ and $c_{m,n}$ coefficients for all the correlation functions are given numerically as a polynomial in $\langle P_2 \rangle$ and their expansion coefficients are tabulated in Table I of Ref. [6] for a Maier-Saupe potential [7,8].

The SRD model gives [from Eq. (3.2) and (3.7)] the spectral densities of a deuteron due to molecular rotations (MR, as the superscript)

$$J_m^{MR}(m\omega) = \sum_p \left[d_{p0}^2(\theta_{M,Q})\right]^2 \sum_k \frac{(\beta_{m,n}^2)_k \cdot (\alpha_{m,n}^2)_k}{(m\omega)^2 + (\alpha_{m,n}^2)_k^2} , \tag{3.12}$$

where $\theta_{M,Q}$ is the angle between the cylindrical symmetry axis of the molecule and principal component of the spin interaction (e.g. C-D bond).

Asymmetric Molecules in Uniaxial Phases

In a more realistic situation, where the liquid crystal molecule is treated as a biaxial rotor reorienting in a uniaxial potential of mean torque, Tarroni and Zannoni's model [9] has been proposed, in which $U(\Omega)$ is independent of α and may be expanded in terms of Wigner matrices as

$$\frac{U(\beta,\gamma)}{kT} = \sum_{Jq} a_{Jq} D_{0,q}^{J}(\beta,\gamma) \tag{3.13}$$

and the equilibrium probability is

$$P(\beta,\gamma)=\frac{\exp[-U(\beta,\gamma)/k_BT]}{\int d\Omega\exp[-U(\beta,\gamma)/k_BT]}. \tag{3.14}$$

The conditional probability function $P(\Omega_0\,|\,\Omega t)$ can be obtained from diagonalizing the diffusion matrix $(\hat{R}^n)_{L'm',Lm}$ [9] in a basis set of Wigner functions. Here the correlation functions for reorientation can be nonzero for $n\neq n'$, and are given by a sum of infinite number of exponentials:

$$g^2_{mnn'}(t)=\sum_k(\beta^2_{mnn'})_k\exp[(\alpha^2_{mnn'})_k t], \tag{3.15}$$

where the decay constants, $(\alpha^2_{mnn'})_k/D_\perp$, are the eigenvalues of the rotational diffusion matrix, and $(\beta^2_{mnn'})_k$, the corresponding eigenvectors, govern the relative weights of the exponentials. The spectral densities of motion for the unique axis of the interaction tensor making an angle θ with the molecular z axis are obtained by Fourier transforming $G^2_{m_L}(t)$ to give

$$J_{m_L}(m_L\omega)=\sum_{m_M}\sum_{m'_M}d^2_{m_M,0}(\theta)d^2_{m'_M,0}(\theta)\sum_k\frac{(\beta^2_{m_Lm_Mm'_M})_k(\alpha^2_{m_Lm_Mm'_M})_k}{(\alpha^2_{m_Lm_Mm'_M})^2_k+(m_L\omega)^2}. \tag{3.16}$$

The Tarroni and Zannoni model has been applied in a deuterium NMR study of a biaxial solute in nematic phase [10] and to the solvent molecules in smectic liquid crystals [11,12].

Uniaxial Molecules in Biaxial Phases

When a uniaxial molecule is reorienting in biaxial mesophases of D_{2h} symmetry, a model has been proposed by Berggern *et. al*[13,14]. The consequence is the possibility of observing correlation functions with $m_L\neq m'_L$. It is shown that some spectral densities vanish, while others change continuously at the biaxial-uniaxial phase transition. The biaxial spectral densities are those which are nonzero in a biaxial phase and vanish in a

uniaxial phase. Here $U(\Omega)$ is independent of γ and expanded in terms of Wigner matrices as

$$\frac{U(\alpha,\beta)}{kT} = \sum_{Jp} a_{Jp} D^{J}_{p,0}(\alpha,\beta), \tag{3.17}$$

and the equilibrium probability is

$$P(\alpha,\beta) = \frac{\exp[-U(\alpha,\beta)/k_B T]}{\int d\Omega \exp[-U(\alpha,\beta)/k_B T]}. \tag{3.18}$$

The conditional probability function $P(\Omega_0 \mid \Omega t)$ can be obtained from diagonalizing the diffusion matrix $(\hat{R}^n)_{L'm',Lm}$ [13] in a basis set of Wigner functions. The correlation functions for reorientation are given by a sum of infinite number of exponentials:

$$g^2_{mm'n}(t) = \sum_k (\beta^2_{mm'n})_k \exp[(\alpha^2_{mm'n})_k t]. \tag{3.19}$$

By Fourier transforming $g^2_{mm'n}(t)$, taking into account the unique axis of the interaction tensor making an angle θ with the molecular z axis, the spectral densities are

$$J_{m_L m'_L}(\omega) = \sum_{m_M} \left[d^2_{m_M 0}(\theta)\right]^2 \sum_k \frac{(\beta^2_{m_L m'_L m_M})_k \cdot (\alpha^2_{m_L m'_L m_M})_k}{\omega^2 + (\alpha^2_{m_L m'_L m_M})^2_k}. \tag{3.20}$$

3.3 Superimposed Rotations Model

Apart from the overall motion of molecules discussed in the previous section, internal dynamics of flexible mesogens are now described. One basic internal rotation model, rotational isomeric state model (RIS) [15], applies to rotational jumps among the three equilibrium sites when the potential barriers are larger than $k_B T$. This is due to the fact that rotation about each carbon-carbon (C-C) bond in the chain is assumed to take one of

the three dihedral angles (ϕ=0º, ±112º). These correspond to the *trans* (*t*) and two symmetric *gauche* ($g^{\pm}$) linkages. The *gauche* states have higher energy in comparison to that of the *trans* by an amount of E_{tg}. Since our samples are not fully deuterated on the chain, not enough information is available to solve the full chain dynamics. The RIS model cannot be used to generate all possible chain conformations.

The other model involving a stochastic rotational diffusion about a bond is discussed in more details here. It is found that the deuteron spin-lattice relaxation rates $R^{(j)}$, where *j* labels the position of the deuteron in the alkyl chains, decrease monotonically along the chains of mesogens. Beckmann *et. al* [16] have proposed a model of superimposed rotations which is consistent with a monotonic decrease of relaxation rates along the pentyl chain of 5CB-d_{15}. Here we apply this model to internal ring flips in our sample 8BEF5 (Fig. 3.1).

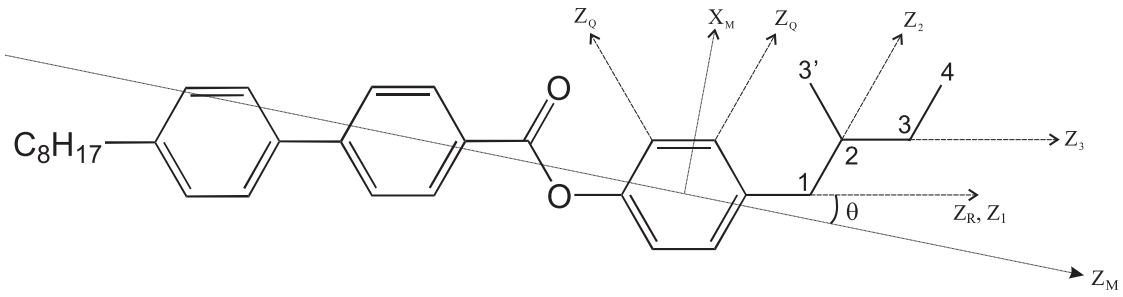

Fig. 3.1 Sketch of 8BEF5, the location of the molecular frame and internal rotation axes. The Y_M axis is chosen to complete a right-handed Cartesian coordinate system.

In this model, the molecule is taken to be made of a number of rigid sub-units, labeled as in figure above. *R* is for the aromatic ring containing deuterons and *i*=1 to 4 for the CD_2 and CD_3 groups. The structure and the location of internal rotation axes are as shown. Since the C-C_1 bond between the aromatic ring and carbon 1 (C_1) are supposed to be rigid,

z_R and z_1 are parallel to one another. An angle θ is defined between the z_M molecular axis and the *para* axis, along which z_R and z_1 now lie. The internal rotation axis linking fragments *i* and *i*+1 is used to define *z* axis for the *i*th sub-unit while its *y* axis is taken to be orthogonal to z_i and z_{i+1}. With this definition the Euler angle $\alpha_{i,i+1}$ linking fragments *i* and *i*+1 is zero, and the Euler angle $\beta_{i,i+1}$ is time-independent and thus leaving only the Euler angle $\gamma_{i,i+1}$ which contains the time dependence of internal motion. The PAS for quadrupolar tensor of a particular deuteron is denoted by Q; to a good approximation this tensor is cylindrically symmetric and the symmetry axis is labeled z_Q.

Again, we start with the correlation function,

$$G_{m_L}(t) = \left\langle F^{(2,m_L)}(0) F^{(2,m_L)*}(t) \right\rangle, \tag{3.21}$$

where $F^{(2,m_L)}$ is the m_L th component of the irreducible spherical tensor representing the quadrupolar interaction; it is expressed in the laboratory frame (*L*) with the z axis parallel to the magnetic field. Now the molecular frame is assumed to be the principal frame for the quadrupolar tensor. In transforming into a molecular frame (*M*) in which the components $F^{(2,m_M)}$ are time-independent,

$$F^{(2,m_L)}(t) = \sum_{m_M} D^2_{m_M m_L}[\Omega_{LM}(t)] F^{(2,m_M)}, \tag{3.22}$$

and substituting Eq. (3.22) into Eq. (3.21), we have

$$G_{m_L}(t) = \sum_{m_M}\sum_{m'_M} F^{(2,m_M)} F^{(2,m'_M)*} \left\langle D^2_{m_M m_L}[\Omega_{LM}(0)] D^2_{m_M m_L}[\Omega_{LM}(t)] \right\rangle. \tag{3.23}$$

Apply this treatment to 8BEF5, and take the ring deuterons of 8BEF5, three coordinate transformations have to be considered: First the quadrupolar frame (Q_R) to the segmental

frame fixed on the *para* axis of the phenyl ring, and this requires the Euler angles Ω_{RQ_R}. From here we transform to the molecular frame involving Euler angles Ω_{MR}, and then to the laboratory frame with the Euler angles Ω_{LM}. Thus,

$$F^{(2,m_L)}(t) = \sum_{m_M}\sum_{m_R}\sum_{m_Q} D^2_{m_M m_L}(\Omega_{LM}) D^2_{m_R m_M}(\Omega_{MR}) D^2_{m_R m_{QR}}(\Omega_{RQ_R}) F^{(2,m_Q)}_{Q_R} . \qquad (3.24)$$

The subscript on $F^{(2,m_Q)}_{Q_R}$ is to emphasize that these tensor components are, in principle, site dependent. Following the same substitution in Eq. (3.23),

$$G^{(R)}_{m_L}(t) = (F^{(2,0)}_{Q_R})^2 \sum_{m_M}\sum_{m'_M}\sum_{m_R}\sum_{m'_R} D^2_{0m_R}(\Omega_{RQ_R}) D^2_{0m'_R}(\Omega_{RQ_R})$$
$$\times \left\langle D^2_{m_M m_L}[\Omega_{LM}(0)] D^{2*}_{m'_M m_L}[\Omega_{LM}(t)] D^2_{m_M m_R}[\Omega_{MR}(0)] D^{2*}_{m'_M m_R}[\Omega_{M'R}(t)] \right\rangle , \qquad (3.25)$$

where the superscript (R) in $G^{(R)}_{m_L}(t)$ is to label the correlation function for the deuterons on the phenyl ring.

Two drastic approximations are necessary in order to simplify this complex correlation function to the point where its evaluation is practical [16]. First, the internal and external modes of motions are decoupled from one another. Thus the time-averaged factor in the correlation function is separated into two parts to be evaluated. The first of these is for reorientation of the molecular reference frame in the laboratory frame, and this part of the correlation function is given by

$$\left\langle D^2_{m_M m_L}[\Omega_{LM}(0)] D^{2*}_{m'_M m_L}[\Omega_{LM}(t)] \right\rangle = \left\langle | D^2_{m_M m_L} |^2 \right\rangle g^{(m_M)}_M(t) \delta_{m_M m'_M} , \qquad (3.26)$$

where now we have introduced the second assumption that the correlation function can be written in terms of a time independent and time dependent term. The latter is a reduced correlation function $g^{(m_M)}_M(t)$ and is taken to be independent of m_L. This assumption is consistent with the strong collision model [5]. The above delta function arises from the

assumed cylindrical symmetry of rotational motion about a fixed axis thereby leading to equality for terms with $\pm m_M$.

The second part in the correlation function is for the internal rotation, and can be rigorously separated into time independent and time dependent parts:

$$\left\langle D^2_{m_R m_M}[\Omega_{MR}(0)] D^{2*}_{m'_R m_M}[\Omega_{MR}(t)] \right\rangle = d^2_{m_R m_M}(\beta_{MR}) d^2_{m'_R m_M}(\beta_{MR}) \times \left\langle \exp[-i[m'_R \gamma_{MR}(t) - m_R \gamma_{MR}(0)] \right\rangle \quad (3.27)$$

When $m_R = 0$, this correlation becomes constant and independent of internal rotation about the C_{Ring}-C_1 bond (*para* axis). Thus,

$$\left\langle D^2_{m_R m_M}[\Omega_{MR}(0)] D^{2*}_{m'_R m_M}[\Omega_{MR}(t)] \right\rangle = [d^2_{m_R m_M}(\beta_{MR})]^2 \times \{g_R(t) - [g_R(t) - 1]\delta_{0 m_R}\} \delta_{m_R m'_R}, \quad (3.28)$$

where $g_R(t)$ is

$$g_R(t) = \left\langle \exp\{-i m_R [\gamma_{MR}(t) - \gamma_{MR}(0)] \right\rangle . \quad (3.29)$$

The subscript *R* indicates that the reduced correlation function is for rotations about the *para* axis. Finally, the correlation function describing the molecular reorientation and internal ring motion gives,

$$G^{(R)}_{m_L}(t) = (F^{(2,0)}_{Q_1})^2 \sum_{m_M} \sum_{m_R} \overline{| D^2_{m_M m_L} |^2} g^{(m_M)}_M(t) [d^2_{m_R m_M}(\beta_{MR})]^2 \times \{g_R(t) - [g_R(t) - 1]\delta_{0 m_R}\} \times [d^2_{0 m_R}(\beta_{RQ_R})]^2 . \quad (3.30)$$

A similar expression can be obtained for the first methylene group rotating about the C_{Ring}-C_1 bond. By including a geometric factor $[d^2_{m_i m_i - 1}(\beta_{i-1,i})]^2$ and another term involving internal correlation function $\{g_i(t) - [g_i(t) - 1]\delta_{m_i 0}\}$, we can generalize the correlation function for additional sub-units. For example, for the deuteron on the second

rigid methylene group $G_{m_L}^{(2)}(t)$,

$$G_{m_L}^{(2)}(t) = (F_{Q_2}^{(2,0)})^2 \sum_{m_M} \sum_{m_1} \sum_{m_2} \overline{|D_{m_M m_L}^2|^2} g_M^{(m_M)}(t)[d_{m_R m_M}^2(\beta_{M1})]^2 [d_{m_1 m_M}^2(\beta_{12})]^2$$
$$\times \{g_1(t) - [g_1(t) - 1]\delta_{0m_1}\} \{g_2(t) - [g_2(t) - 1]\delta_{0m_2}\} \times [d_{0m_2}^2(\beta_{2Q_2})]^2 . \quad (3.31)$$

For simplicity, apply the Fourier transform to Eq. (3.30)

$$J_{m_L}^{(i)}(m_L\omega_0) = \int_0^\infty G_{m_L}^{(i)}(t)\cos(m_L\omega_0 t)dt . \quad (3.32)$$

Now the spectral densities for the deuteron on C_1 site (or for the ring deuterons by interchanging labels 1 and *R*) can be written as

$$J_{m_L}^{(1)}(m_L\omega_0) = (F_{Q_2}^{(2,0)})^2 \sum_{m_M=-2}^{2} \sum_{m_1=-2}^{2} [\overline{|D_{m_M m_L}^2|^2}(d_{m_1 m_M}^2(\beta_{M1}))^2 (d_{0m_1}^2(\beta_{1Q_1}))^2$$
$$\times \int_0^\infty g_M^{(m_M)}(t)\{g_1(t) - [g_1(t) - 1]\delta_{0m_1}\}\cos(m_L\omega_0 t)]dt . \quad (3.33)$$

For the term with $m_1 = 0$ in Eq. (3.33), in the fast motion limit,

$$\int_0^\infty g_M^{(m_M)}(t)\cos\omega t dt = \int_0^\infty g_M^{(m_M)}(t)dt$$
$$= \tau_M^{(m_M)} . \quad (3.34)$$

For the products of correlation function in Eq. (3.33), when $m_1 \neq 0$ in the fast motion limit

$$\int_0^\infty g_M^{(m_M)}(t)g_1(t)dt = \{[\tau_M^{(m_M)}]^{-1} + \tau_1^{-1}\}^{-1} . \quad (3.35)$$

Finally, combining the small step diffusion rotation model, the superimposed rotation model with strong collision limit, we arrive at the expression of the spectral densities

$$J_m(m\omega, 0°) = \frac{3\pi^2}{2}(q_{CD}^i)^2 \sum_n \sum_p [d_{p,0}^2(\beta_{R,Q}^i)]^2 [d_{n,p}^2(\theta_{MR})]^2$$
$$\times \sum_k \frac{(\beta_{m,n}^2)_k \left[(\alpha_{mn}^2)_k + (1 - \delta_{p,0})D'\right]}{(m\omega)^2 + \left[(\alpha_{mn}^2)_k + (1 - \delta_{p,0})D'\right]^2} , \quad (3.36)$$

where D' is $1/\tau_1$ in the above equations, *i* = ring or CH_2 group. θ_{MR} is the angle

between the long molecular axis and the *para* axis. This equation is applied in the deuterium study of chiral smectigen 8BEF5 discussed in Chapter 4. Similarly, the spectral densities for the nitrogen and deuteron NMR study of a lyotropic sample DACl/H_2O will be included in Chapter 5.

Since nitrogen 14 nuclei has also a spin $I = 1$ system and governed by the quadrupole interaction, we can treat ^{14}N relaxation as we did in ^2H study. Thus, for the nitrogen on the head group N-C_1 bond, the spectral densities labeled by a superscript N

$$J_m^N(m\omega,0°) = \frac{3\pi^2}{2}(q_{Nitrogen})^2 \sum_n [d_{n,0}^2(\theta_{NC})]^2 \times \sum_k \frac{(\beta_{mn}^2)_k (\alpha_{mn}^2)_k}{(m\omega)^2 + (\alpha_{mn}^2)_k^2}, \tag{3.37}$$

where $q_{nitrogen}$ is the quadrupolar coupling constant for nitrogen, and θ_{NC} is the angle between the N-C_1 bond and the long molecular axis. For the deuteron $^2H_{C1}$ on the chain C_1 site of DACl,

$$J_m^{^2H_{C_1}}(m\omega,0°) = \frac{3\pi^2}{2}(q_{CD})^2 \sum_n \sum_p [d_{p,0}^2(\beta_{NCH})]^2 [d_{n,p}^2(\theta_{NC})]^2 \times \sum_k \frac{(\beta_{m,n}^2)_k \left[(\alpha_{mn}^2)_k + (1-\delta_{p,0})D'\right]}{(m\omega)^2 + \left[(\alpha_{mn}^2)_k + (1-\delta_{p,0})D'\right]^2}, \tag{3.38}$$

where the diffusion coefficient D' corresponding the correlation time τ_1 in Eq. (3.35) is included for the superimposed internal rotation. The q_{CD} stands for the quadrupolar coupling constant for deuteron on the C-D bond. And β_{NCH} is the angle ∠N-C_1-H. For the deuteron $^2H_{C2}$ on the chain C_2 site,

$$J_m^{^2H_{C_2}}(m\omega,0°)=\frac{3\pi^2}{2}(q_{CD})^2\sum_n\sum_j\sum_p[d^2_{p,0}(\beta_{CCH})]^2[d^2_{j,p}(\gamma_{NCC})]^2[d^2_{n,j}(\theta_{NC})]^2$$

$$\times\sum_k\frac{(\beta^2_{mn})_k\left[(\alpha^2_{mn})_k+(1-\delta_{j,0})D'+(1-\delta_{p,0})D''\right]}{(m\omega)^2+\left[(\alpha^2_{mn})_k+(1-\delta_{j,0})D'+(1-\delta_{p,0})D''\right]^2}, \qquad (3.39)$$

where D'' is the diffusion coefficient for deuterons rotating about the C_1-C_2 bond. $d^2_{j,p}(\gamma_{NCC})$ denotes the Wigner matrix whose C_1-C_2 segment is rotating about the N-C_1 bond. β_{CCH} is the angle $\angle C_1$-C_2-H.

3.4 Angular-Dependent Relaxation

In liquid crystals, it is customary to write the irreducible spectral densities given in the laboratory frame in terms of spectral densities expressed in the crystal-frame, which is defined by the symmetry axis (director) of the phase. In the case of the director not aligned along the external magnetic field, the extra transformation involves Euler angles $\Omega_{LD}[\equiv(\phi_{LD},\theta_{LD})]$ from the crystal frame to the laboratory frame. This produces linear combination of the crystal frame spectral densities according to [13,17,18]. If the assumption of letting ϕ_{LD} distinguishable in our SmC* study in the next chapter, one obtains in biaxial liquid crystalline phases [17]

$$J_1(\omega,\theta)=\frac{3}{2}(\cos^2\theta\sin^2\theta)J_{0,0}(\omega,0^0)+\frac{1}{2}\left(1-3\cos^2\theta+4\cos^4\theta\right)J_{1,1}(\omega,0^0)$$
$$+\frac{1}{2}\left(1-\cos^4\theta\right)J_{2,2}(\omega,0^0)-\sqrt{6}(\cos^2\theta\sin^2\theta)J_{2,0}(\omega,0^0)$$
$$-\frac{1}{2}\left(1-5\cos^2\theta+4\cos^4\theta\right)J_{1,-1}(\omega,0^0)-\frac{1}{2}\left(1-\cos^2\theta\right)^2J_{2,-2}(\omega,0^0)$$
$$J_2(2\omega,\theta)=\frac{3}{8}(1-\cos^2\theta)^2J_{0,0}(2\omega,0^0)+\frac{1}{2}(1-\cos^4\theta)J_{1,1}(2\omega,0^0)$$

$$+\frac{1}{8}\left(1+6\cos^2\theta+\cos^4\theta\right)J_{2,2}(2\omega,0^0)+\frac{\sqrt{6}}{4}\left(1-\cos^4\theta\right)J_{2,0}(2\omega,0^0)$$

$$+\frac{1}{2}\left(1-2\cos^2\theta\right)^2 J_{1,-1}(2\omega,0^0)+\frac{1}{8}\left(1-\cos^2\theta\right)^2 J_{2,-2}(2\omega,0^0), \qquad (3.40)$$

where uniaxial spectral densities ($m=m'$) are $J_{0,0}$, $J_{1,1}$, and $J_{2,2}$, and biaxial spectral densities $J_{2,0}$, $J_{1,-1}$ and $J_{2,-2}$ are only nonzero in biaxial phases. Note that $J_{i,i} \equiv J_i(\omega)$. Even in biaxial mesophases, the biaixial spectral densities are unobservable if the director is aligned with the external field as in some SmC phases. Biaxial spectral densities due to molecular reorientations in biaxial phases are only calculated theoretically based on the small step rotational diffusion model [13,14], but no experiments have been reported on the determination of biaxial spectral densities so far.

References

1 J.P.Tollenaere and E.E.Moret (1997). Guidebook on Molecular Modelling in Drug Design: Hyper-Glossary of Terminology. Retrieved May 22, 2005, from Department of Medicinal Chemistry, Faculty of Pharmacy, Utrecht University, Netherlands. Web Site:http://wwwcmc.pharm.uu.nl/webcmc/glossary.html

2 R.R.Vold,"Nuclear Spin Relaxation" in *Nuclear Magnetic Resonance of Liquid Crystals*, edited by J.W.Emsley (Reidel, Dordrecht, 1985), Vol. 141, pp. 253.

3 P.L.Nordio and P.Busolin, J. Chem. Phys. **55**, 5485 (1971).

4 P.L.Nordio, G.Rigatti, and U.Segre, J. Chem. Phys. **76**, 253 (1972).

5 P.L.Nordio and U.Segre, *The Molecular Physics of Liquid Crystals*. (Academic

Press, New York, 1979).

[6] R.R.Vold and R.L.Vold, J. Chem. Phys. **88**, 1443 (1988).

[7] W.Maier and A.Saupe, Nature **14a**, 882 (1959).

[8] W.Maier and A.Saupe, Nature **15a**, 287 (1960).

[9] R.Tarroni and C.Zannoni, J. Chem. Phys. **95**, 4550 (1991).

[10] S.Huo and R.R.Vold, J. Phys. Chem. **99**, 12391 (1995).

[11] R.Y.Dong and X.Shen, J. Chem. Phys. **105**, 2107 (1996).

[12] R.Y.Dong, J. Phys. Chem. **100**, 15663 (1996).

[13] E.Berggren, R.Zannoni, and C. Zannoni, J. Chem. Phys. **99**, 6180 (1993).

[14] E.Berggren and C.Zannoni, Mol. Phys. **85**, 299 (1995).

[15] P.J.Flory, *Statistical Mechanics of Chain Molecules*. (Interscience, New York, 1969).

[16] P.A.Beckmann, J.W.Emsley, G.R.Luckhurst, and D.L.Turner, Mol. Phys. **59**, 97 (1986).

[17] R.Y.Dong, Liq. Cryst. **16**, 1101 (1994).

[18] S.Gustafsson and B.Halle, Mol. Phys. **80**, 549 (1993).

4 Chiral Smectgon 8BEF5 in the SmA and SmC* Phases

4.1 Introduction

One of most fascinating properties of liquid crystals is their diverse molecular behaviour in various mesophases due to even minor structural changes. Although thorough studies of mesogens at high temperature unaxial phases, such as Nematic and Smectic A phases, are well documented [1-7], efforts are still necessary to understand the structure and polar properties of chiral smectogens which may exhibit ferroelectric [8], antiferroelectric [9] and related subphases.

^{13}C NMR studies have proven useful to understand the molecular structure via studying of orientational order and dynamics near the SmA-SmC* transition [10-14]. For example, information of the angle between the bent chiral chain and long molecular axis of some ferroelectric liquid crystal can be obtained [14,15]. On the other hand, deuterium NMR study is a powerful tool used extensively for extracting dynamical information [1]. However, the characterization of dynamic behaviour of these biaxial smectogens is not easily accessible. The problems, in particular the relation between tilted molecules in different smectic planes and the chiral pitch axis, are due to the difficulty of extracting meaningful spectral parameters from experimental observations and the lack of a suitable theoretical motional model (of the SmC* phase) which involves incredible number of parameters. Two chiral smectogens 10B1M7 [16,17] and 8BEF5 [18,19] have been studied in

our lab using ^{2}H NMR but with limited success.

Recently, Domenici *et. al* [20] proposed a new approach to tackle the problem in SmC* phase by treating aromatic deuterons of 8BEF5 at a single Larmor frequency. In this chapter, we present the experimental spectral data for the aromatic and alpha deuterons on the chiral chain at a higher Larmor frequency, and the analysis of deuteron results from two frequencies, 46 and 61.4 MHz, which can provide more reliable information to further test this approach [21]. The limiting assumption such as Perrin model [22] used before has been removed. Comparison of derived motional parameters among SmA phase and SmC* phase will be discussed.

4.2 Quadrupolar Splitting and Ordering

A typical deuterium NMR spectrum in a more ordered smectic phase, shown in Fig. 4.1 at 352 K, gives separate quadrupolar doublets, similar to those reported earlier [18]. The overlap among the aromatic peaks ‘a’ and ‘b’ were similar in both SmA and SmC* phase. This overlap only exacerbated when entering other smectic phases below 340 K. The spectral densities derived for the region of overlapped aromatic peaks at SmC* phase were improved by deconvolution [23,24] using Bruker NMR software.

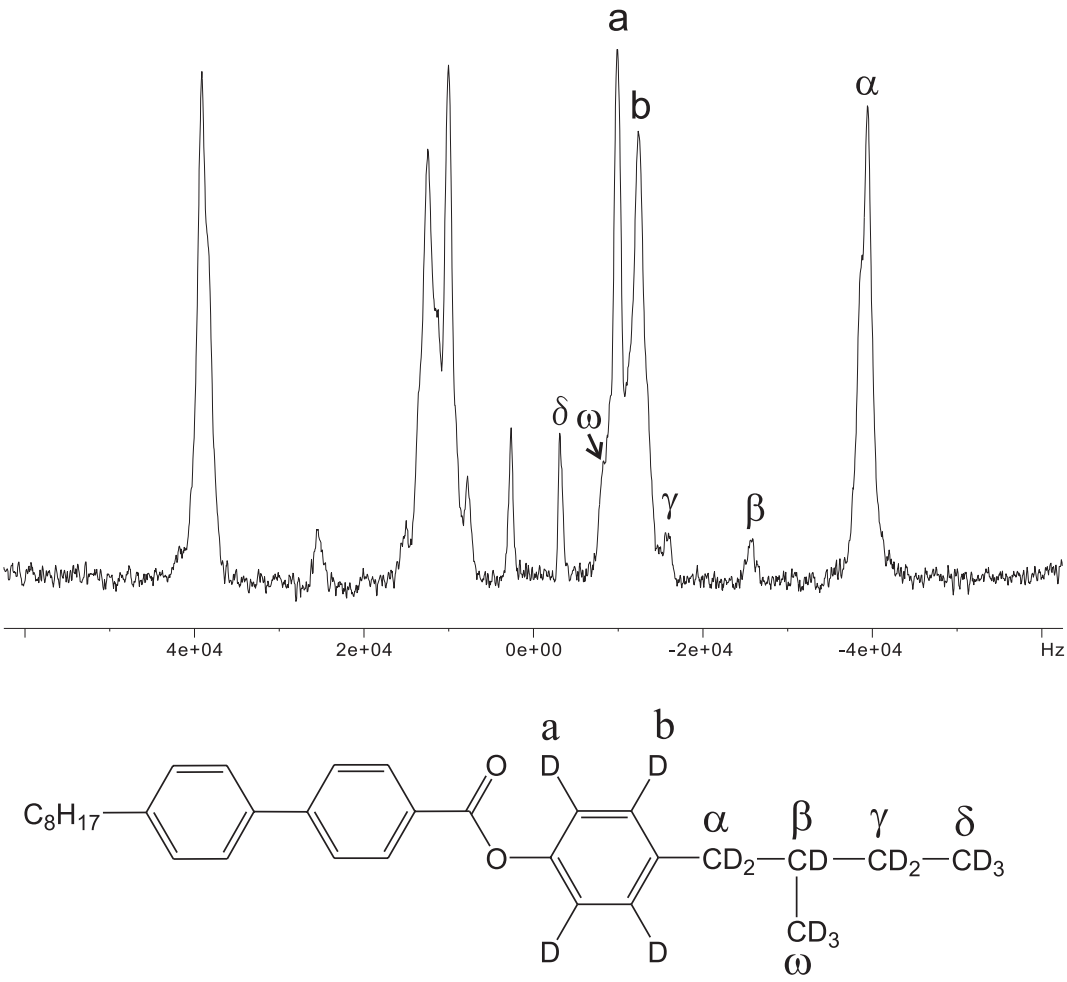

I 408K **BPIII** 407K **N*** 406K **SmA** 348K **SmC*** 335K **(SmI* SmJ*)** 315K **SmG*** 319 **Cr**

Fig. 4.1 Plot of a typical deuterium spectrum (352 K) and molecular structure of (S)-[4-(2-methylbutyl)phenyl]-4'-octylbiphenyl carboxylate and its phase sequence.

Despite the ability of NMR to detect the transition temperature between mesophases, optical methods of texture observation, such as polarizing microscopy, can determine the mesophase transitions of liquid crystals more accurately. This is due to a tiny homogenized sample under study. NMR samples usually require much greater mass (volume), and as a consequence a temperature gradient across the sample exists. Since there is always a temperature variance inside the NMR probe for each experiment, and

the thermocouple is only located close to the NMR sample but not inside the sample, the set temperature of the temperature control unit does not reflect the real temperature of the sample accurately. A means of calibration of temperature must be employed to make experiments on the same sample consistent. In our case, quadrupolar splittings of different deuterium nuclei as a function of temperature (Fig. 4.2) were used to calibrate the 'real temperature' of the sample [18]. The peak assignments in Fig. 4.2 show increasing motional flexibility towards the end of the chain, while the deuterons on the aromatic sites are more motionally averaged because of the ring flip. Quite a portion of splitting data of deuterons on site 'ω' and site 'γ' were missing, because these sites happened to be overlapped by those from the aromatic deuterons and also they have lower deuteration. In the SmA phase, the splittings increase smoothly upon decreasing temperature (reported every 5 degrees). Experiments were done more frequently, every 1 or 2 degrees, to record quadrupolar splittings in chiral mesophases within a small range of low temperatures. At 75 ºC, SmA-SmC* transition was observed as a change in slope consistent with the previous paper [18]. The SmC* phase terminates with a sharp increase at the onset of SmI* phases at around 62 ºC. If omitting the data of SmC* phase, we can see a smooth connection between SmA and SmI* for most sites. The SmC* data may be explained by the occurrence of tilt angle θ between director and the normal of smectic plane.

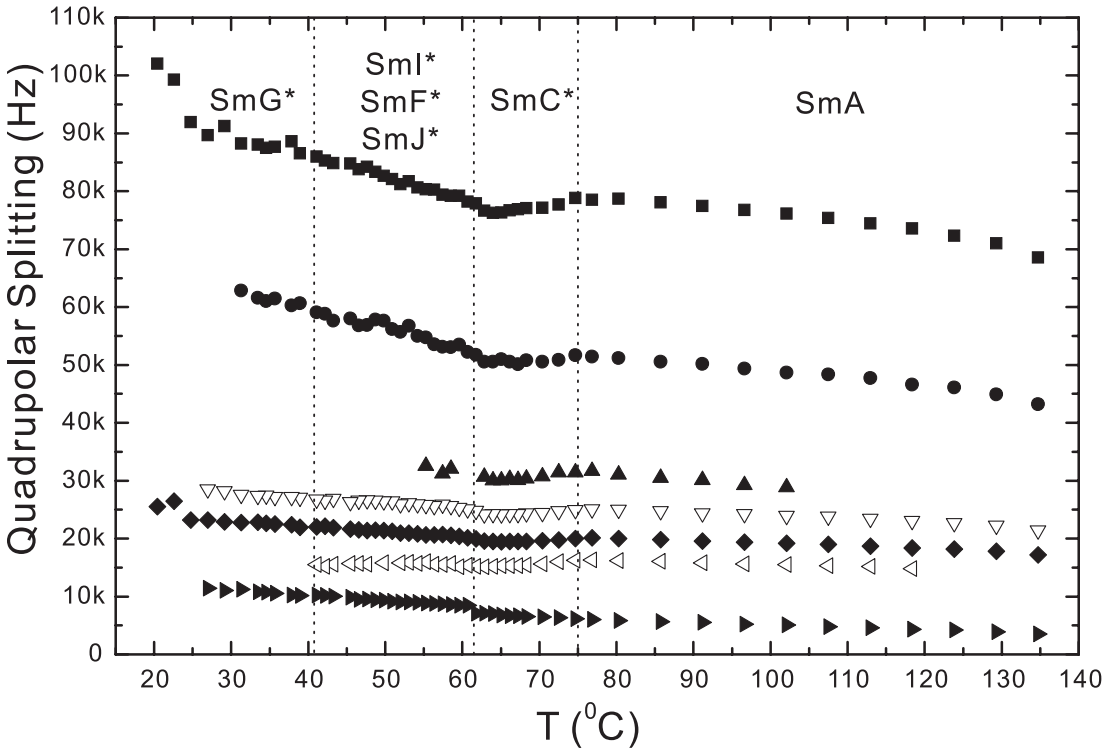

Fig. 4.2 Quadrupolar splittings measured for the different deuterium nuclei in the various mesophases as a function of temperature. The legend from the top to bottom, square, circle, up closed triangle, down open triangle, tilted square, left open triangle, right closed triangle refer to sites 'α', 'β', 'γ', 'b', 'a', 'ω' and 'δ', respectively.

The quadrupolar splittings of sites a and b can also be used to obtain the order parameter S_{zz}, by means of Eq. (1.38), where i denotes the deuteron site, and $\beta^i_{R,Q}$ is the angle between the *para* axis and the i site C-D bond. The angle $\beta^i_{R,Q}$ are 59.3º for i = 'a' deuterons (next to the COO group), 60.3º for the 'b' deuterons (next to the chiral chain) and 107.5º for the 'α' methylene deuterons, quadrupolar coupling constant q^i_{CD} = 185 kHz for aromatic deuterons 'a' or 'b', q^α_{CD} = 165 kHz for the carbon site α, and for the aromatic sites, an asymmetry parameter η = 0.04 is used. The very small best-fitting parameter $\Delta_{biaxial}$ indicates a low molecular biaxiality in SmC* phase. The experimental values of order parameter S^{exp}_{zz} have been described in the following equation to relate

the calculated values S_{zz}^{cal} , which are obtained by extrapolating from the SmA phase, ranging between 0.86 to 0.9, and the tilt angle θ in the SmC* phase,

$$S_{zz}^{\exp} = S_{zz}^{cal} \frac{3\cos^2\theta - 1}{2} . \tag{4.1}$$

The tilt θ is found to vary from 0º to 11º upon decreasing temperature in the SmC* phase.

4.3 Results and Discussion

^{2}H T_{1Z} and T_{1Q} in the SmC* phase give spectral densities $J_m(m\omega_0,\theta^o)$ since the director is oriented at the tilt angle θ with respect to the external magnetic field. Eqs. (3.40) are used to relate them to the calculated spectral densities for the director parallel to the magnetic field. To describe the spectral densities, there are several motional models to treat the overall molecular rotation, such as Nordio's model, Vold and Vold's model and third rate model [25,26]; and to account for the internal motion such as superimposed rotations, models like strong collision limit and small step limit. In the present study, we are using small step rotation diffusion [27,28] to describe the molecular reorientation, plus superimposing internal bond (ring) rotation treated in the strong collision limit [29]. Collective order director fluctuation (see Appendix B) [1] is deemed to be negligible based on previous studies [19,20]. Tarroni and Zannoni [28] solved the rotational diffusion equation, yielding the decay constants $(\alpha^2_{m_L m_M})_k / D_\perp$, which are the eigenvalues of the rotational diffusion matrix, and $(\beta^2_{m_L m_M})_k$, the corresponding eigenvectors, which govern the relative weights of the exponentials. The diffusional coefficient $D_\perp$ represents tumbling

rotation of the molecule about one of the short molecular axes, while $D_{\|}$ the spinning motion about the long molecular axis. Both of $D_{\perp}$ and $D_{\|}$ appear in $(\alpha_{mn}^2)_k$. The spectral densities for the aromatic ($D' = D_R$) and methylenic ($D' = D_\alpha$) deuterons in the phenyl ring and at the C_α site are given by Eq. (3.36) in Chapter 3, where D' is the internal rotation diffusion constant of the ring or the methylenic group about the *para* axis, and the angle between the *para* axis and the long molecular axis $\theta_{MR} = 8°$ [18]. The term $(1-\delta_{p,0})$ in Eq. (3.36) denotes the choice of strong collision limit. The order parameter S_{zz} extrapolated from the SmA phase and the tilt angle (see Table 4.1) in the SmC* phase are those determined previously [18]. The S_{zz} is required to construct the anisotropic potential of mean torque for solving the rotational diffusion equation.

Table 4.1 Tilt angle and extrapolated S_{zz} in the SmC* phase used in Eqs. (3.40).

Temperature (ºC)	Tilt Angle (º)	Order Parameter S_{zz}
75	0	0.86
73	4.6	0.87
71	8.0	0.87
69	9.4	0.87
67	10.4	0.88
65	10.8	0.88
63	10.9	0.89
62	11.0	0.89

The SmC* phase was difficult to tackle before [30] due its phase biaxiality. In the helicoidal structure, the local director describes the molecular tilt with a fixed angle θ from the normal to the smectic planes, while the value of azimuthal angle ϕ varies from 0º to 360º according to different smectic planes in which the molecule are located. Fig. 4.3 shows a general situation where the pitch axis of a molecule in SmC* phase tilts an

angle Θ from the external field direction, z axis.

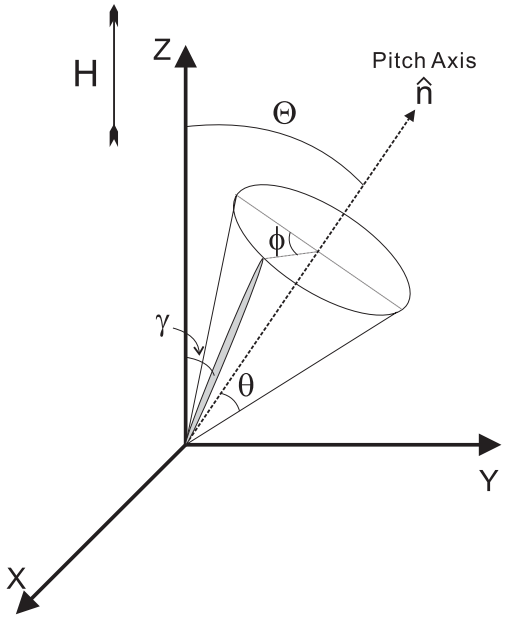

Fig. 4.3 Geometric diagram of a molecule in SmC* phase in a general situation. The grey bar is the molecule. Here the pitch axis lies on the layer normal. The tilt angle θ from the pitch axis, the azimuthal angle ϕ, the angle Θ between the pitch axis and the z axis, and the angle γ between the molecule and the z axis are shown as above.

Since the quadrupolar splitting is related to $\cos\gamma$, $\Delta\nu \propto P_2(\cos\gamma) = \frac{3}{2}\cos^2\gamma - \frac{1}{2}$, and there is a trigonometric relation between these angles

$$\cos\gamma = \cos\theta\cos\Theta + \sin\theta\sin\Theta\cos\phi\,. \tag{4.2}$$

When the sample is aligned, the pitch axis, and the plane normal are along the external magnetic field. So the angle Θ = 0. This makes the term involving the azimuthal angle ϕ trivial, and there is no ϕ dependence for the $\Delta\nu$. Besides, it is classically understandable that the variety of azimuthal angle ϕ on different smectic planes contribute mutually cancelling effects, yielding the same quadrupolar splitting as in a macroscopically uniaxial phase. There is no experimental evidence of ϕ dependence in spin relaxation rates, leading to the assumption of ignoring ϕ (set ϕ = 0º) [20] and the treatment of the

biaxial SmC* phase as an uniaxial environment. Hence, the spectral densities at the tilt angle θ can be associated to the spectral densities $J_{m,m'}(\omega,0^o)$, where the subscripts m and m′ are projection indices in the laboratory frame. According to Eqs. (3.40), only uniaxial spectral densities (m=m′) J_{00}, J_{11}, and J_{22} are used in the present study, while biaxial spectral densities $J_{2,0}$, $J_{1,-1}$ and $J_{2,-2}$ disappear. Indeed, the biaxial spectral densities have been difficult to detect or measure experimentally. Since the studied SmC* phase has relatively small tilt angle, it is justified to discard the small biaxial spectral densities. The spectral densities of the 'a' and 'b' deuterons in the SmC* phase at 46 MHz [20] seem to support such an assumption.

The spectral densities for aromatic deuterons 'a' and 'b', and chiral chain site C_α at 61.4 MHz as a function of temperature in the SmA and SmC* phases are plotted in Fig. 4.4a, while their corresponding spectral densities [18] at 46 MHz are reproduced in Fig. 4.4b. The unavailability of C_α data at 46 MHz was caused by the poor signals in the SmC* phase. The spectral densities measured at 61.4 MHz show continuous behaviours across the SmA-SmC* transition just like those reported at 46 MHz. This continuity is in fact expected even if the biaxial terms are included, because the tilt angle θ at SmC* phase drops gradually to 0º at the onset of the SmA phase. Eq. (3.36) is employed for SmA phase, while in addition Eqs. (3.40) without biaxial contribution is used for SmC* phase.

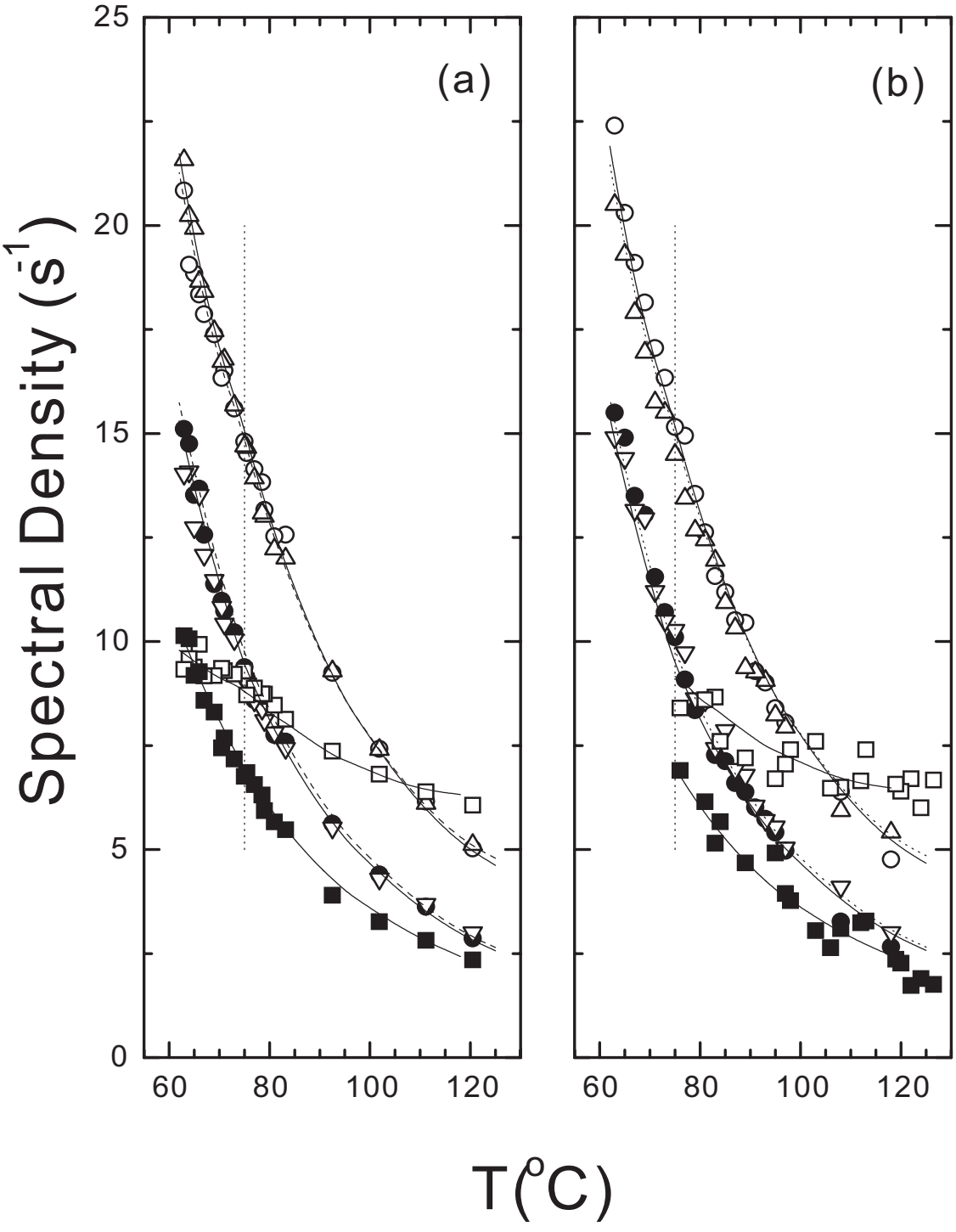

Fig. 4.4 Plot of spectral densities of aromatic ('a' site, circles, open symbol for J_1 and closed symbol for J_2; 'b' site, up triangles for $J_1$and down triangles for J_2) and c_α (squares, open symbol for J_1 and closed symbol for J_2) deuterons in the SmA and SmC* phases of 8BEF5 at 61.4 (a) and 46 (b) MHz. Vertical dash denotes SmA-SmC* transition.

Assuming the diffusional coefficients D_i obey an Arrhenius behaviour ($D_i = D_i^{\infty} \exp[-E_a^i / RT]$, the label *i* specifying the type of motion) within a smectic phase, the 'global target' approach is used to analyze the smoothed spectral densities data in these phases. Instead of using D_i^{∞} as fitting parameters, the above relation is rewritten in terms of D_{iT} at a particular chosen temperature T_s. The D_{iT} can be obtained by an 'individual target' analysis, which is a more usual starting approach when we try to find a rough set of parameters that are needed for the global target approach. By combining our data of 6 spectral densities at 16 temperatures and two frequencies, we have 192 data in total to determine 8 target parameters. All diffusion constants are now varied independently, which was not possible in the previous study [20] due to the lack of experimental data. T_s=391K was used in the SmA phase, and the fitting were optimized by minimizing the sum square error (*F*) using a program called AMOEBA[31].

$$F = \sum_k \sum_{\omega} \sum_i \sum_m [J_m^{(i)Cal}(m\omega) - J_m^{(i)Exp}(m\omega)]_k^2 , \tag{4.3}$$

where the sum over *k* is for 16 temperatures, the sum over *i* covers sites 'a', 'b' and 'α', the sum over ω is for two frequencies and *m*=1 and 2. The fitting quality factor *Q* is given by the percentage of mean-squared deviation,

$$Q = 100F / \sum_k \sum_{\omega} \sum_i \sum_m [J_m^{(i)Exp}(m\omega)]_k^2 \tag{4.4}$$

In fitting the SmC* data, D_{iT} at T_s=348K (tilt angle=0º) were fixed at their best values found in the SmA phase analysis, and only the four activation energies were varied to minimize *F*. Calculated spectral densities from our global analyses at 46 MHz and 61.4

MHz are shown as curves (solid lines for 'a' site and C_α deuterons, while dashed lines for 'b' site deuterons) in Fig. 4.4. As seen in this diagram, the fits to the experimental results are quite good. As a consequence, the derived motional parameters D_i, shown in Fig. 4.5, should be quite reliable. The error limits are estimated by keeping all parameters fixed at their optimized values except the one for which the error limits are seek. The target parameter is changed gradually such that the *F* value is approximately doubled to give the error bounds. As usually found in low molecular mass liquid crystals, the activation energy of the tumbling motion is slightly less than that of the spinning motion [1]. The fitting result plus error limits are presented in Table 4.2.

Table 4.2 Fitting parameters of diffusional coefficients and activation energies with error limits.

		SmA phase	SmC* phase
Pre-exponential Factor	$D_{\parallel}^{\infty}$	$(6.10\pm1.10)\times10^{13}\ s^{-1}$	$(6.02\pm1.30)\times10^{16}\ s^{-1}$
	$D_{\perp}^{\infty}$	$(1.97\pm0.23)\times10^{11}\ s^{-1}$	$(8.82\pm3.68)\times10^{12}\ s^{-1}$
	D_{R}^{∞}	$(4.39\pm0.19)\times10^{14}\ s^{-1}$	$(2.10\pm0.10)\times10^{14}\ s^{-1}$
	D_{α}^{∞}	$(3.24\pm0.43)\times10^{14}\ s^{-1}$	$(8.37\pm1.74)\times10^{13}\ s^{-1}$,
Activation Energies	$E_{\parallel}^{a}$	32.4 ± 0.5 kJ/mol	52.7 ± 0.6 kJ/mol
	$E_{\perp}^{a}$	24.6 ± 0.4 kJ/mol	35.7 ± 1.2 kJ/mol
	E_{R}^{a}	32.0 ± 0.1 kJ/mol	29.9 ± 0.1 kJ/mol
	E_{α}^{a}	29.5 ± 0.4 kJ/mol	25.6 ± 0.6 kJ/mol

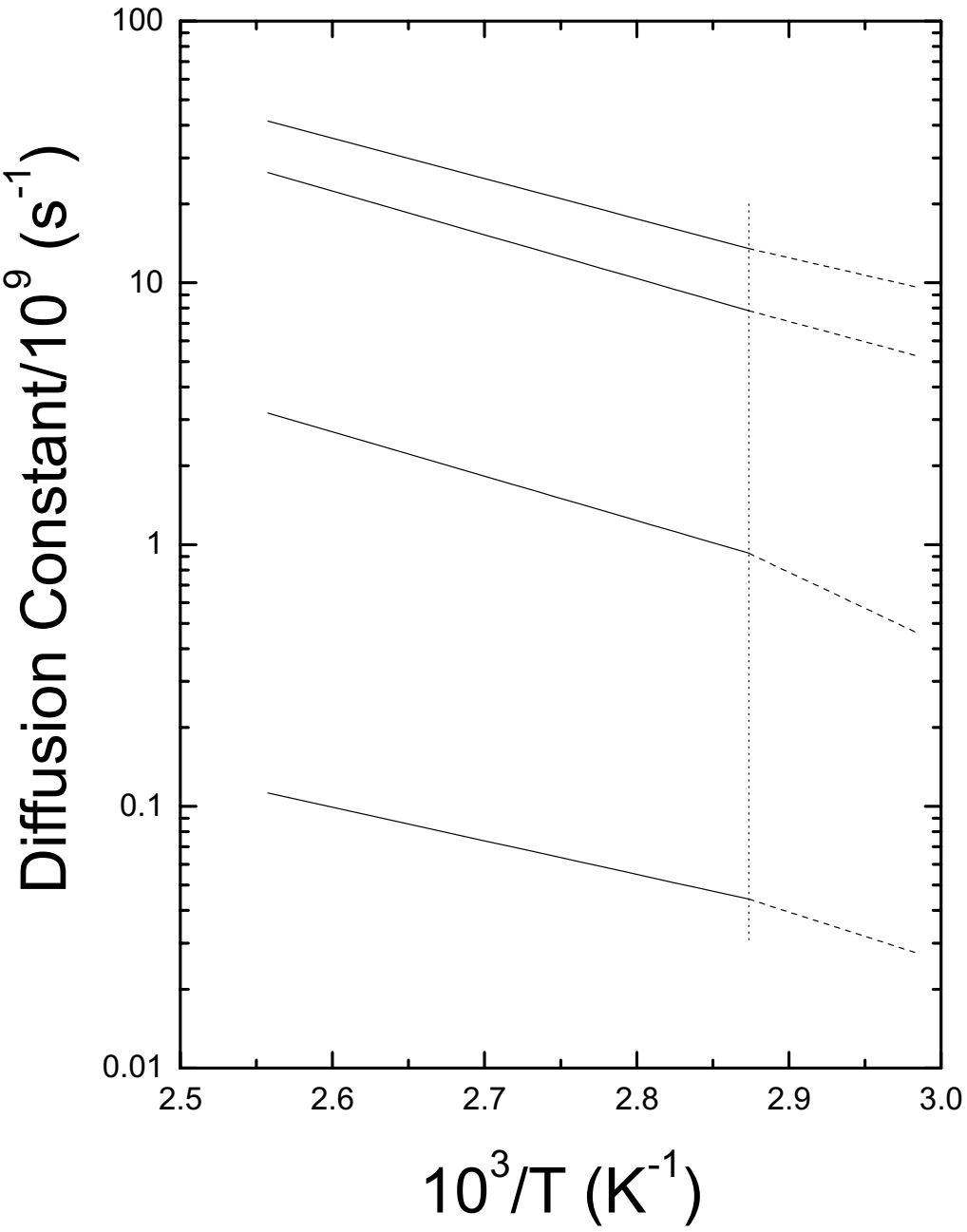

Fig. 4.5 Plots of diffusion constants in the SmA (solid lines) and SmC* phase (dashed lines). They are D_α , D_R , $D_\parallel$ and $D_\perp$ starting from the top.

As seen in Fig. 4.5 and Table 4.2, the activation energies for the spinning and tumbling motions increase noticeably in the SmC* phase in comparison to those in the SmA phase as found previously [20], although here we have found that the $D_\parallel / D_\perp$ ratio is about 30,

which is larger than 8 according to the Perrin model [22]. The reasons for an increase in the activation energies for both the spinning and tumbling motion in the SmC* phase could be due to the smaller layer thickness and the helical structure. It is noted that $D_{\perp}^{\infty}$ is not as well determined in the SmC* phase. This might be due to the smaller number of available spectral densities. The activation energies for the internal ring flips and bond rotation of the C_{α} methylene group in the SmC* phase are marginally changed to lower values.

A valuable concern is raised about the possibility that molecules diffuse along the helical pitch in the SmC* phase. This might influence the molecular orientation process and thus spectral densities. We believe that the diffusion process along the pitch axis is only fast in the high temperature cholesteric and blue phases. Considering a typical diffusion constant D is on the order of 10^{-7} cm^2/s, and the correlation time (measurement time) in smectic C* phase $\tau \sim 10^{-4}$ s - 10^{-5} s, a molecule diffusion distance $\sqrt{D\tau} \approx 0.01$ μm is found to be smaller than a typical pitch length of 50 μm [32] in a similar chiral compound. The molecular translational diffusion is quite slow as compared to rotation diffusion, or to say, they are not on the same time scale. Hence, the change in molecular reorientation due to molecular translation diffusion along the pitch axis is negligible in comparison to the rotational diffusive motion. There is also evidence of small translation contribution in comparison with rotational contribution in the SmC* phase of a ferroelectric liquid crystal based on angular dependent proton relaxation studies [33].

In summary, we have demonstrated that the relaxation data in the tilted SmC* phase of

the studied deuteron sites can be reasonably interpreted based on the concept that molecules are tilted in the external magnetic field and the helicoidal structure formed by them effectively makes the biaxial spectral densities unobservable. It is important to point out that meaningful motional parameters can be derived from deuterium NMR relaxation as long as sufficient number of deuterated sites and frequencies are available as noted in the literature [34].

References

1 R.Y.Dong, *Nuclear Magnetic Resonance of Liquid Crystals*, 2nd ed. (Springer, New York, 1997).

2 R.Y.Dong, Phys. Rev. E. **60**, 5631 (1999).

3 E.E.Burnell and C.A.de Lange, *NMR of Ordered Liquid*. (Kluwer Academic Publishers, Dordrecht, Boston, London, 2003).

4 R.Y.Dong, J. Phys. Chem. **100**, 15663 (1996).

5 R.Y.Dong, Mol. Phys. **88**, 979 (1996).

6 R.Y.Dong, A.Carvalho, P.J.Sebastiao, and H.T.Nguyen, Phys. Rev. E **62**, 3679 (2000).

7 R.Y.Dong and X.Shen, J. Chem. Phys. **105**, 2107 (1996).

8 R.B.Meyer, L.Liebert, L.Strzelecki, and P.Keller, J. Phys. Lett. **36** (L69) (1975).

9 A.D.L.Chandani, E.Gorecka, Y.Ouchi, H.Takezoe, and A.Fukuda, Jpn. J. Appl. Phys **28**, L1265 (1989).

[10] A.Yoshizawa, A.Yokoyama, H.Hikuzaki, and T.Hirai, Liq. Cryst. **94**, 513 (1993).

[11] A.Yoshizawa, H.Hikuzaki, and M.Fukumasa, Liq. Cryst. **18**, 351 (1995).

[12] A.Yoshizawa and I.Nishiyama, Mol. Cryst. Liq. Cryst. **260**, 403 (1995).

[13] A.D.Chen, C.D.Poon, T.J.Dingemans, and E.T.Samulski, Liq. Cryst. **24**, 255 (1998).

[14] S.Yoshida, B.Jin, Y.Takanishi, K.Tokumara, K.Ishikawa, H.Takezoe, A.Fukuda, T.Kusumoto, T.Nakai, and S.Miyajima, J. Phys. Soe. Jpn **68**, 9 (1999).

[15] T.Nakai, S.Miyajima, Y.Takanishi, S.Yoshida, and A.Fukuda, J. Phys. Chem. B **103**, 406 (1999).

[16] D.Catalano, M.Cifelli, M.Geppi, and C.A.Veracini, J. Phys. Chem. A **105**, 35 (2001).

[17] R.Y.Dong, L.Chiezzi, and C.A.Veracini, Phys. Rev. E. **65**, 041716 (2002).

[18] D.Catalano, L.Chiezzi, V.Domenici, M.Geppi, C.A.Veracini, R.Y.Dong, and K.Fodor-Csorba, Macromol. Chem. Phys. **203**, 1594 (2002).

[19] L.Chiezzi, V.Domenici, M.Geppi, C.A.Veracini, and R.Y.Dong, Chem. Phys. Lett. **358**, 257 (2002).

[20] V.Domenici, M.Geppi, and C.A.Veracini, Chem. Phys. Lett. **382**, 518 (2003).

[21] R.Y.Dong, Y.B.Chen, and C.A.Veracini, Chem. Phys. Lett. **405**, 177 (2005).

[22] F.Perrin, J. Phys. Radium **5**, 497 (1934).

[23] G.A.Morris, H.Barjat, and T.J.Horne, Prog. NMR Spect. **37**, 197 (1987).

[24] G.A.Morris, J. Magn. Reson. **80**, 547 (1988).

[25] C.F.Polnaszek, G.V.Bruno, and J.H.Freed, J. Chem. Phys. **58**, 3185 (1973).

[26] C.F.Polnaszek and J.H.Freed, J. Chem. Phys. **79**, 2283 (1975).

[27] P.L.Nordio and P.Busolin, J. Chem. Phys. **55**, 5485 (1971).

[28] R.Tarroni and C.Zannoni, J. Chem. Phys. **95**, 4550 (1991).

[29] P.A.Beckmann, J.W.Emsley, G.R.Luckhurst, and D.L.Turner, Mol. Phys. **59**, 97 (1986).

[30] J.W.Doane,"Phase Biaxiality in some of the Smetic Phases" in *Nuclear Magnetic Resonance of Liquid Crystals*, edited by J.W.Emsley (Reidel, Dordrecht, 1985), pp. 431.

[31] W.H.Press, B.P.Flannery, S.A.Teukolsky, and W.T.Vetterling, *Numerical Recipes*. (Cambridge University Press, Cambridge, 1986).

[32] G.Y.Yeap, M.Nakata, Y.Takanishi, K.Ishikawa, and H.Takezoe, Liq.Cryst. **27**, 1437 (2000).

[33] J.L. Figueirinhas, A. Ferraz, A.C. Ribeiro, H.T. Nguyen, and F. Noack, Ferroelectrics **146**, 123 (1993).

[34] L. Calucci and M. Geppi, J. Chem. Inf. Comput. Sci. **41**, 1006 (2001).

5 Lyotropic Liquid Crystal Study of DACl/H_2O Binary System

5.1 Introduction

Using ^{1}H NMR fast field cycling T_1 measurements, Wachowicz *et. al* [1] recently found that *layer undulations* (or ODF), make an important contribution to slow molecular dynamics in both hexagonal and lamellar phase, with different frequency dependence. This indicates a relatively weak interaction between neighbouring decylammonium chloride (DACl) layers in water. But at high frequency region (>10^5 Hz), the fast molecular motions [2] dominate the dynamics, such as internal rotation of alkyl chains about their long molecular axes, trans-gauche isomerization and lateral diffusion. In consideration of fast local orientation and surface diffusion around the aggregate axes, Halle's group[3] proposed a motion model for spin relaxation in the hexagonal phase, which was successfully applied by Dong [4] to interpret the ^{14}N relaxation measurements in a similar binary system. However, the study of the lamellar phase is still rare. Here we present the spin-lattice relaxation data of DACl/H_2O in the lamellar phase by exploiting both ^{2}H and ^{14}N nuclei. Despite the low gyromagnetic ratio of ^{14}N and difficulty in detection of the ^{14}N signals, the ^{14}N spectrum is easily identified and less affected by liquid crystal impurities [5]. With deuterons on the first three alkyl carbon sites of DACl and the associated nitrogen on the head group, an attempt is made to measure their relaxation properties in order to account for the overall molecular motion in the

lamellar phase. Fig. 5.1 illustrates the 3D chemical structure of a DACl molecule.

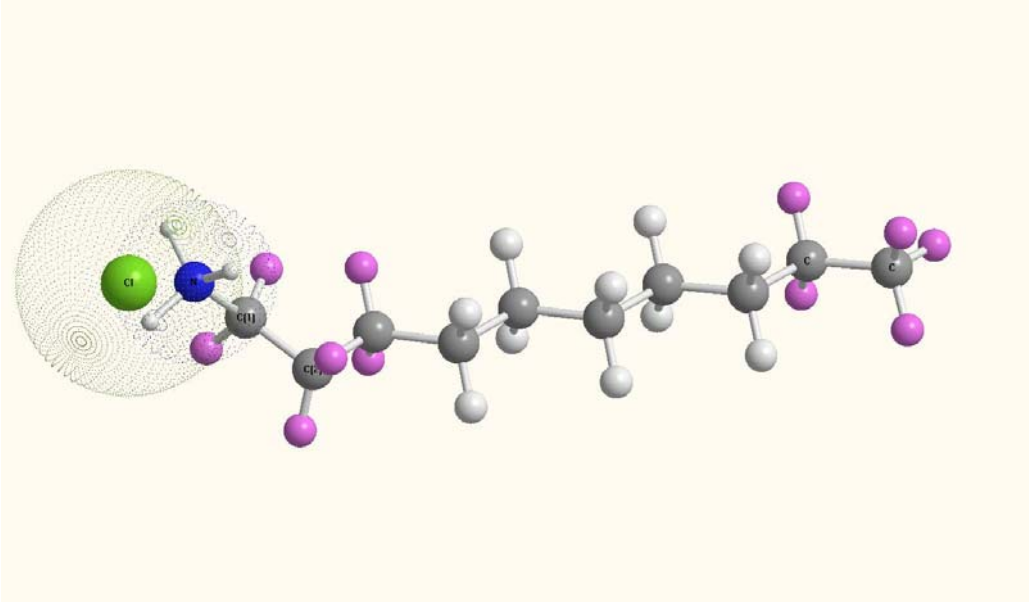

Fig. 5.1 3D structure of a DACl molecule. The ten black atoms in zigzag chain are the hydro-carbon backbone. The head group -$NH3^+$ and Cl^- are hydrophilic and in contact with the water layer, where Cl^- can flow. The hydrogens in deep colour denote deuterated sites under study.

5.2 Geometric Model

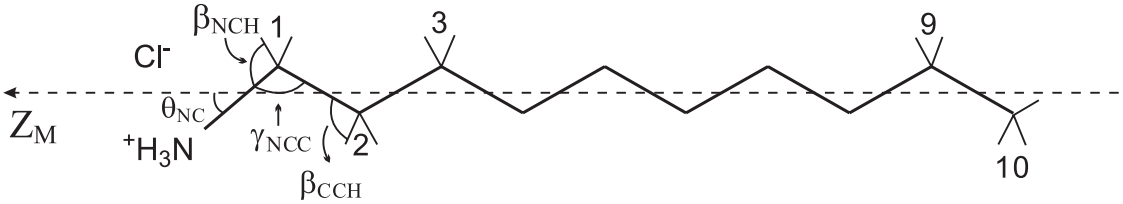

Fig. 5.2 2D Illustration of molecular structure of deuterated DACl at Carbon sites C_1, C_2/C_3, C_9, and C_{10} in its all transformation. The geometric angles will be employed in later discussion of the superimposed rotation model. The dashed line is the long molecular axis Z_M which is more or less parallel to layer normal.

A schematic diagram of the molecular geometry is shown in Fig 5.2. In the lamellar phase, some parts of the DACl geometry are still unknown. When it is in the crystalline phase, C_2 to C_{10} on the DACl chain are supposed to be coplanar, while N and C_1 are displaced significantly from these ideal carbon *zigzag* planes [6,7]. The failure of placing

the N-C_1 bond on the long molecular axis in our spectral density calculations seems to confirm the existence of an angle θ_{NC} between and N-C_1 bond and the long molecular axis. This angle is estimated to be less than 30° [8]. From our simulation of the $^2H_{C1}$ and ^{14}N spectral densities, angles θ_{NC} of 26° and 28° produced satisfactory results for DACl 56 wt.% and 54 wt.%, respectively. However, the uncertainty of the angle θ_{NC} could be 3°. This is due to the lack of enough information in the literature, and the experimental errors (Chapter 2) in the present study because of the instrumentation limit. Both ^2H and ^{14}N are spin I = 1 system. A typical nitrogen NMR doublet (Fig. 5.3) was similar to the deuterium counterparts (Fig. 5.4).

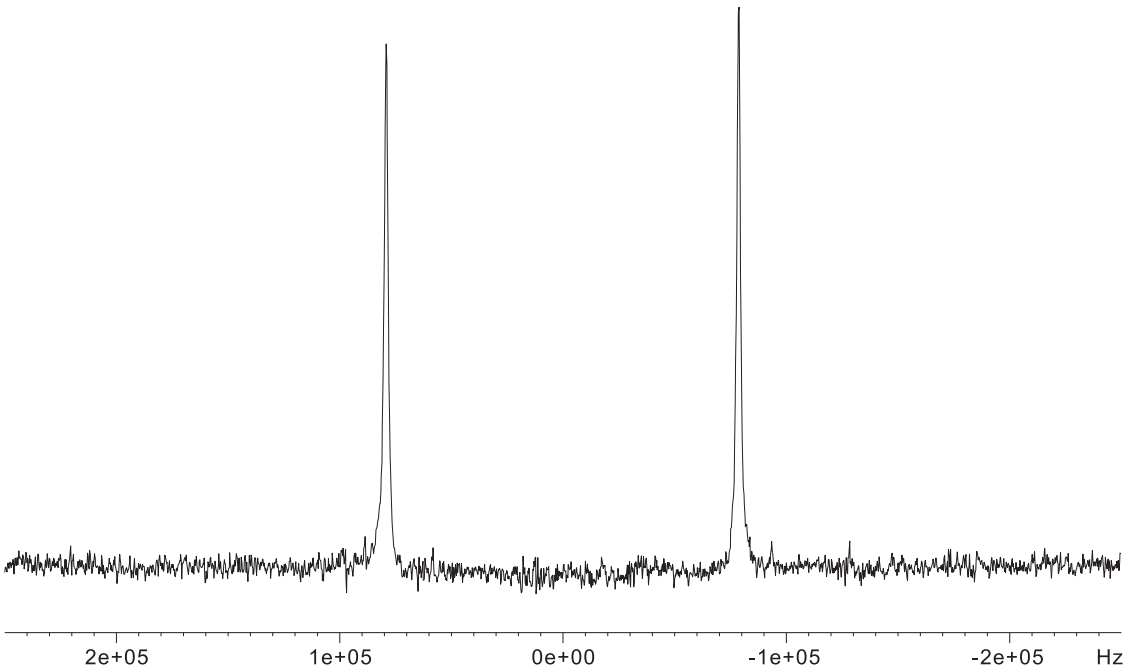

Fig. 5.3 Typical nitrogen NMR spectrum (303.5K) of 56wt.% DACl/H_2O sample. Note that the noise is much greater than that in Fig. 5.4.

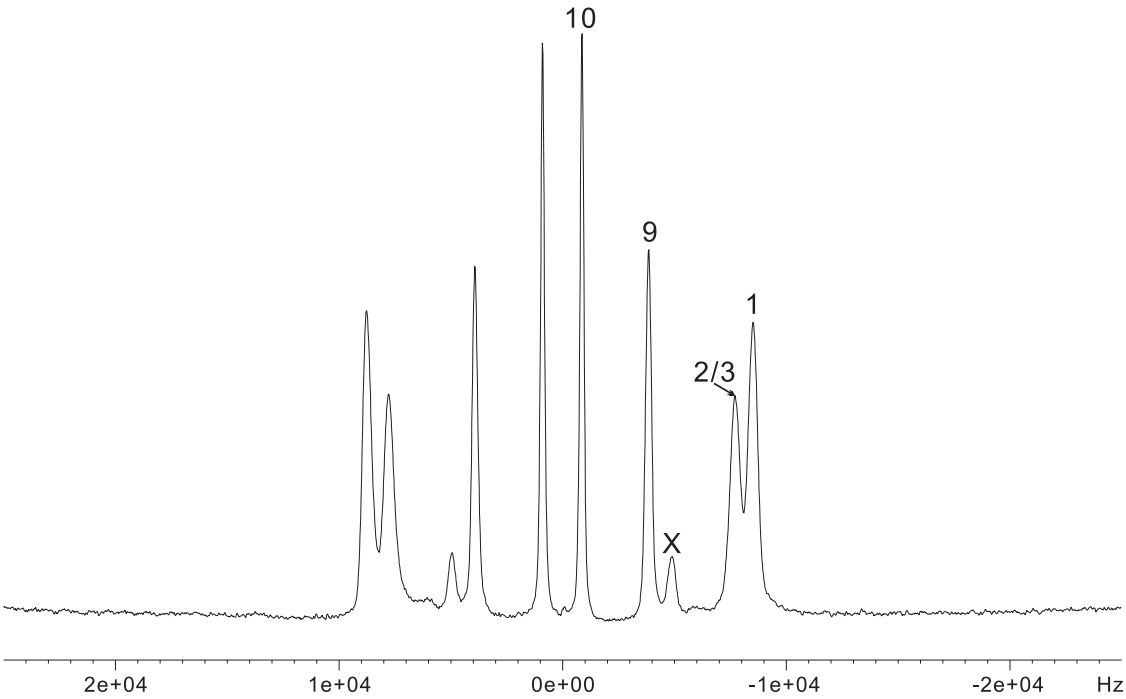

Fig. 5.4 Plot of a typical deuterium spectrum (323K)
with peak assignments of 54 wt.% DACl/H_2O sample.

From the quadrupolar splittings of ^{2}H NMR spectra, segmental order parameters S_{CD} on the C-D bond can be obtained as follows. Recalling Eq. (1.39), in the aligned lamellar phase, the layer normal is perpendicular to the magnetic field [2], and the symmetry axis of the aggregate is along the layer normal. This makes $\Phi = 0°$ and $\Theta = 90°$, and Eq. (1.39) reduces to

$$\Delta\nu_i = \frac{3}{4} q_{CD} S_{CD}^{(i)}, \tag{5.1}$$

where q_{CD} is the quadrupolar coupling constant for the deuteron on the chain, and $S_{CD}^{(i)}$ is the segmental order parameter of the C-D bond of a particular carbon site *i*. Applying Eq. (5.1) to ^{14}N, one obtains

$$\Delta\nu_N = \frac{3}{4} q_N S_{CN} = \frac{3}{4} q_N S_{zz} P_2(\cos\theta_{NC}), \tag{5.2}$$

where q_N is the quadrupolar coupling constant for nitrogen and S_{CN} refers to the segmental order parameter of the C-N bond, and S_{zz} is the nematic order parameter. Similarly for $^2H_{C1}$ on the first carbon site,

$$\Delta\nu_{D_{C_1}} = \frac{3}{4} q_{CD} S_{CD}$$
$$= \frac{3}{4} q_{CD} S_{zz} P_2(\cos\theta_{NC}) P_2(\cos\beta_{NCH}), \quad (5.3)$$

where β_{NCH}=106.7º is used for the angle for N-C_1-H, and q_{CD} is taken to be 170 kHz [9]. Combining Eqs. (5.2) and (5.3) and using the ^2H and ^{14}N splittings yield the value for q_N. The q_N value is found to change weakly in temperature. Thus, it is taken to be the average value, 523.2 kHz for 56 wt.% DACl/H_2O sample and 503.5 kHz for 54 wt.% sample. These values are similar to (but lower than) the value obtained in crystal [8].

Similar to ^2H, ^{14}N spin lattice relaxation time of Zeeman (T_{1Z}) and quadrupolar (T_{1Q}) orders can be measured simultaneously using BBJB-M_∞ sequence described in Chapter 2 to give spectral densities $J_1(\omega_0, \Theta)$ and $J_2(2\omega_0, \Theta)$ [Eq. (3.4) and (3.5)], where $\omega_0/2\pi$ is the Larmor frequency, and Θ is the angle between the external magnetic field and the phase director (see Fig. 2.2). Taking into account the superposition of different kinds of motion, such as collective order fluctuation, molecular rotation, and internal isomerization, these spectral densities can be calculated by a suitable model. AT 9.4 tesla (28.9 MHz) for ^{14}N, collective fluctuations of layers are relatively unimportant [2] and thus we again employ a small step rotation diffusion model [10,11] to describe the molecular reorientations of the head group.

The superimposed bond rotations on the overall motion with strong collision limit [12] is

employed to account for the internal bond motion. The rotational diffusion equation solved by Tarroni and Zannoni [11] is now applied, giving Eqs. (3.37), (3.38) and (3.39) for the spectral densities for the head group nitrogen, deuterons on the first and the second carbon site, respectively. Here β_{NCH} is taken to be 107.5º, and γ_{NCC} is assumed to equal ∠C-C-C of 113.5º [13,14].

In the lamellar phase, since the layer normal is perpendicular to the applied magnetic field, the angle θ of 90º in Eqs. (3.40) should be used to give simplified expressions for the measured spectral densities in this study. It is worth to note that lamellar phase is uniaxial when using Eqs. (3.40) here.

5.3 Results and Discussion

The splitting of ^{14}N and ^{2}H of the C_1 site versus temperature are shown in Fig. 5.5 and 5.6, for 54 wt.% and 56 wt.% DACl/H_2O system, respectively. Since no suitable temperature calibration method was available for the ^{14}N measurement, $^{2}H_{C1}$ splittings were used to scale their corresponding nitrogen data, where both splittings display similar temperature dependence. As for the $^{2}H_{C1}$ experiments, the temperatures were calibrated by using the known phase transition temperatures of a deuterated mesogen 5O.7-d_4 [15] . It is also found that in the reduced temperature [16] scale, the quadrupolar splittings of both the ^{14}N and ^{2}H exhibit very little dependence on the sample concentration.

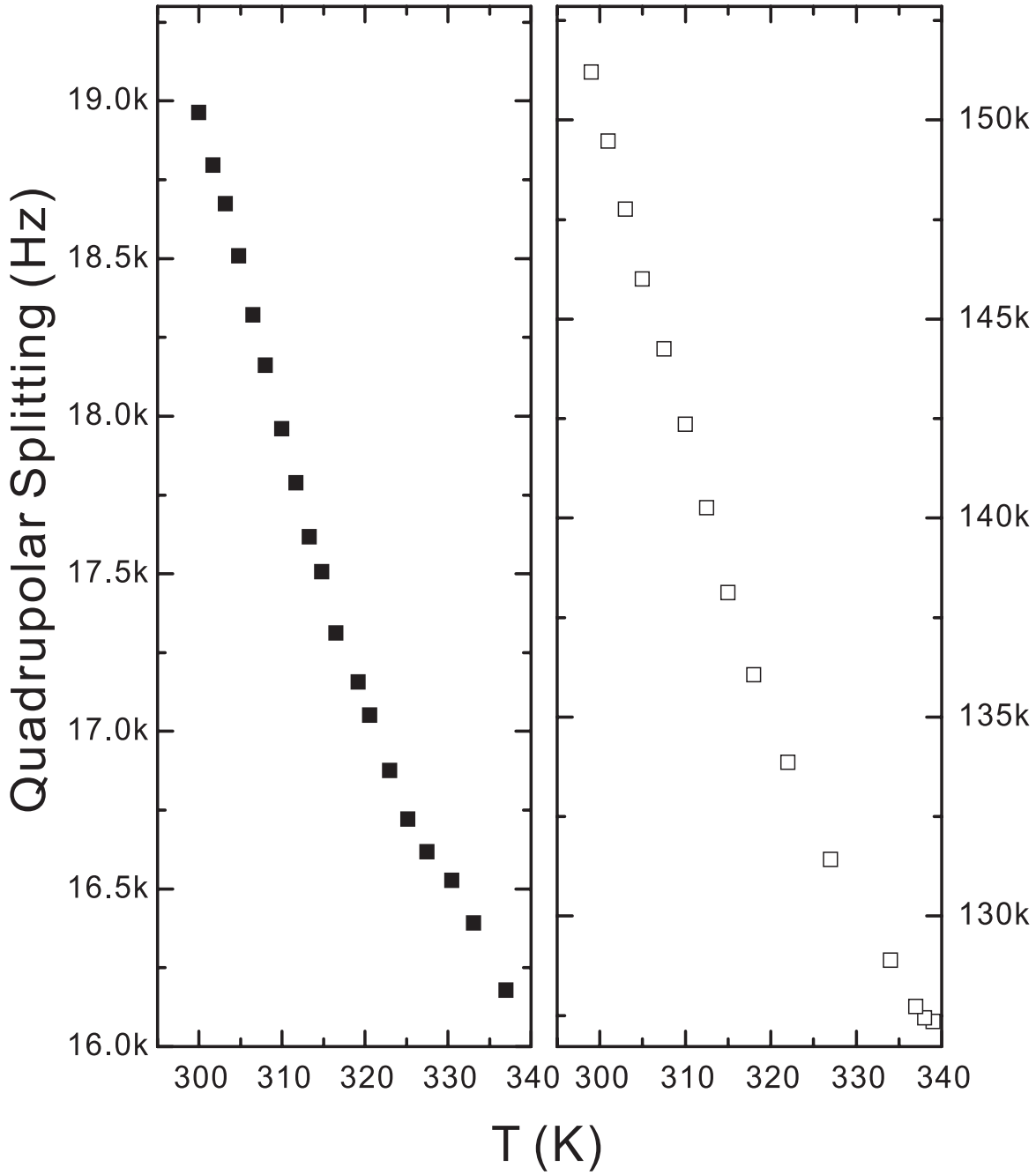

Fig. 5.5 Quadrupolar splittings of 54 wt.% DACl/H_2O sample. The open square is for nitrogen at 28.9MHz, while the close square is for the deuteron on C_1 site at 61.4 MHz. The ratio of splitting of the two nuclei is around 7.92:1.

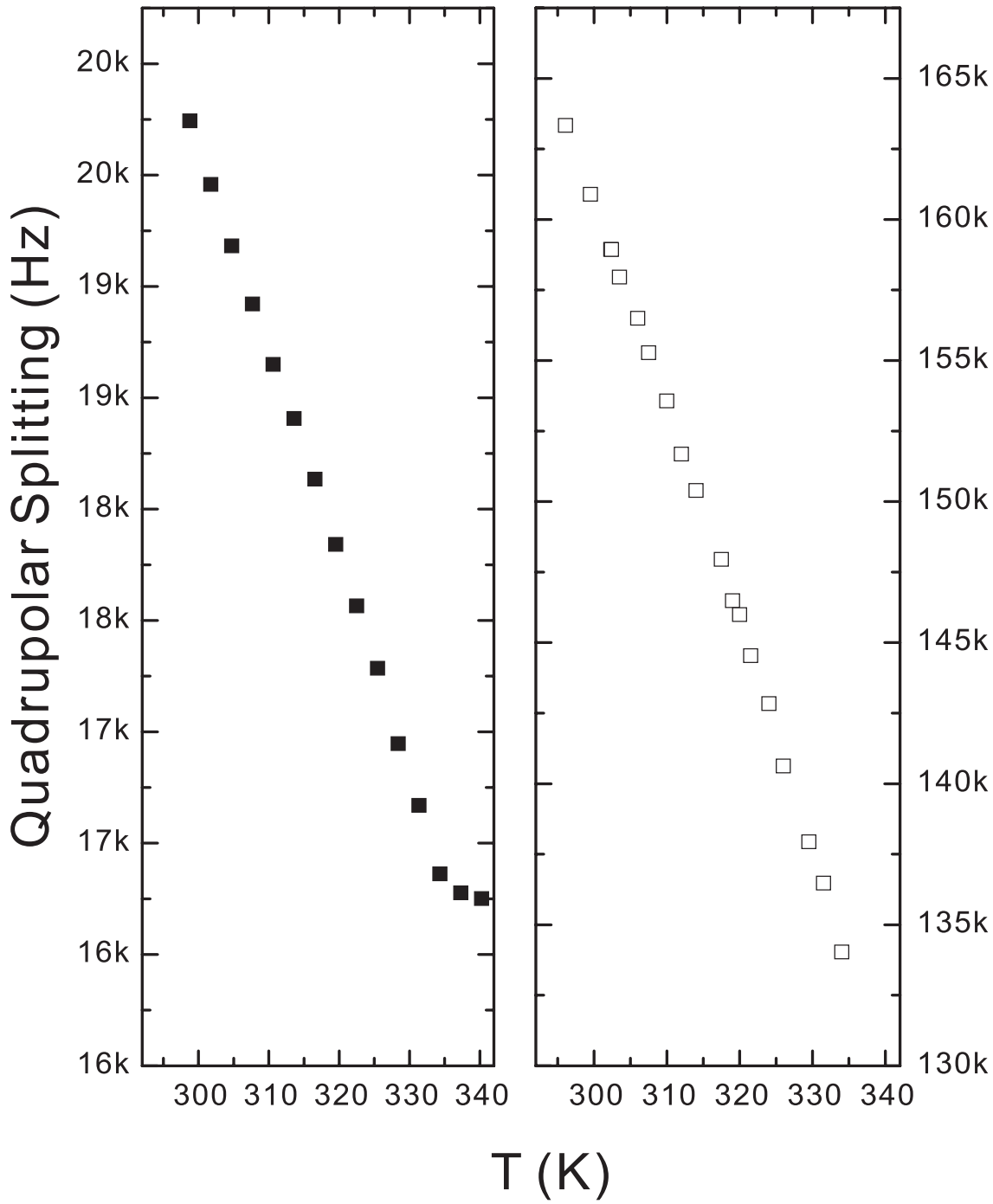

Fig. 5.6 Quadrupolar splittings of 56 wt.% DACl/H_2O sample. The open square is for nitrogen, while. the close square is for the deuteron on C_1 site. The ratio of splitting of the two nuclei is around 8.21:1.

By using Eq. (5.3), and the θ_{NC} value (26º or 28º), the orientational order values vary between 0.45 to 0.57 for the aligned aggregate of DACl molecules in 54 wt.% (θ_{NC}=28º) and 56 wt.% (θ_{NC} = 26º) samples (Fig. 5.7). This S_{zz} and the corresponding θ_{NC} are determined in conjunction with the fitting of the spectral densities. The decrease in splittings (S_{zz}) predicts the progression of disorder with increasing temperature. The slightly higher order in 56 wt.% than in 54 wt.%. DACl/H_2O system is due to the increase in concentration of DACl in the lamellar phase, and the increased viscosity in the sample. The ^2H NMR spectra of selectively deuterated DACl molecules give information about fast anisotropic motions of a particular C-D bond. The quadrupolar splitting of each of C_1~C_{10} deuterons measured in the lamellar phase at two DACl concentrations (54% and 56%) can be used to evaluate the temperature dependence of the C-D bond order parameter, $S_{CD}^{(i)}$, on the basis of Eq. (5.1). Fig. 5.8 presents the segmental order parameters of six deuterated sites on the chain at two concentrations. The value of segmental order parameters $S_{CD}^{(i)}$ (<0.18) as well as the small difference (<15%) among the two concentrations correspond to those reported by Jurga *et. al* [1]. The smaller quadrupolar splitting and consequently the segmental order parameter S_{CD} observed for deuterons further down the carbon-carbon backbone, reflect an increase in motional disorder along the chain, and is a consequence of an increase of gauche conformation probability [1].

Plots of deuteron spectral densities for methylene sites as a function of temperature in the lamellar phase are shown in Fig. 5.9 for two concentrations (54 wt.% and 56 wt.%). At a

glance, crossovers between J_1 and J_2 are pronounced in C_1, and C_2/C_3, in both concentrations. This crossover phenomenon is quite rare among thermotropic liquid crystals [17] and was only detected in a recent work described in chapter 4. In addition, spectral densities for C_1 and C_2/C_3 are of similar values within error limits.

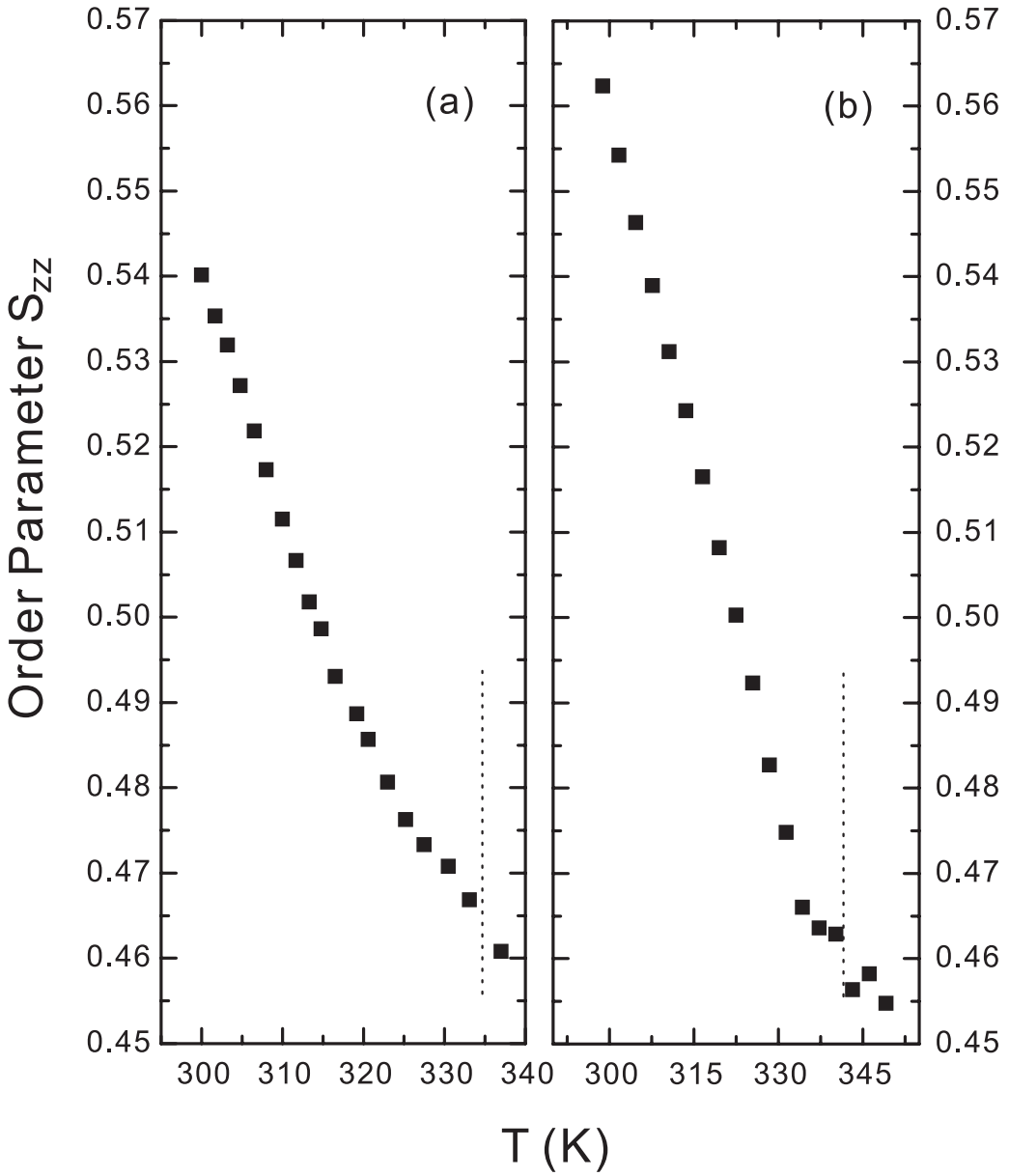

Fig. 5.7 Temperature dependence of order parameter S_{zz} for DACl/H_2O 54 wt.% (a) and 56 wt.% (b) samples. The dotted line is the transition temperature for biphasic lamellar+isotropic region.

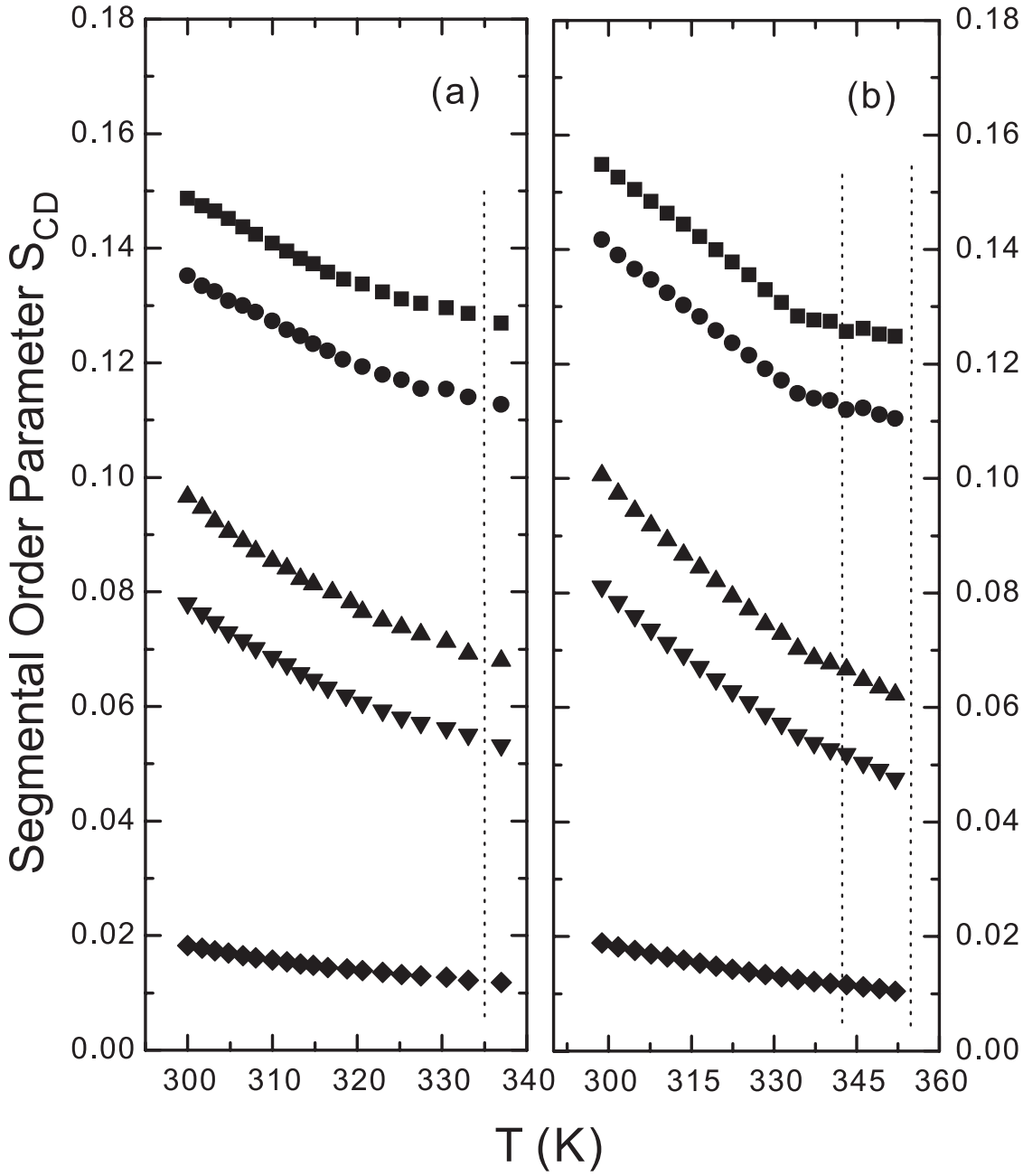

Fig. 5.8 Temperature dependence of segmental order parameters of for C_1, C_2/C_3, C_X, C_9, and C_{10}, segments denoted by squares, circles, up triangles, down triangles, diamonds, respectively, in the system containing 54 wt.% (a) and 56 wt.% (b) DACl in H_2O. In (a), to the right of the dotted line shows the biphasic region. In (b), the region between the dotted lines shows the biphasic region, while the right dotted line indicates the Lamellar-isotropic transition. The splitting in the biphasic region shows little temperature dependence.

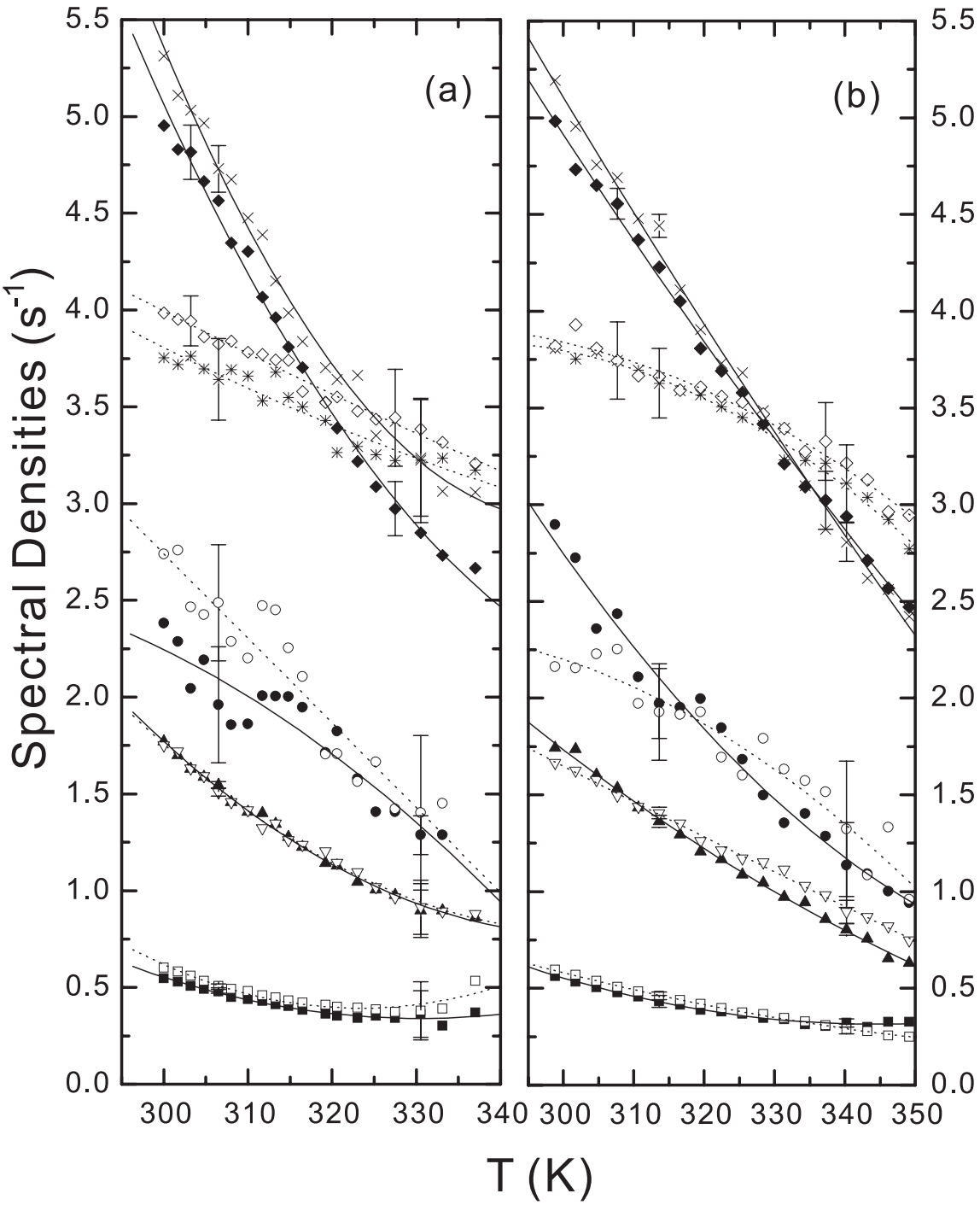

Fig. 5.9 Plot of spectral densities of deuterons on C_1, C_2/C_3, C_X, C_9 and C_{10} of the 54 wt.% (a) and 56 wt.% (b) DACl in water, with the close symbol diamonds, crosses, circles, triangles and squares, for J_1 respectively. The open symbols are the corresponding J_2, except C_2 is denoted by star. The 2nd polynomial fitting curves are just plotted to aid the eyes. The solid curves are for J_1, while the dotted lines for J_2.

Fig. 5.10 and 5.11 show plots of ^{14}N and $^{2}H_{C1}$ spectral densities for 54 wt.% and 56 wt.% DACl/H_2O samples, respectively. There is no obvious crossover in the ^{14}N data in view of larger uncertainties of these data. The two concentrations showing similar temperature behaviours seem to enhance the creditability of our ^{14}N experiments. Using Eqs. (3.37), (3.38) and Eqs. (3.40), we can simulate the smoothed spectral density data in the lamellar phase via a 'global target' approach, in which an Arrhenius behaviour is assumed for the various diffusion constants. As the geometry of the DACl structure in the lamellar phase is not fully known, θ_{NC} is first guessed by trial and error. The order parameter S_{zz} and the quadrupolar coupling constant q_N are then calculated by fitting both splitting data of $^{2}H_{C1}$ and ^{14}N. After several simulations with an averaged q_N value, θ_{NC} is determined by the best fitting quality of ^{14}N and ^{2}H spectral densities. Now the temperature dependence can be written as $D_i = D_i^{\infty} \exp[-E_a^i / RT]$, where i is the specific type of motion. Instead of fitting D_i^{∞}, the diffusion coefficients at some particular temperature, D_{iT} were used. Before running the global target program, a 'single temperature' fitting approach facilitates the estimation of approximate values, which can later be used as initial input of the fitting parameters. Apart from predicting $D_{\parallel}$ and $D_{\perp}$ for both ^{14}N and ^{2}H, another internal rotational diffusion parameter, D' is included for rotating the methylene group about the N-C bond in the superimposed rotation model. Now at each temperature, four spectral densities determine three parameters, and the quality of the fit for the 54% sample was good (f = 0.08). The minimization of the sum square fractional error f given by Eq. (5.4) is carried out using AMOEBA,

$$f = \sum_k \sum_i \sum_m \frac{[J_m^{(i)Cal}(m\omega) - J_m^{(i)Exp}(m\omega)]_k^2}{[J_m^{(i)Exp}(m\omega)]_k^2}, \tag{5.4}$$

where the sum over k is for 16 temperatures, the sum over i covers sites '^{14}N', '$^{2}H_{Cl}$', and m=1 and 2 (^{14}N for 28.9MHz, and ^{2}H for 61.4MHz only).

Calculated spectral densities from our global analysis at 28.9 MHz and 61.4 MHz are shown as curves (solid lines for J_1, while dotted lines for J_2). In total, 4×16＝64 spectral densities are used to obtain 6 parameters. As seen in this diagram, the fitting quality for both nuclei is quite good and the crossovers of J_1 and J_2 in Fig. 5.10 and 5.11 are reproduced. As a consequence, the derived motional parameters shown in Fig. 5.12 should be quite reliable. Table 5.1 summarizes the result for diffusion coefficients and their activation energies. The error limits are estimated by varying one parameter while fixing the rest to their best values to yield a doubling in f value.

Unusually, the tumbling motion is found to be comparable to the spinning motion, which seems unrealistic at a glance. This is in view of the molecules being anchored at the interfacial lamellar layers. However, if the layer undulations are considered, comparable values of tumbling to spinning motion would indicate a rigorous motion of the local directors of aggregates of molecules. A simple physical picture is that the 2D lamellar layers resemble a wavy sea, where the 'water' surface is up and down, thereby leading to an apparent increase of the tumbling constant for the long molecular axis. Nevertheless, the activation energy for the spinning motion is lower than that for the tumbling motion. This seems reasonable since the DACl molecules are easier to rotate as they are loosely

anchored on the water surface.

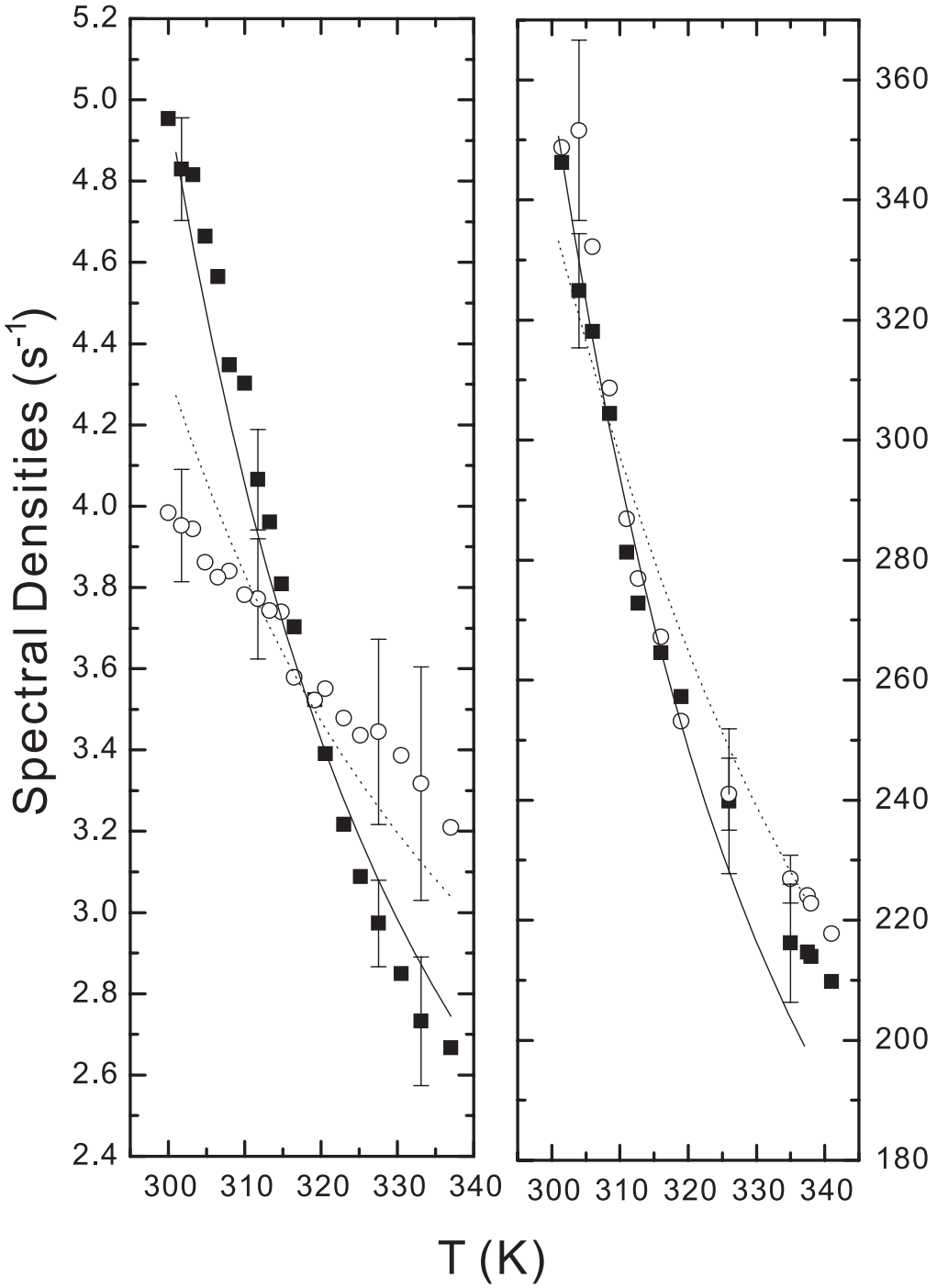

Fig. 5.10 Plots of spectral densities of both ^{2}H and ^{14}N of 54 wt.% DACl in water. The closed square and open circle refer to J_1 and J_2 respectively. Solid and dotted lines are for the corresponding calculated value J_1 and J_2 respectively. The left graph is for ^{2}H experiment, while the right for ^{14}N.

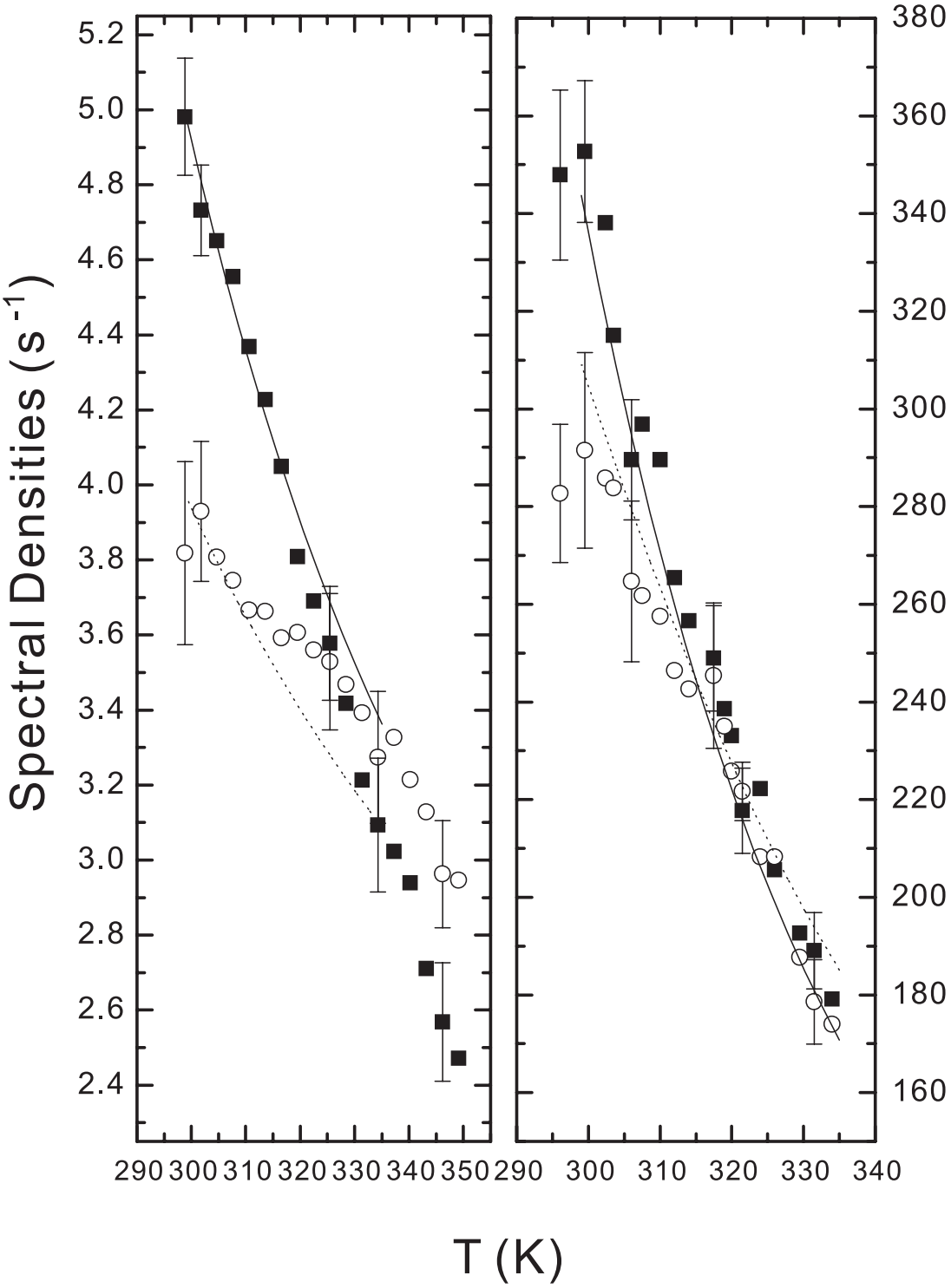

Fig. 5.11 Plots of spectral densities of both ^{2}H and ^{14}N of 56 wt.% DACl in water. The closed square and open circle refer to J_1 and J_2 respectively. Solid and dotted lines are for the corresponding calculated value J_1 and J_2 respectively. The left graph is for ^{2}H experiment, while the right for ^{14}N.

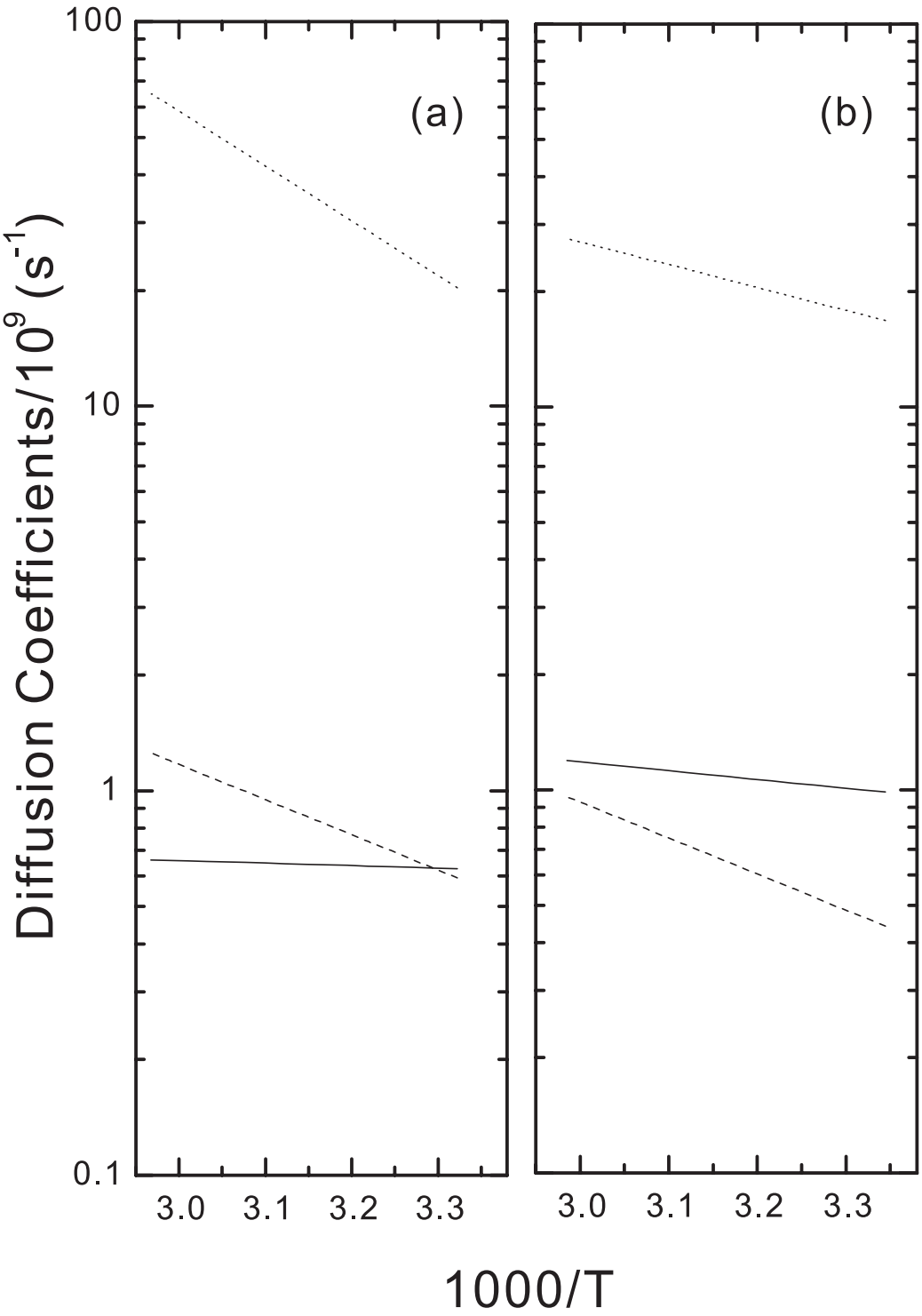

Fig. 5.12 Plots of diffusion constants for DACl/H_2O sample with a 54 wt.% (a) and 56 wt.% (b) DACl. The solid line, dashed line and dotted line represent $D_{\parallel}$, $D_{\perp}$ and D', respectively.

Table 5.1 Fitting parameters of diffusional coefficients and activation energies with error limits.

		54 wt.%	56 wt.%
Pre-exponential Factor	$D_{\parallel}^{\infty}$	$(1.02 \pm 0.08) \times 10^{9} s^{-1}$	$(5.60 \pm 0.57) \times 10^{9} s^{-1}$
	$D_{\perp}^{\infty}$	$(5.96 \pm 0.64) \times 10^{11} s^{-1}$	$(5.73 \pm 0.81) \times 10^{11} s^{-1}$
	D'^{∞}	$(9.48 \pm 1.09) \times 10^{14} s^{-1}$	$(1.57 \pm 0.16) \times 10^{12} s^{-1}$
Activation Energies	$E_{\parallel}^{a}$	1.24 ± 0.20 kJ/mol	4.37 ± 0.27 kJ/mol
	$E_{\perp}^{a}$	17.5 ± 0.3 kJ/mol	18.0 ± 0.4 kJ/mol
	E'^{a}	27.2 ± 0.3 kJ/mol	11.4 ± 0.3 kJ/mol

As a step further, relaxation information of deuterons on C_2/C_3 have also been examined using the superimposed rotations model. Taking an additional superimposed rotation into account, Eq. (3.39) is used with D'' for the C_2/C_3 methylene rotation, while the results of $D_{\parallel}$, $D_{\perp}$ and D' and their corresponding activation energies $E_{\parallel}^{a}$, $E_{\perp}^{a}$ and E'^{a} obtained from the previous simulation are fixed in the global target approach.

However, the similarity of the relaxation values of C_1 segment and C_2/C_3 segment is doomed to fail this attempt. Fig. 5.13 shows the results of the simulation of deuterium spectral densities on C_2 site in both 54 wt.% and 56 wt.% samples. The fittings were not good and no crossover could be reproduced. The diffusion coefficients D'' for 54 wt.% and 56 wt.% samples are small (4.78×10^{9} at 301K and 7.26×10^{9} at 299K) in comparison to the corresponding D' on the C_1 site ($20.34 \times 10^{9}$and 16.83×10^{9}). Similarly the activation energies for D'' are also smaller than their counterparts for D' in both

concentrations (see Table 5.2). Plots of spectral densities at a selected temperature as a function of D'' are plotted in order to find the range of possible fitting parameter D'', as shown in Fig. 5.14. It seems that J_1 and J_2 of $^2H_{C2}$ can not be simulated with the same D'' value. Normally, under the superimposed motion theory, C_2/C_3 has more flexibility (higher disorder), and thus longer relaxation time. The overlapping of C_2 and C_3 doublets should even help their spectral densities deviate from the C_1 data. The fact that the three carbon sites relax similarly may suggest that C_1-C_2-C_3-C_4 behave as a "rigid" group and share more or less the same diffusion parameter. Therefore, the superimposed rotations model is not a suitable model to account for the C_2/C_3 relaxation data. A fully deuterated $DACl/H_2O$ sample is, however, required for testing correlated rotations in the flexible C-C backbone using the decoupled model [18].

Table 5.2 Fitting parameters of diffusional coefficients D'' and activation energies.

	54 wt.%	56 wt.%
D''^{∞}	$4.78\times10^{9}s^{-1}$	$2.43\times10^{11}s^{-1}$
E''^{a}	0 kJ/mol	8.7 kJ/mol

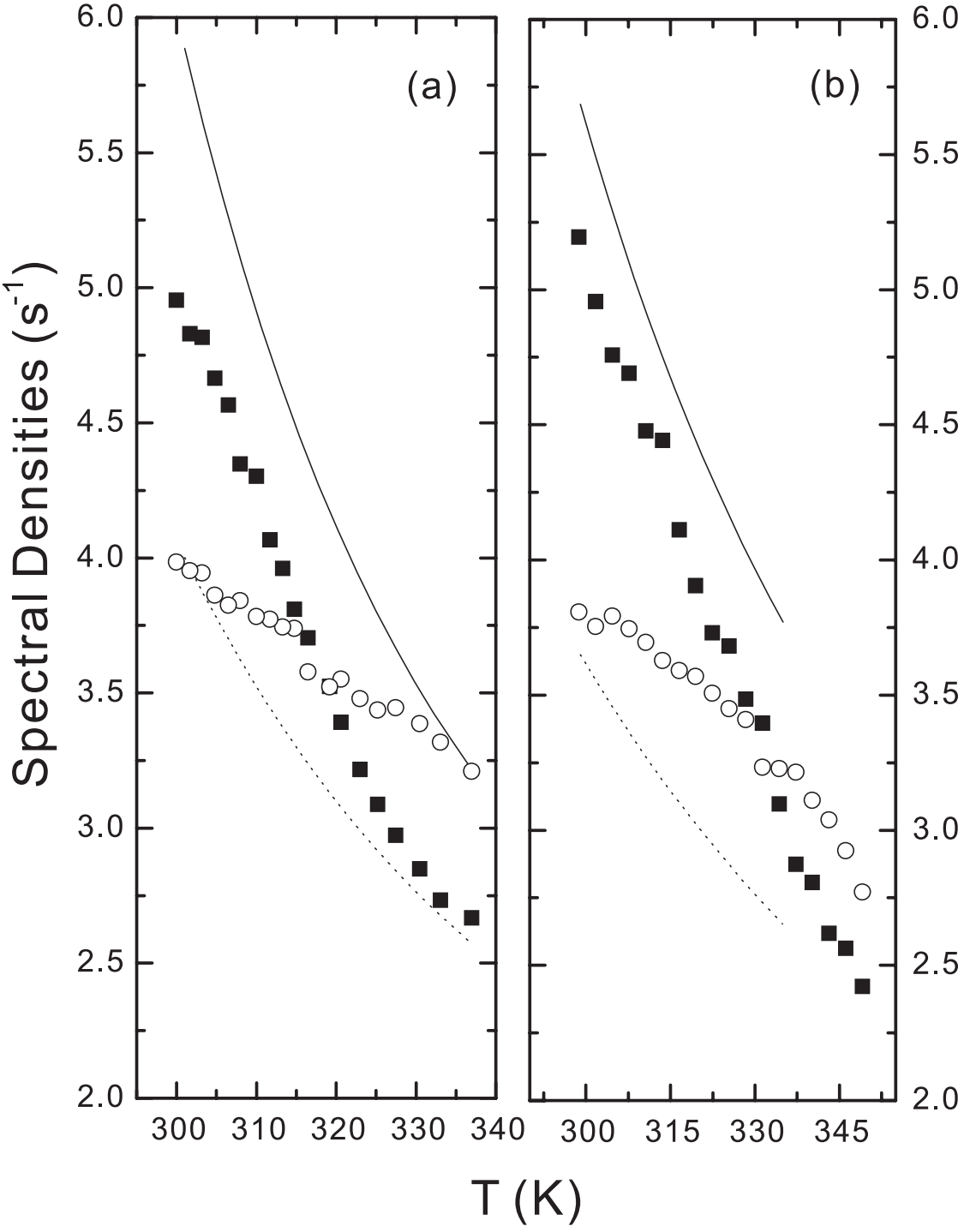

Fig. 5.13 Plots of spectral densities of deuterons on C_2 site of 54 wt.% (a) and 56 wt.% (b) DACl in H_2O. The square and open circle represent experimental values of J_1, J_2, respectively. The solid line is for calculated value of J_1, while the dotted for calculated value of J_2.

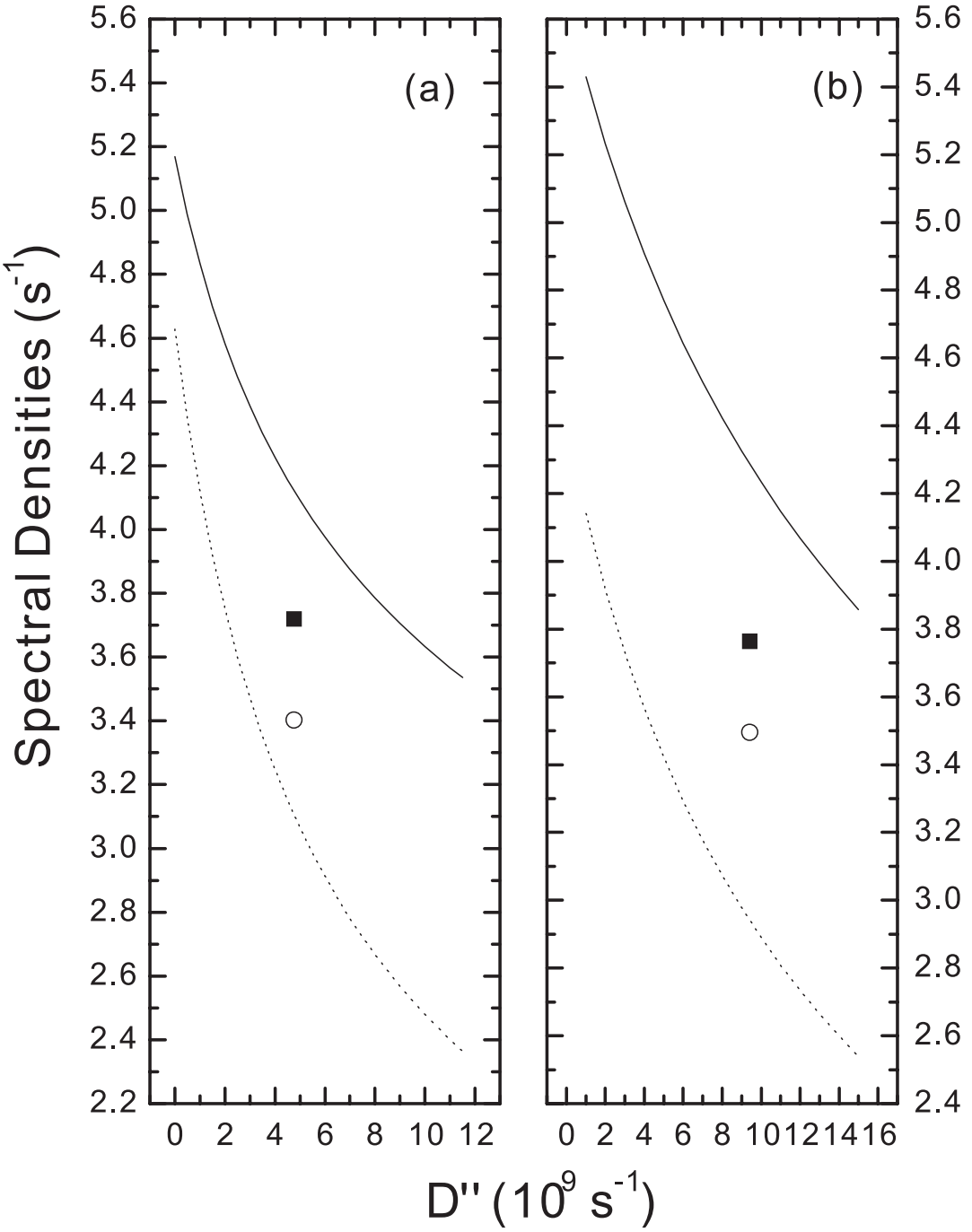

Fig. 5.14 Plots of Spectral densities vs. diffusion coefficient D'' on the $^2H_{C2}$ site of 54 wt.% (a) and 56 wt.% (b) DACl/H_2O. The left graph is for 320.2K, and the right for 323K. Squares and open circles represent the experimental J_1 and J_2 at the best fitting D'', respectively. The solid line is for calculated value of J_1, while the dotted line for experimental J_2.

In conclusion, the overall rotational diffusion model plus the internal superimposed rotation model with strong collision limit have been applied to study the dynamics of lyotropic liquid crystal in the lamellar phase. The relaxation data of studied C_1 deuteron and nitrogen sites provide a way to investigate the head group motion at the water interface. Given the geometry of the molecule and sufficient number of deuterated sites and frequencies, some meaningful motional parameters could be obtained to account for the chain dynamics of the molecules in the lamellar phase.

References

[1] M.Wachowicz, S.Jurga, and M.Vilfan, Phys. Rev. E. **70**, 031701 (2004).

[2] Z.Fojud, E.Szczeniak, S.Jurga, S.Stapf, and R.Kimmich, Solid State Nuc. Mag. Reson. **25**, 200 (2004).

[3] P.Quist, B.Halle, and I.Furo, J. Chem. Phys. **95**, 9 (1991).

[4] R.Y.Dong, Mol. Phys. **99**, 637 (2001).

[5] R.Y.Dong, E.Tomchuk, J.J.Visintainer, and E.Bock, Mol. Cryst. Liq. Cryst. **33**, 101 (1976).

[6] G.J.Kruger, M.Rademeyer, and D.G.Billing, Acta Cryst. E **59**, o480 (2003).

[7] M.Gorden, Acta Cryst. **6**, 739 (1953).

[8] J.Seliger, V.Zagar, and R.Blinc, J. Chem. Phys. **78**, 5 (1982).

[9] P.Li M.Jansson, J. Chem. Phys. **93**, 1448 (1989).

[10] P.L.Nordio and P.Busolin, J. Chem. Phys. **55**, 5485 (1971).

[11] R.Tarroni and C.Zannoni, J. Chem. Phys. **95**, 4550 (1991).

[12] P.A.Beckmann, J.W.Emsley, G.R.Luckhurst, and D.L.Turner, Mol. Phys. **59**, 97 (1986).

[13] C.J.R.Counsell, J.W.Emsley, N.J.Heaton, and G.R.Luckhuist, Mol. Phys. **54**, 847 (1985).

[14] D.Catalano, L.Chiezzi, V.Domenici, M.Geppi, C.A.Veracini, R.Y.Dong, and K.Fodor-Csorba, Macromol. Chem. Phys. **203**, 1594 (2002).

[15] R.Y.Dong and K.R.Sridharan, J. Chem. Phys. **82**, 11 (1985).

[16] R.Y.Dong, *Nuclear Magnetic Resonance of Liquid Crystals*, 2nd ed. (Springer, New York, 1997).

[17] R.Y.Dong, Prog. in NMR Spect. **41**, 115 (2002).

[18] R.Y.Dong, Phys. Rev. A **43**, 4310 (1991).

Brief Conclusion

Nuclear spin relaxation measurements can be used to study the molecular dynamics of liquid crystals. The present deuterium study of 8BEF5-d_{15} shows that by including the tilt angle w.r.t the pitch axis (the magnetic field), the liquid crystal molecules in the chiral smectic C (SmC*) phase can be treated as in an uniaxial phase. This assumption simplifies the calculation of spectral densities, and makes it possible to obtain meaningful parameters. The diffusion coefficients in the SmC* phase are found to vary continuously from the SmA phase. The higher activation energies in the SmC* are reasonable due to the twisted structure of molecules in the chiral phase.

As another spin one nucleus, ^{14}N NMR not only shares the same theory as ^{2}H NMR, but also has its own advantage in yielding significant information of molecular dynamics. At the head group of DACl-d_{11} molecules, the ^{14}N spin-lattice relaxation measurements in conjunction with $^{2}H_{C1}$ data can give us the overall motional information of the molecule in the lamellar phase. Our ^{14}N and ^{2}H study also show that one can gather more reliable information on the location of the long molecular axis and account for the dynamics of the molecule in the lamellar phase. The studied lyotropic liquid crystal in its lamellar phase can be treated similarly to that of a thermotropic SmA phase. In the lamellar phase, $D_{\perp}$ seems to be comparable to $D_{\parallel}$, which means a rigorous "tumbling" motion of the local directors of aggregates. This appears to be closely tied to layer undulations. On the other hand, lower activation energy for the spinning motion than that of the tumbling

motion shows that it is easier for molecules to rotate as they are loosely anchored. A series of ^{14}N experiments on samples with different concentrations of DACl in the lamellar phase are expected to confirm the geometry of the molecule and the current results.

Appendix A

Diffusion Equation for Relaxation [1]

Among different types of orienting potential [2-8] $U(\Omega)$ present in the mesophases, the case of uniaixal molecule reorienting in uniaxial phases is described here. The orientational distribution function $P(\Omega)$ and the conditional probability function $P(\Omega_0 \mid \Omega t)$ are obtained by solving the rotational diffusion equation

$$\frac{\partial P(\Omega_0 \mid \Omega t)}{\partial t} = -\sum_{\alpha\beta} L_\alpha D_{\alpha\beta} \left\{ L_\beta + L_\beta \left[\frac{U(\Omega)}{k_B T} \right] \right\} P(\Omega_0 \mid \Omega t) \tag{A.1}$$

where $L_\alpha = (L_x, L_y, L_z)$ is a component of a dimensionless angular momentum operator $\vec{L}$, and $\hat{D}$ is a rotational diffusion tensor diagonalized in a fixed molecular frame [2]. And the following quantities related to the diffusion tensor components are introduced for convenience.

$$\rho = \frac{D_x + D_y}{2}, \quad \varepsilon = \frac{D_x - D_y}{D_x + D_y}, \quad \eta = \frac{2D_z}{D_x + D_y} \tag{A.2}$$

where ρ is the tumbling motion of the molecule, ε refers to the asymmetry parameter of the diffusion tensor, and η expresses the ratio between spinning and tumbling of the molecule. In the case of a symmetric rod molecule [2,3], $D_x = D_y$, then ρ becomes $D_\perp$, the diffusion constant of the molecule about an axis perpendicular to the its z axis, and η is the ratio of the parallel and perpendicular diffusion constants ($D_\parallel / D_\perp$). The above diffusion equation becomes

$$\frac{1}{D_\perp}\frac{\partial P(\Omega_0 \mid \Omega t)}{\partial t} = -\left\{L_x^2 + L_x\left[L_x \frac{U(\Omega)}{k_B T}\right]\right\} P(\Omega_0 \mid \Omega t)$$
$$-\left\{L_y^2 + L_y\left[L_y \frac{U(\Omega)}{k_B T}\right]\right\} P(\Omega_0 \mid \Omega t)$$
$$-\eta\left\{L_z^2 + L_z\left[L_z \frac{U(\Omega)}{k_B T}\right]\right\} P(\Omega_0 \mid \Omega t)$$
$$\equiv \Gamma P(\Omega_0 \mid \Omega t)\,, \tag{A.3}$$

where Γ is the diffusion operator which, for the purpose of numerical calculations, can be rewritten using unitary transformation as

$$\hat{\Gamma} = P^{-1/2}(\Omega)\Gamma P^{1/2}(\Omega)$$
$$= -\left\{\nabla^2 + \frac{1}{2}\left[\nabla^2 \frac{U(\Omega)}{k_B T}\right] - \frac{1}{4}\left[L_+ \frac{U(\Omega)}{k_B T}\right]\left[L_- \frac{U(\Omega)}{k_B T}\right] - \frac{1}{4}\eta\left[L_z \frac{U(\Omega)}{k_B T}\right]^2\right\}, \tag{A.4}$$

where the nabla operator $\nabla^2 = L_x^2 + L_y^2 + \eta L_z^2$, and $L_\pm = L_x \pm iL_y$ is the angular momentum step operator, and $P(\Omega)$ denotes the orientational distribution function. The diffusion equation in this symmetrized form is given by

$$\frac{1}{D_\perp}\frac{\partial \hat{P}(\Omega_0 \mid \Omega t)}{\partial t} = \hat{\Gamma}\hat{P}(\Omega_0 \mid \Omega t)\,, \tag{A.5}$$

where

$$\hat{P}(\Omega_0 \mid \Omega t) = P^{-1/2}(\Omega)P(\Omega_0 \mid \Omega t)P^{1/2}(\Omega_0) \tag{A.6}$$

is the symmetrized conditional probability. Now the symmetrized diffusion equation is solved using a matrix representation in a basis of normalized Wigner matrices

$$\mathcal{D}_{m,n}^L(\Omega) = \sqrt{(2L+1)/8\pi^2}\, D_{m,n}^L(\Omega) \tag{A.7}$$

In particular,

$$\hat{P}(\Omega_0 \mid \Omega t) = \sum_{Lmn} C_L^{mn}(\Omega_0, t) \mathcal{D}_{m,n}^{L}(\Omega) \tag{A.8}$$

where the expansion coefficients, C_L^{mn}, are evaluated by using the initial condition $\hat{P}(\Omega_0 \mid \Omega, 0) = \delta(\Omega - \Omega_0)$ to give

$$C_L^{mn}(\Omega_0, 0) = \mathcal{D}_{m,n}^{L*}(\Omega_0) \tag{A.9}$$

By substituting Eq. (A.8) in Eq. (A.5), multiplying both sides of the left by $\mathcal{D}_{m,n}^{L*}(\Omega)$ and integrating over Ω, a system of linear differential equations is obtained:

$$\frac{1}{D_\perp} \dot{C}(t) = \hat{R} C(t), \tag{A.10}$$

where

$$\hat{R}_{L'm'n',Lmn} = \int d\Omega \mathcal{D}_{m',n'}^{L'*}(\Omega) \hat{\Gamma} \mathcal{D}_{m,n}^{L}(\Omega) \tag{A.11}$$

The explicit expressions for the matrix elements $\hat{R}_{L'm'n',Lmn}$ depend on the orienting potential $U(\Omega)$. The form of $U(\Omega)$ can be chosen on the basis of symmetry of the phase and of the molecule. The matrix representation of $\hat{\Gamma}$ in a Winger basis set $\mathcal{D}_{m,n}^{L}(\Omega)$ is real and symmetric, and is thereafter called the diffusion operator matrix $\hat{R}$. This should not be confused with $\hat{D}$. In the presence of $U(\Omega)$, the $\hat{R}$ matrix will not be diagonal.

In consideration of the simplest orienting potential, where cylindrical molecules in uniaxial phases like nematic and smectic A are applicable, $U(\Omega)$ is independent of α and γ and reduces to $U(\beta)$. The equilibrium orientational distribution $P(\Omega)$ is connected to the Boltzmann distribution

$$P(\beta) = \frac{\exp[-U(\beta)/k_B T]}{\int d\Omega \exp[-U(\beta)/k_B T]}. \tag{A.12}$$

For uniaxial molecules in uniaxial phases, there will be no coupling between terms with

different *m* and *n*. Hence *m* and *n* can be used to label the diffusion matrices, that is,

$$(\hat{R}^{mn})_{L',L} = \hat{R}_{L'm'n',Lmn}\delta_{m,m'}\delta_{n,n'} \tag{A.13}$$

In solving the set of linear differential equations [Eq. (A.10)], a unitary eigenvector matrix $\hat{X}^{mn}$ which diagonalizes the self-adjoint diffusion matrix $\hat{R}^{mn}$ can be introduced such that

$$\hat{R}^{mn}\hat{X}^{mn} = \hat{X}^{mn}\hat{r}^{mn}, \tag{A.15}$$

where $\hat{r}^{mn}$ is a diagonal matrix which contains the eigenvalues of $\hat{R}^{mn}$. The formal solution is

$$C^{mn}(t) = \hat{X}^{mn}\exp(D_{\perp}\hat{r}^{mn}t)(\hat{X}^{mn})^{T}C^{mn}(0) \tag{A.16}$$

Considering the matrix elements of $\hat{X}^{mn}$ and substituting the zero time coefficients, it follows

$$C_{L}^{mn}(\Omega_0,t) = \sum_{K}\sum_{L'}(\hat{X}^{mn})_{L,K}\exp(D_{\perp}\hat{r}_{K}^{mn}t)(\hat{X}^{mn})_{L',K}^{T}D_{m',n}^{L'*}(\Omega_0), \tag{A.17}$$

where K is used to label the eigenvalues of the diffusion matrix, $\hat{R}^{mn}$. Using the un-normalized Wigner matrices here, the symmetrized conditional probability can be written as

$$\hat{P}(\Omega_0 \mid \Omega t) = \frac{1}{8\pi^2}\sum_{K}\sum_{JJ'}\sum_{mn}\sqrt{(2J+1)(2J'+1)}$$

$$\times(\hat{X}^{mn})_{J,K}\exp(D_{\perp}\hat{r}_{K}^{mn}t)(\hat{X}^{mn})_{J,K}\times D_{m,n}^{J}(\Omega)D_{m,n}^{J'*}(\Omega_0) \tag{A.18}$$

The orientational probability may be obtained from the asymptotic condition

$$P(\Omega) = \lim_{t\to\infty}P(\Omega_0 \mid \Omega t) \tag{A.19}$$

All the exponentials in Eq. (A.18) decay to zero at infinite time except for the one

corresponding to the zero eigenvalues, $\hat{r}_0^{00}$. The long time behaviour of the symmetrized conditional probability is

$$\lim_{t\to\infty}\hat{P}(\Omega_0\,|\,\Omega t) = P^{1/2}(\Omega_0)P^{1/2}(\Omega)$$

$$= \frac{1}{8\pi^2}\sum_{J''}\sum_{J'''}\sqrt{(2J''+1)(2J'''+1)}\times(\hat{X}^{00})_{J'',0}(\hat{X}^{00})_{J''',0}D^{J''}_{0,0}(\Omega)D^{J'''*}_{0,0}(\Omega_0) \quad \text{(A.20)}$$

Hence $P(\Omega)$ is given by

$$P(\Omega) = \frac{1}{8\pi^2}\sum_{J}\sum_{J'}\sqrt{(2J+1)(2J'+1)}$$

$$\times(\hat{X}^{00})_{J,0}(\hat{X}^{00})_{J',0}D^{J}_{0,0}(\Omega)D^{J'*}_{0,0}(\Omega_0)\,, \quad \text{(A.21)}$$

where $(\hat{X}^{00})_{J',0}$ is from Eq. (A.15) using $m=n=0$. Rewriting the equation for a stochastic process[9],

$$\left\langle D^{L}_{m,n}(\Omega_0)D^{L'*}_{m',n'}(\Omega)\right\rangle = \int d\Omega_0 P(\Omega_0)D^{L}_{m,n}(\Omega_0)\times\int d\Omega P(\Omega_0\,|\,\Omega,t)D^{L'*}_{m',n'}(\Omega) \quad \text{(A.22)}$$

the correlation functions are

$$g^{L}_{mn}(t) = \int d\Omega_0 P^{1/2}(\Omega_0)D^{L}_{m,n}(\Omega_0)\times\int d\Omega P^{1/2}(\Omega)\hat{P}(\Omega_0\,|\,\Omega t)D^{L*}_{m,n}(\Omega)\,. \quad \text{(A.23)}$$

Substituting Eqs. (A.18) and (A.20) to Eq. (A.23), the correlation functions become

$$g^{L}_{mn}(t) = \sum_{K}\exp(D_{\perp}\hat{r}^{mn}_{K}t)\sum_{JJ'}\sum_{J''J'''}\sqrt{\frac{(2J+1)(2J'+1)}{(2J''+1)(2J'''+1)}}$$

$$\times(\hat{X}^{mn})_{J,K}(\hat{X}^{mn})_{J'K}(\hat{X}^{00})_{J'',0}(\hat{X}^{00})_{J''',0}$$

$$\times c(L,J',J''';m,-m)c(L,J',J''';n,-n)$$

$$\times c(L,J,J''';m,-m)c(L,J,J'';n-n)\,, \quad \text{(A.24)}$$

where the results of the integrals involving three Wigner matrices have been expressed in terms of the Clebsch-Gordon coefficients $c(A,B,C;d,e)$. The above equation can be

written as an infinite sum of decaying exponentials [Eq. (3.7)].

References

[1] R.Y.Dong, *Nuclear Magnetic Resonance of Liquid Crystals*, 2nd ed. (Springer, New York, 1997).

[2] P.L.Nordio and P.Busolin, J. Chem. Phys. **55**, 5485 (1971).

[3] P.L.Nordio, G.Rigatti, and U.Segre, J. Chem. Phys. **76**, 253 (1972).

[4] J.M.Bernassau, E.P.Black, and D.M.Grant, J. Chem. Phys. **76**, 253 (1982).

[5] J. Bulthuis and L.Plomp, J. Phys. France **51**, 2581 (1990).

[6] R.Tarroni and C.Zannoni, J. Chem. Phys. **95**, 4550 (1991).

[7] E.Berggren, R.Zannoni, and C. Zannoni, J. Chem. Phys. **99**, 6180 (1993).

[8] E.Berggren and C.Zannoni, Mol. Phys. **85**, 299 (1995).

[9] P.L.Nordio and U.Segre, *The Molecular Physics of Liquid Crystals*. (Academic Press, New York, 1979).

Appendix B

Order Director Fluctuation

Order Director Fluctuations (ODF) [1,2] describe thermal fluctuations of the orientation of the director and involve collective motions of a large number of molecules in an anisotropic elastic continuum. In lamellar phase of lyotropics, where layer structures are more pronounced, this is sometimes called undulation [3]. Since ODF shows different frequency dependences in different mesophases, NMR field cycling experiments are instrumental to study ODF mechanism and ODF is found to dominate the spin-lattice relaxation dispersion at Larmor frequencies below 1MHz [4].

To describe the ODF contribution to spectral densities, a small angle (θ) approximation is often used, where θ is the angle between the instantaneous director and its equilibrium orientation. Because ODF involve a distribution of correlation times involving long wavelength modes, the spectral densities show characteristic frequency behaviours. Here we highlight the orientation dependence of the equilibrium director being in the direction of the external B_0 field. When the principal component of the spin interaction (e.g. C-D bond) is fixed w.r.t. an assumed axis of cylindrical symmetry of the molecule given by the angle $\beta_{M,Q}$,the spectral densities are given to second-order in θ for nematics by[5-7]

$$J_0(\omega) = A^2 \frac{\langle P_2 \rangle^2}{(1-3\alpha)^2} \left[d^2_{00}(\beta_{M,Q}) \right]^2 \frac{1}{\pi} \ln\left[1 + \left(\frac{\omega_c}{\omega} \right)^2 \right] \qquad \text{(B.1)}$$

$$J_1(\omega) = A\frac{\langle P_2\rangle^2}{(1-3\alpha)^2}\left[d^2_{00}(\beta_{M,Q})\right]^2 \times (1-4\alpha)U\left(\frac{\omega_c}{\omega}\right)\omega^{-1/2} \tag{B.2}$$

$$J_2(\omega) = A^2\frac{\langle P_2\rangle^2}{(1-3\alpha)^2}\left[d^2_{00}(\beta_{M,Q})\right]^2\frac{1}{3\pi}\times\ln\left[1+\left(\frac{\omega_c}{\omega}\right)^2\right], \tag{B.3}$$

where $\langle P_2\rangle$ is the nematic order parameter, the cutoff function $U(\omega_c/\omega)$ accounts for the cutoff of coherence modes at high frequencies

$$U(x) = \frac{1}{2\pi}\ln\left[\frac{x-\sqrt{2x}+1}{x+\sqrt{2x}+1}\right] + \frac{1}{\pi}[\tan^{-1}(\sqrt{2x}-1) + \tan^{-1}(\sqrt{2x}+1)] \tag{B.4}$$

and the prefactor A is given by,

$$A = \frac{3kT}{4\sqrt{2}\pi}\left(\frac{\eta}{K^3}\right)^{1/2} = \frac{3\pi\alpha}{2\sqrt{2\omega_c}}, \tag{B.5}$$

where ω_c is the high frequency cutoff, K is an average elastic constant, η is an average viscosity and the α parameter defined by Eq. (B.5) is a measure of the magnitude of director fluctuations (α <<1).

References

1 R.Y.Dong, *Nuclear Magnetic Resonance of Liquid Crystals*, 2nd ed. (Springer, New York, 1997).

2 R.Y.Dong, Prog. in NMR Spect. **41**, 115 (2002).

3 P. G. d. Gennes and J.Prost, *The Physics of the Liquid Crystals*. (Oxford University Press, Oxford, 1993).

4 W.Wolfel, F.Noack, M.Stohrer, and Z.Naturforsch, J. Chem. Phys. **30**, 437 (1975).

5 R.L.Vold, R.R.Vold, and M.Warner, J. Chem. Soc. Faraday Trans. II **84**, 997

(1988).

[6] G. V. d. Zwan and L.Plomp, Liq. Cryst. **4**, 133 (1989).

[7] E.A.Joghems and G. V. d. Zwan, J. Phys. II **6**, 845 (1996).